

Washington University in St. Louis
Washington University Open Scholarship

Engineering and Applied Science Theses &
Dissertations

McKelvey School of Engineering

Winter 12-15-2017

Characterizing anisotropy in fibrous soft materials by MR elastography of slow and fast shear waves

John Larson Schmidt

Washington University in St. Louis

Follow this and additional works at: https://openscholarship.wustl.edu/eng_etds



Part of the [Biomechanics Commons](#), [Biomedical Engineering and Bioengineering Commons](#),
and the [Mechanical Engineering Commons](#)

Recommended Citation

Schmidt, John Larson, "Characterizing anisotropy in fibrous soft materials by MR elastography of slow and fast shear waves" (2017).
Engineering and Applied Science Theses & Dissertations. 299.
https://openscholarship.wustl.edu/eng_etds/299

This Dissertation is brought to you for free and open access by the McKelvey School of Engineering at Washington University Open Scholarship. It has been accepted for inclusion in Engineering and Applied Science Theses & Dissertations by an authorized administrator of Washington University Open Scholarship. For more information, please contact digital@wumail.wustl.edu.

WASHINGTON UNIVERSITY IN ST. LOUIS

School of Engineering and Applied Sciences
Mechanical Engineering and Materials Science

Dissertation Examination Committee:

Philip V. Bayly, Chair

Joel R. Garbow

Guy M. Genin

Ruth J. Okamoto

David A. Peters

Jessica E. Wagenseil

Characterizing Anisotropy in Fibrous Soft Materials by MR Elastography of Slow and Fast
Shear Waves

by

John L. Schmidt

A dissertation presented to
The Graduate School
of Washington University in
partial fulfillment of the
requirements for the degree
of Doctor of Philosophy

December 2017
St. Louis, Missouri

© 2017, John L. Schmidt

Table of Contents

List of Figures	v
List of Tables	x
Acknowledgments.....	xi
Abstract of the Dissertation	xiv
Chapter 1: Soft tissue mechanical characterization: Magnetic resonance elastography (MRE), mechanical anisotropy	1
1.1 Overview: mechanical characterization of soft tissues	1
1.2 Significance.....	2
1.2.1 Palpation	2
1.2.2 Traumatic brain injury	2
1.2.3 Tissue material properties affect medical device implantation.....	4
1.2.4 Mechanical anisotropy of soft tissues	6
1.2.5 Material nonlinearity of soft tissue at large strains	7
1.3 Elastography: non-invasive measurement of soft tissue mechanical properties.....	7
1.3.1 Principles of magnetic resonance elastography (MRE)	7
1.3.2 Parameter estimation from MRE	8
1.4 Summary	10
1.5 Specific Aims and Dissertation Outline.....	11
1.5.1 Specific aims	11
1.5.2 General Organization	12
Chapter 2: Theoretical background and imaging methods	14
2.1 Overview	14
2.2 Equilibrium	15
2.3 Kinematics: Strain – displacement relationships	15
2.4 Constitutive Equations	16
2.5 Harmonic plane wave propagation	21
2.5.1 General.....	21
2.5.2 Wave speeds in an isotropic medium.....	22

2.5.3 Wave speeds and polarizations in a transversely isotropic medium	22
2.6 Shear wave propagation in media under finite deformation	25
2.7 Imaging Methods and Analysis.....	26
2.7.1 Introduction.....	26
2.7.2 Magnetic resonance imaging (MRI)	26
2.7.3 Magnetic resonance elastography (MRE).....	26
2.7.4 Estimation of material parameters in MRE.....	29
2.8 Summary	32
Chapter 3: Magnetic resonance elastography of slow and fast shear waves illuminates differences in shear and tensile moduli in anisotropic tissue	34
3.1 Overview	34
3.2 Introduction	35
3.3 Methods.....	36
3.3.1 Theory: fast and slow shear-wave speeds in elastic, incompressible, transversely isotropic materials.....	36
3.3.2 Experiments: slow and fast shear waves in cylindrical and cube specimens.....	39
3.3.3 Image analysis: characterization of anisotropic wave propagation.....	43
3.4 Results	48
3.4.1 Imaging experiments.....	48
3.4.2 Direct mechanical characterization	54
3.5 Discussion	55
3.6 Conclusion	59
Chapter 4: Measurement of anisotropic mechanical properties in porcine brain white matter ex vivo using magnetic resonance elastography.....	61
4.1 Overview	61
4.2 Introduction	62
4.3 Methods.....	65
4.3.1 Theory	65
4.3.1 Experiments	66
4.3.1.1 Sample preparation	66
4.3.1.2 Imaging	67
4.3.1.3 Computational modeling and simulations.....	68

4.3.1.4 Analysis of experimental and simulated image data.....	69
4.3.1.5 Dynamic shear testing (DST).....	72
4.4 Results	73
4.4.1 MRE experiments and FE simulations exhibit elliptical shear wave propagation.....	73
4.4.2 Estimated local wavelength comparisons between experiment and FE models	73
4.5 Discussion and Conclusions.....	78
4.6 Conclusions	82
Chapter 5: Probing mechanical nonlinearity of soft tissue: a path forward using MRE.....	83
5.1 Overview: Nonlinear mechanical characterization of soft tissues	83
5.2 Significance.....	83
5.3 Nonlinear deformation effects on shear waves	84
5.3.1 Brief theoretical review.....	84
5.3.2 Finite element simulations of nonlinear deformations and MRE	88
5.3.3 Data analysis	93
5.4 Proposed experimental methods	95
5.4.1 Overview.....	95
5.4.2 Experimental apparatus.....	97
5.4.3 Experimental protocol.....	101
5.5 Conclusions	101
Chapter 6: Summary, Conclusions, and Future Directions	102
6.1 Summary of Work.....	102
6.2 Limitations	103
6.2.1 MRI and MRE resolution.....	103
6.2.2 Transverse isotropy as a model for fibrous tissues	104
6.2.3 Assumption of material incompressibility	104
6.3 Future directions	105
6.3.1 Orthotropic material models	105
6.3.2 Noncontact excitation	105
6.3.2 MRE applied to estimate nonlinear material properties.....	105
References	107
Vita.....	114

List of Figures

Figure 1.1: MRI tagging study showing impact to the head and corresponding strain. a) Schematic diagrams of head motion in the sagittal plane b) Lagrangian strain tensor fields at 18, 78 and 84 milliseconds after skull motion was stopped after impact to the posterior of the head. Here ϵ_{xx} is the dimensionless strain in the x-direction, ϵ_{yy} in the y-direction, and ϵ_{xy} the shear strain. Adapted from reference (Bayly et al., 2005).	3
Figure 1.2: Surgical implantation of stimulation electrodes into the subthalamic nucleus for deep brain stimulation therapy. Adapted from Reference (Benabid et al., 2009).	5
Figure 1.3: The complicated structure of human intervertebral disc. Adapted from Reference (Urban and Winlove, 2007).....	6
Figure 2.1: The propagation direction (denoted by unit vector \mathbf{n}) and polarization directions (unit vectors \mathbf{m}_s and \mathbf{m}_f) of slow and fast shear waves, respectively, in an incompressible, transversely isotropic, elastic material. The unit vector \mathbf{a} denotes the normal to the plane of isotropy. (Reproduced from: Schmidt et al., 2016).....	24
Figure 2.2: A modified spin-echo MRE pulse diagram. (Clayton et al., 2011a)	27
Figure 2.3: Experimental MRE displacement data acquired in gelatin/glycerol (isotropic, Okamoto et al., 2011) at 200 Hz mechanical actuation.....	29
Figure 2.4: Simulated harmonic displacement data in a material representing gelatin ($\mu = 1.1$ kPa, $\rho = 1100$ kg/m ³) at 200 Hz mechanical actuation.	29
Figure 2.5: Simulated harmonic displacement data in a material representing gelatin ($\mu = 1.1$ kPa, $\rho = 1100$ kg/m ³) at 200 Hz mechanical actuation.	30
Figure 2.6: Simulated harmonic displacement data in a material representing gelatin ($\mu' = 1.1$ kPa, $\rho = 1100$ kg/m ³) at 200 Hz mechanical actuation. (a) Shear storage modulus, μ' . (b) Shear loss modulus, μ''	32
Figure 3.1: The propagation direction (denoted by unit vector \mathbf{n}) and polarization directions (unit vectors \mathbf{m}_s and \mathbf{m}_f) of slow and fast shear waves, respectively, in an incompressible, transversely isotropic, elastic material. The unit vector \mathbf{a} denotes the normal to the plane of isotropy.	38
Figure 3.2: Schematic diagrams of: (a) cylindrical specimen with axial excitation; (b) cube specimen with tangential excitation in a plane parallel to the fiber direction to induce “fast” shear waves. (c) cube specimen with tangential excitation perpendicular to the dominant fiber direction to induce “slow” shear waves. (d) photograph of cylindrical turkey breast specimen embedded in gelatin (corresponding to panel a). (e) photograph of experimental setup for cube turkey breast (corresponding to panel b; actuator on left). (f) photograph of a cylindrical sample placed in RF coil with actuator on right.....	40
Figure 3.3: Fiber orientation estimated by DTI in (a) cylindrical and (b) cube specimens of turkey breast. Maximum principal diffusion direction vectors (cyan) are superimposed on fractional anisotropy maps (FA, grey) for each voxel.	43
Figure 3.4: Wave propagation in axially-excited, cylindrical specimens. (a-c) Representative images of elliptical waves exhibiting direction-dependent propagation with different wave speeds in different directions. (a)	

Representative sample #1 of turkey breast, 800 Hz; (b) Representative sample #2 of turkey breast, 800 Hz; (c) aligned fibrin gel, 200 Hz. (d) Circular waves in (isotropic) gelatin, 200 Hz. (e) Ellipses were fitted to the wave images (white and black lines in b-d) and the average ratios of their semi-axes are shown for the different materials.44

Figure 3.5: Wave propagation in a cylindrically aligned fibrin gel (200 Hz actuation) specimen, illustrating analysis by directional filtering. (a) Elliptical waves exhibiting direction dependent propagation with different wave speeds in different directions. (b-c) Displacement field after directional filtering in each of two propagation directions specified by angle, θ , from the dominant fiber direction. (b) $\theta = 0^\circ$ and (c) $\theta = 90^\circ$46

Figure 3.6: Wave propagation in a cube specimen of aligned fibrin with dominant fiber direction at 45° from horizontal (Figures 3.1(b,c)), illustrating analysis by directional filtering. (a) Excitation (600 Hz) in the m_f direction (with a component along the fibers, as in Figure 3.1(b)) leads to predominantly downward-propagating fast shear waves. (b) Excitation (600 Hz) in the m_s direction, perpendicular to the fibers, as in Figure 3.1(c), leads to predominantly downward-propagating slow shear waves. Panels (c,d): Directionally filtered waves in the $[0 -1 0]$ direction corresponding to panels (a,b) respectively.46

Figure 3.7: Shear wave attenuation. (a) Wave propagation (200 Hz) in a cylindrical specimen of aligned fibrin gel. (b) Directionally filtered slow-wave (u_s , $\theta = 90^\circ$) displacement in the fibrin specimen shown in (a), as a function of radial position. Markers show successive peaks used for attenuation ratio. (c) Wave propagation in a finite element (COMSOL) simulation of an ITI material excited at 200 Hz with estimated parameters for fibrin gel, including a loss factor of $\eta = 0.2$. (d) Directionally filtered slow-wave (u_s , $\theta = 90^\circ$) displacement in the simulation described in (c). (e) Wave propagation (800 Hz) in a cylindrical specimen of turkey breast. (f) Directionally filtered slow-wave (u_s , $\theta = 90^\circ$) displacement in the turkey breast specimen shown in (e). (g) Wave propagation in a finite simulation of an ITI material excited at 800 Hz, with estimated parameters for turkey breast, including a loss factor of $\eta = 0.4$. (h) Directionally filtered slow-wave (u_s , $\theta = 90^\circ$) displacement in the simulation described in (g).48

Figure 3.8: Average (\pm std. deviation) slow shear-wave speeds (blue *) plotted vs the angle between propagation direction and the horizontal axis of the cylinder, in cylindrical specimens. (a) Representative sample #1 of turkey breast (800 Hz). (b) Representative sample #2 of turkey breast (800 Hz). (c) Aligned fibrin gel (200 Hz). (d) Gelatin (200 Hz). Each plot is for a single sample; average values for each direction are computed over 5 slices. Theoretical curves (red lines) are obtained from Eq. 3.2 using values of μ and ϕ estimated by weighted, least-squares fitting for each sample.50

Figure 3.9: Wave propagation visualized by MRE in cube samples with different directions of excitation relative to fiber orientation. Fibers are oriented approximately 45° from horizontal as in Figure 2(b,c). Top panels (a,b) show fast and slow wave propagation in turkey breast actuated at 800 Hz and bottom panels (c,d) show aligned fibrin actuated at 600 Hz. Left panels (a,c): Actuation in the m_f direction with a component along the fibers (as in Figure 3.2(b)) leads to downward-propagating, fast shear waves. Right panels (b,d): Actuation in the m_s direction, perpendicular to the fibers (as in Figure 3.2(c)) leads to downward-propagating, slow shear waves.51

Figure 3.10: Summary of shear-wave speeds in turkey breast (a, b) and aligned fibrin (c, d) at different angles θ of propagation direction relative to fiber direction. (a) Slow shear-wave speed in cylindrical turkey breast specimens (800 Hz, $N = 4$ samples). Estimated material parameters: $\mu = 33.1 \pm 11.4$ kPa, $\phi = 1.3 \pm 0.7$ (b) Fast and slow shear-wave speeds in cube specimens (800 Hz, $N=5$). Estimated parameters: $\mu = 33.2 \pm 16.7$, $\zeta = 9.2 \pm 4.9$. (c) Slow shear-wave speeds in a cylindrical fibrin specimen (200 Hz, $N=3$). Estimated material parameters: $\mu = 1.1 \pm 0.5$ kPa, $\phi = 1.1 \pm 0.2$ (d) Average fast and slow shear-wave speeds in a cube specimen of aligned fibrin (600 Hz, $N=1$). Estimated parameters: $\mu = 4.7$ kPa, $\zeta = 2.7$52

Figure 3.11: Storage (elastic) and loss (viscous) components of the complex shear modulus $\mu^* = \mu' + i\mu''$ of turkey breast (N=33, 30-40 Hz) measured by direct mechanical testing (DST). The ratio of the storage moduli was $\mu'_{\parallel}/\mu'_{\perp} = 1.5 \pm 0.3$, the ratio of the loss moduli was $\mu''_{\parallel}/\mu''_{\perp} = 2.0 \pm 0.3$, and the ratio of the magnitudes was $\mu_{\parallel}/\mu_{\perp} = 1.6 \pm 0.3$ ($\phi = 0.6 \pm 0.3$). 55

Figure 4.1: (a-b) T1-weighted (T1W) *in vivo* anatomical images from prior work (Bayly et al., unpublished) showing tissue volume used for current study (red dashed outlines). (c) T1W images of *ex vivo* sample used in the current study. Fiber orientation is left-to-right. (d) Photo of *ex vivo* sample of brain tissue used for this study. (e) Apparatus for MRE experiments: tissue embedded in gel inside cylindrical container, excited by harmonic motion of a central axial stinger. 67

Figure 4.2: FE model (COMSOLTM Multiphysics v5.1) showing axial (w) displacement. A disk-shaped inclusion representing transversely isotropic (TI) WM is enclosed in an isotropic soft material representing gelatin. Inclusion: $\mu_2 = 2.0$ kPa, $\mu_1 = 2.6$ kPa ($\phi=0.30$), $\eta = 0.5$, $\rho = 1000$ kg/m³. Surrounding gelatin: $\mu = 1.1$ kPa, $\eta = 0.1$, $\rho = 1100$ kg/m³. Actuation frequency: 200 Hz. The black arrow points in the direction normal to the TI material's plane of isotropy (i.e., the fiber axis, a) 69

Figure 4.3: Shear-wave propagation in WM brain tissue (experiment, top row) and transversely isotropic FE models (simulation, bottom row) with fitted ellipses outlined. (a-c) MRE images of shear wave propagation in WM at (a) 100 Hz, (b) 200 Hz, and (c) 300 Hz. Shear-wave fronts are fitted by ellipses (black or white). The boundary of the tissue sample is outlined by a thin dotted white line. (d) Shear-wave propagation in a slice containing only gelatin at 300 Hz. (e-g) Shear wave propagation in FE simulations with similar mechanical properties to the experiment: (e) 100 Hz, $\mu_2 = 1100$ Pa, $\phi = 0.30$; (f) 200 Hz, $\mu_2 = 1600$ Pa, $\phi = 0.45$; (g) 300 Hz, $\mu_2 = 2300$ Pa, $\phi = 0.35$. (h) Shear-wave propagation in the isotropic/gelatin portion of the FE model at 300 Hz. 71

Figure 4.4: Apparent shear modulus in WM brain tissue and transversely isotropic (TI) FE models. Regions of interest (ROIs) parallel (\parallel) and perpendicular (\perp) to fitted ellipse semi-major axis are highlighted. (a-c) Maps of apparent shear modulus at (a) 100 Hz, (b) 200 Hz, (c) 300 Hz, estimated from MRE data in slices containing brain tissue. (d) Maps of apparent shear modulus at 300 Hz, estimated from MRE data in slices containing only gelatin. (e-g) Maps of apparent shear modulus estimated using data from FE simulations with mechanical properties matched to the experiment: (e) 100 Hz: $\mu_2 = 1100$ Pa, $\phi = 0.30$; (f) 200 Hz: $\mu_2 = 1600$ Pa, $\phi = 0.45$; (g) 300 Hz: $\mu_2 = 2300$ Pa, $\phi = 0.35$. (h) Maps of apparent shear modulus at 300 Hz, estimated using data from the isotropic/gelatin portion of the FE model. 72

Figure 4.5: Parameter estimation by comparison of experiment to simulation. Results from inversion of data from MRE experiments are matched to results of inversion of data from a library of FE simulations performed with a range of plausible transversely isotropic (TI) material parameters. Results from \perp and \parallel ROIs are compared separately to identify effects of anisotropy. (a) Normalized RMS error (NRMSE) between wavelength (λ_2) estimates from experimental data and TI FE simulations in the \perp ROI. (b) NRMSE between wavelength (λ_1) estimates from experimental data and FE simulations in the \parallel ROI. (c) NRMSE between the ratio of semi-axes of ellipses fitted to shear-wave fronts in the experimental data and FE simulations. (d) Weighted total NRMSE between experiment and FE models (weighted sum of wavelength NRMSEs and axis ratio NRMSE). 75

Figure 4.6: Summary of shear modulus and shear anisotropy estimates in WM brain tissue. (a) Shear moduli in planes parallel (μ_1) and perpendicular (μ_2) to fiber orientation. (b) Shear anisotropy ($\phi = \mu_1/\mu_2 - 1$). Solid bars (100 Hz, 200 Hz, 300 Hz) represent results from MRE/FE analysis. Cross-hatched bars (20-30 Hz) show results obtained by direct mechanical testing (DST). Lines across plots with stars indicate statistical significance (* $P <$

0.05, ** $P < 0.005$). Curly bracketed lines signify Friedman tests across 100 Hz, 200 Hz, and 300 Hz. Straight lines signify Wilcoxon signed rank tests between two sets of data.76

Figure 5.1: Free-body diagram of a solid undergoing two deformations. (a) a static, finite deformation of a solid body to a specified operating point (u_0 ; corresponding to experimental displacement on the order of millimeters). (b) a superimposed dynamic deformation (\tilde{u}) associated with incremental displacements on the order of micrometers. The angle, θ , represents the angle of imposed shear.87

Figure 5.2: Deformations applied to the 15mm³ model in step 0 (a), step 1 (b), and step 2 (c). Step 0, the initial step, does not involve any displacements or strains on the material. Step 1, the deformation of the solid to the operating point involves finite strain, and displacements on the order of mm. Step 2, the incremental displacement involves harmonic displacements on the order of μm at 600 Hz.91

Figure 5.3: (first column) Logarithmic shear strain (γ_{12}^{\log}) and (second column) displacement in the FE model after the imposed deformation of step 1. (third column) Shear waves in the model from step 2 at a frequency of actuation of 600 Hz. Rows (a-e) correspond to applied finite displacements of [0, 0.75, 1.50, 2.25, 3.0] mm and thus to the targeted imposed strains (α) of [0, 0.05, 0.10, 0.15, 0.20].92

Figure 5.4: Stress and strain in the center of the FE model during the large deformation step (step 1). (a) Half of the model is displayed (cut plane is the YX plane). All data in (b) and (c) are from the element highlighted in red in the middle (in X, Y, and Z directions) of the model. (b) Shear stress as a function of shear strain. Note the increase of stress as the strain is increased. (c) The derivative of the data in (b) showing the instantaneous (tangent) shear modulus at different strain states. Data are compared to theoretical predictions (blue line).93

Figure 5.5: Overview of logarithmic strain from ABAQUS (left column), estimates of shear modulus from local frequency estimation inversion (center column), and estimates of shear modulus local direct inversion (right column). Rows (a) – (e) represent differing operating points: applied strains of [0, 0.05, 0.10, 0.15, 0.20], respectively. The box within the deformed cube represents the area in the xy plane where data were averaged.94

Figure 5.6: Results of shear wave inversion in a deformed cube of Yeoh material, compared to theoretical predictions. Shear wavelength and shear modulus increase with finite deformation. Each black “x” represents averages in the boxed region of the corresponding panel in Figure 5.5: either the middle column (local frequency estimation, LFE, Knutsson et al., (1994)) or right column (local direct inversion, LDI, Okamoto et al., (2011b)). (a) Shear wavelength, estimated by LFE, increases with finite deformation. (b) Shear modulus, estimated by LDI, increases with finite deformation.95

Figure 5.7: Overview of the proposed experimental design, including the locations of components with respect to the MRI console and high magnetic field found in and around the MR magnet. Blue components refer to the mechanism for finite deformation (using tubing for transferring the deformation from the control room to the MRI scanner). Green components refer to the mechanism to induce superimposed waves, which is similar to the actuation used in many MRE studies.97

Figure 5.8: Concept drawing of a sample holder to be housed within the MR magnet bore. The system must deform the sample in shear to a specified operating point (displacements on order of mm), and induce shear wave deformations at high frequency (displacements on order of μm). The syringe on the right provides the large deformation and the piezoelectric actuator attached to the rod on the left provides high frequency, small-amplitude shear wave excitation (typically used in small animal and phantom MRE studies; Clayton et al., 2011; Schmidt et al., 2016).98

Figure 5.9: Sample holder (deformable cube) prototype. (a) CAD drawing of the deformable cube. (b) the finished sample holder cube; deformable by the application of force in the direction of the black arrow.99

Figure 5.10: Proposed apparatus to provide finite deformation within MR scanner. Linear actuator (left) connected to a syringe filled with fluid (right) – intended to stay within the MRI control room. The syringe is attached by tubing to the corresponding syringe within the apparatus in Figure 5.7. The linear actuator is controlled by a micro-controller.....100

Figure 5.11: A micro-controller (Arduino Uno R3) can combine input signals and output pulses to control scanning. (a) The function generator that drives the piezoelectric actuator can provide a TTL signal at the vibration frequency (e.g., 100 Hz), as input to the micro-controller. (b) An analogous TTL signal can be provided by the finite deformation mechanism as input to the micro-controller. The signal is 5V when the deformation has been performed and the sample is in-position and 0V otherwise. (c) A combination of these signals (AND operator), will be output from the micro-controller to trigger the scanner.100

List of Tables

Table 2.1: Common nomenclature and relationship to nomenclature in this study.	25
Table 3.1: Summary of incompressible, transversely isotropic (ITI) material parameter estimates from MRE of turkey breast muscle tissue and aligned fibrin gel. Parameters are: baseline shear modulus, μ ; shear anisotropy, ϕ ; tensile anisotropy, ζ ; loss factor, η .(* To estimate ζ in cube specimens, ϕ was set to the value measured in cylindrical specimens.)	54
Table 3.2: Average amplitudes of displacements in slow (u_s) and fast (u_f) shear waves observed in cylindrical and cube specimens.	54
Table 4.1: A summary of the findings in Chapter 4 using MRE. Baseline shear moduli (μ_2) and the shear moduli anisotropy factor (ϕ) for three experimental actuation frequencies (100, 200, and 300 Hz) are shown. The data is also expressed in Figure 4.6 (non cross-hatched bars).....	78
Table 5.1: Material parameters assigned to the FE model. The column on the right indicates the intended units of the parameters. Large values for D_2 and D_3 are chosen to neglect higher order volumetric terms (see Equation 5.3b). ..	90

Acknowledgments

Four years ago, Dr. Philip Bayly provided me with a research project for which I am sincerely grateful. Much of the success of this work, including the winning of a subsequent NSF grant, is a reflection on his restless dedication and astute attention to detail. This project and his mentorship have provided me with skills that go far beyond the laboratory and keyboard.

My colleagues and mentors within the lab are the support which have made my work possible.

Much of my success and the lab as a whole is due to the efforts of Dr. Ruth Okamoto. Her relentless quest for the correct answer is evident in all the lab's work. Dr. Dennis Tweten provided invaluable help in finite element model development and helped develop many advanced analysis methods. Dr. Andrew Badachhape was an enormous help with presentation, various technical issues, and brain tissue excision. Charlotte Guertler's assistance with CAD modeling and presentation immensely helped my thesis progression. I am also honored to have had the opportunity to work alongside such a dynamic set of undergraduate researchers, of which their support has been instrumental to my success: Ananya Benegal, Jake Ireland, Maisie Mahoney, Rachel Mickelson, Tally Portnoi and Chase Walker. Ananya, the undergraduate student who I worked with the longest, was always ready to go each week and provided me with a wealth of samples to test and data for my thesis. Jake always brought an interesting perspective to challenges and quite frequently spent long hours in the lab 3D printing and designing new structures. Maisie produced samples as well as discovered several new methods for sample preparation. Rachel assisted in the design and engineering of MRE apparatuses for *in vivo* mouse and nonlinear deformation of tissues projects. Tally provided help in the areas of sample production, direct mechanical testing, and analysis development. Chase spent countless hours producing mechanically anisotropic samples to be tested by MRE.

I want to thank Dr. Parag Banerjee, who is ultimately responsible for my matriculation to Washington University. His patience and mentorship for my first year as a graduate student was an exceptional foundation for which my graduate experience has been built upon.

The background required to write this dissertation was provided by the exemplary courses I have taken at Washington University, namely: continuum mechanics from Dr. Pathak, elasticity from Dr. Sellers, finite element analysis from Dr. Szabo, cardiac MRI from Dr. Caruthers, experimental solid mechanics from Dr. Wagenseil and nonlinear vibrations from Dr. Bayly. My time served as a TA was especially enriching under the instruction of Drs. Flores and Sastry.

I would like to acknowledge the Biomedical Magnetic Resonance Laboratory, specifically Drs. Joel Garbow, Xia Ge, Bill Spees, James Quirk, and Mr. John Engelbach. Dr. Xia Ge was always available to help with scanner and sequence issues. The preclinical animal study initiated by Dr. Joel Garbow (Genentech) has prepared me wonderfully for a future career aligned with industry.

The staff in the MEMS department have truly been crucial to my success. Linda Buckingham, Laura Barker, Felicia Dilworth, and Kevin Cowell always made sure my documents were in a row, provided me with the valuable assistance needed to get my research done, as well as provided me with excellent conversation and music recommendations.

Financial support of this work was provided by National Science Foundation grant CMMI-1332433, National Institutes of Health grant R01 NS-055951, and Genentech.

John Schmidt

*Washington University in St. Louis
December 2017*

*To my family, from whom my inspiration stems and whose
support has encouraged me to follow my ambitions.*

ABSTRACT OF THE DISSERTATION

Characterizing anisotropy in fibrous soft materials by MR elastography of slow and fast shear waves
by

John L. Schmidt

Doctor of Philosophy in Mechanical Engineering

Washington University in St. Louis, 2017

Professor Philip V. Bayly, Chair

The general objective of this work was to develop experimental methods based on magnetic resonance elastography (MRE) to characterize fibrous soft materials. Mathematical models of tissue biomechanics capable of predicting injury, such as traumatic brain injury (TBI), are of great interest and potential. However, the accuracy of predictions from such models depends on accuracy of the underlying material parameters. This dissertation describes work toward three aims. First, experimental methods were designed to characterize fibrous materials based on a transversely isotropic material model. Second, these methods are applied to characterize the anisotropic properties of white matter brain tissue *ex vivo*. Third, a theoretical investigation of the potential application of MRE to probe nonlinear mechanical behavior of soft tissue was performed. These studies provide new methods to characterize anisotropic and nonlinear soft materials as well as contributing significantly to our understanding of the behavior of specific biological soft tissues.

Chapter 1: Soft tissue mechanical characterization: Magnetic resonance elastography (MRE), mechanical anisotropy

1.1 Overview: mechanical characterization of soft tissues

Mechanical deformation of soft biological tissues, such as brain tissue, muscle tissue and cardiac tissue, is a natural occurrence in everyday life. Material parameters, which describe the relationship of stress (loading) to the strain (deformation) of tissue are important for the modeling and simulation of traumatic brain injury (TBI) and processes at the interface of implants and other medical devices. Clinical medicine has long relied on the manual evaluation of mechanical properties (palpation) to identify a variety of disease processes, such as tumors located in the breast or prostate. Knowledge of their material parameters in relation to soft tissues, however, is limited. Most biological tissues are mechanically anisotropic, heterogeneous, viscoelastic, and may have nonlinear behavior at high strains or strain rate. These properties require models to account for directionality, location, speed and amplitude of loading and deformations. Elastographic imaging methods and direct mechanical techniques now exist to identify the effect of these properties. This chapter describes current and past efforts to measure the parameters associated with these properties, with an emphasis on elastographic techniques.

1.2 Significance

1.2.1 Palpation

The mechanical properties of soft biological tissues have been of interest in medicine for centuries. Even with little understanding about tumors or other disease processes, manual palpation by an experienced person could lead to a successful diagnosis, simply by detecting soft and hard regions within tissue. Although modern imaging methods such as computed tomography (CT), magnetic resonance imaging (MRI), or ultrasound are used frequently during the pre-operative stage, a surgeon will often find new tumors through palpation during surgery (Manduca et al., 2001). Thus, identifying the mechanical properties of tissues is important for the diagnosis of disease or injury while also providing a more complete knowledge of healthy tissue.

1.2.2 Traumatic brain injury

Traumatic brain injury (TBI) is one of the leading causes of death and disability in the United States, with about 1.7 million people incurring the injury every year (Faul et al., 2010). It is estimated there are more than 5 million people living with lasting TBI-related disabilities in the United States (Schulz-Heik et al., 2016). Cognitive impairments among survivors are common, with survivors frequently incurring reduced quality of life (Lew et al., 2006).

TBI in the human brain occurs as a result of abnormally high strain in brain tissue, usually caused by high linear and angular accelerations of the skull (Holbourn, 1943). Studies involving tagged MRI during minor (non-injurious) impacts to the head (Figure 1.1) have illustrated the relationship of skull accelerations to brain tissue deformation (Bayly et al., 2005; Margulies and Thibault, 1992).

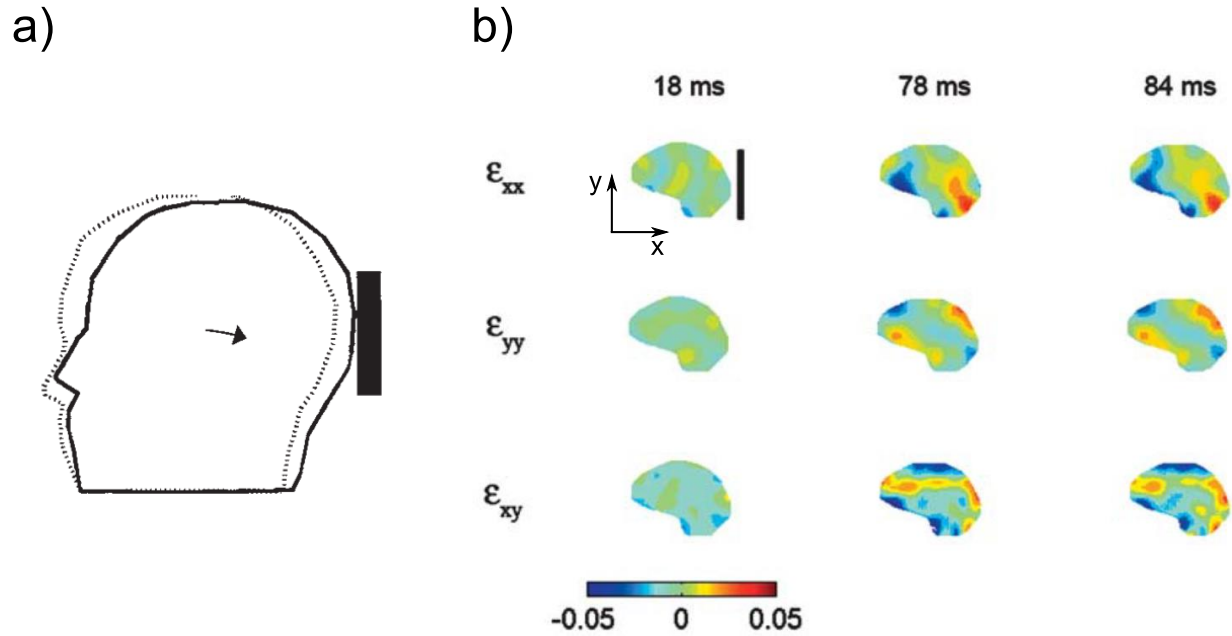


Figure 1.1: MRI tagging study showing impact to the head and corresponding strain. a) Schematic diagrams of head motion in the sagittal plane b) Lagrangian strain tensor fields at 18, 78 and 84 milliseconds after skull motion was stopped after impact to the posterior of the head. Here ϵ_{xx} is the dimensionless strain in the x-direction, ϵ_{yy} in the y-direction, and ϵ_{xy} the shear strain. Adapted from reference (Bayly et al., 2005).

Computer simulations using finite element (FE) methods offer enormous potential for the understanding and prevention of TBI. Experimental study of injurious conditions in humans is ethically impossible, therefore *in silico* experiments are a reasonable substitute. However, FE simulations require an accurate and thorough understanding of the mechanical behavior of brain tissue and the surrounding structures. In addition, while many authors have proposed computational models of TBI (Giordano et al., 2014; Kleiven and Hardy, 2002; Mao et al., 2013; Ueno et al., 1995; Vavalle et al., 2015; Zhang et al., 2004), validation, in the form of experimental data confirming the accuracy of these models, is lacking.

While computer models of TBI are generally less expensive than physical simulations using surrogate materials or devices, physical models are still important for understanding injury (Zhu et al., 2012) as well as for surgical training and simulation (Ploch et al., 2016). Desmoulin and Dionne (2009) describe the biomechanical response requirements needed to simulate many biological tissues (not only brain tissue) to physically replicate battlefield injuries.

1.2.3 Tissue material properties affect medical device implantation

The development of medical devices also requires a thorough understanding of tissue properties. Deep brain stimulation (DBS) treatments consist of the placement of stimulating electrodes to provide high frequency electrical impulses in the region of the ventral intermediate nucleus of the thalamus or globus pallidus (see Figure 1.2). Impulses applied in those regions have been found to treat the symptoms of essential tremor and Parkinson's disease, respectively (Perlmutter and Mink, 2006). Knowledge of the mechanical interaction between electrodes and surrounding brain tissue is critical. Movement of an implant relative to surrounding tissue (likely due to a mechanical mismatch) can lead to a glial scar surrounding the electrode (Groothuis et al., 2014), which can decrease stimulation effectiveness (Groothuis et al., 2014; Salatino et al., 2017).

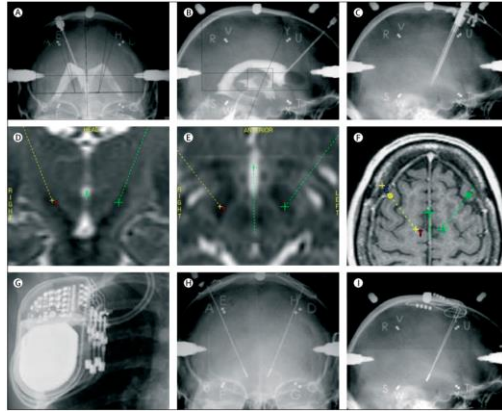


Figure 1.2: Surgical implantation of stimulation electrodes into the subthalamic nucleus for deep brain stimulation therapy. Adapted from Reference (Benabid et al., 2009).

The spinal intervertebral disc (IVD) has been shown to exhibit changes in mechanical properties with degeneration and aging (Iatridis et al., 1997). Figure 1.3 shows the various regions within the IVD. The mechanical properties of IVD could be important in the prediction of degeneration or the development/assessment of therapy. Mechanical characterization could also be crucial for total disc replacement, in which an artificial IVD implant replaces a completely degenerated IVD.

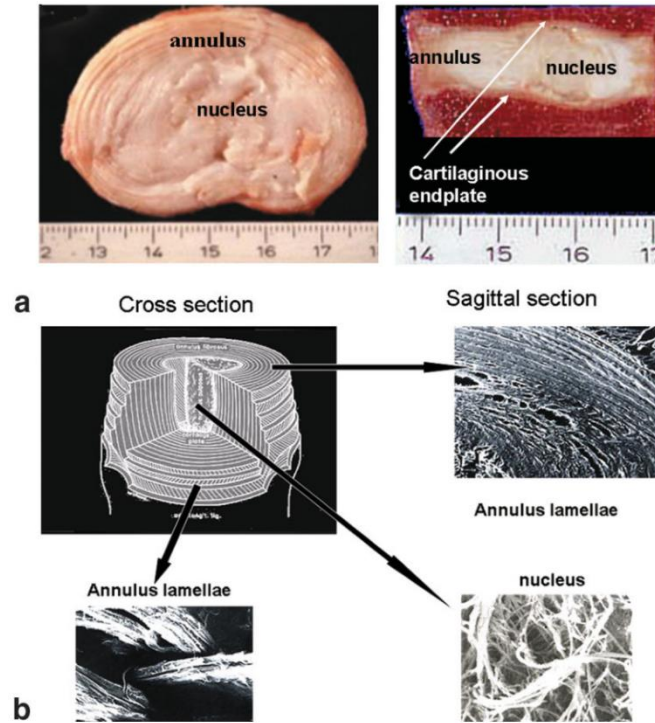


Figure 1.3: The complicated structure of human intervertebral disc. Adapted from Reference (Urban and Winlove, 2007).

1.2.4 Mechanical anisotropy of soft tissues

Mechanical anisotropy in a material refers to the dependence of a response on the direction of mechanical loading. Muscle tissue has shown to be anisotropic under compressive loads (Böl et al., 2014). The Achilles tendon has been found to exhibit mechanically anisotropic behavior in shear wave dispersion analysis (Brum et al., 2014).

Several recent studies have suggested brain white matter (WM) is mechanically anisotropic. In both small (Feng et al., 2013b) and large (Feng et al., 2017) deformations, brain tissue was observed to be anisotropic, with the authors applying a transversely isotropic model to interpret their data. Velardi et al. (2006) studied experimental behavior of *ex vivo* porcine brain tissue in extension and proposed an anisotropic, hyperelastic constitutive model to explain their data. Prange and Margulies (2002) studied *ex vivo* porcine and human brain tissue, finding a

directional dependence (though somewhat inconsistent) in WM. Ning et al. (2006) characterized brainstem experimental data as a transversely isotropic, viscoelastic material and compared observed behavior to the predictions of a corresponding numerical model.

1.2.5 Material nonlinearity of soft tissue at large strains

While complete characterization of the linear properties of soft tissue is important, it is important to note that injurious conditions typically involve large strains (Holbourn, 1943). Recently, injury thresholds in isolated optic nerve axon stretch studies (*ex vivo*, *in situ*) have been found to be ~ 0.2 strain (Bain and Meaney, 2000). Researchers have noted the need for non-linear material characterization rather than simply assuming linear material behavior in FE models (Brands et al., 2002).

1.3 Elastography: non-invasive measurement of soft tissue mechanical properties

Elastographic techniques, including both ultrasound elastography and magnetic resonance elastography (MRE) present an exciting future for non-invasive evaluation of the mechanics of soft tissues.

1.3.1 Principles of magnetic resonance elastography (MRE)

MRE relies on the measurement of oscillating displacements of tissue caused by an external harmonic vibration. These oscillating displacements generally correspond to shear waves propagating through the tissue. In an MRI scanner, the displacements caused by external harmonic vibration are measured by modulating the gradient field at the vibration frequency (Muthupillai et al., 1995a). The phase difference between the MR signals acquired during gradient field modulations applied in opposite directions is proportional to the displacement in

the direction of the gradients. Images of these phase differences (or phase contrast images), which encode the harmonic displacement of the tissue, are acquired at every voxel to create an image volume describing propagation of shear waves. Transient MRE, which measures the wave propagation of a single actuated pulse is also an active field of research (McCracken et al., 2005). This thesis focuses on harmonic, steady-state MRE.

1.3.2 Parameter estimation from MRE

MRE was originally developed using isotropic, elastic material models (Muthupillai et al., 1995b; Muthupillai and Ehman, 1996). Similar isotropic, elastic or viscoelastic models have been used to characterize tissues such as liver (Asbach et al., 2008; Klatt et al., 2010a; Mariappan et al., 2009), breast (Sinkus et al., 2005a), and brain (Atay et al., 2008; Clayton et al., 2011a; Feng et al., 2013a; Green et al., 2008; Johnson et al., 2013; Murphy et al., 2013; Sack et al., 2008). Elastic material models are often generalized for viscoelastic materials by the correspondence principle, which allows elastic moduli to be replaced with complex viscoelastic moduli (Clayton et al., 2011a) to describe the response to harmonic excitation.

Techniques used in MRE should be extended to account for directionally-dependent material properties. Work has recently been published on anisotropic material models in three general categories: theoretical studies, ultrasound elastography studies (involving estimation of two or three parameters), and MRE studies involving estimation of two, three, or five or more parameters. Rouze et al. (2013) showed agreement between predictions of a three-parameter, incompressible, transversely isotropic (ITI) theory and a finite element model. Royer et al. (2011) outlined an incompressible, transversely isotropic (ITI) model and approach for ultrasound elastography. Gennisson et al. (2003) also using ultrasound elastography, studied

transversely isotropic phantoms and measured shear moduli parallel and perpendicular to the fibers. Other recent ultrasound studies (Aristizabal et al., 2014; Wang et al., 2013) describe two different shear-wave speeds in transversely isotropic phantoms.

Anisotropic MRE has most commonly been used to estimate two elastic parameters: the two shear moduli governing shear in planes (i) parallel or (ii) perpendicular to the fiber direction. Such studies have been performed by Sinkus et al. (2005) (breast tissue); Green et al. (2013), Klatt et al. (2010b), Papazoglou et al. (2006), Qin et al. (2014, 2013) (muscle tissue); Qin et al. (2013) (anisotropic phantoms); and Namani et al. (2009) (aligned fibrin gels). MRE can also be used to estimate three parameters (for example, two shear moduli and an independent tensile modulus) for ITI material models (Feng et al., 2013b; Guo et al., 2015) and five parameters for general TI material models, or more for general orthotropic models (A Romano et al., 2012). Papazoglou et al. (2006) derived a three-parameter model for skeletal muscle tissue and an approach for estimation, though only two shear moduli were reported. Feng et al. (2013b) demonstrated that at least three elastic parameters are required to describe white matter in the brain because of anisotropy in shear and tensile moduli. Romano et al. (2012) identified five parameters in brain white matter (corticospinal tracts) with the application of spatial-spectral filters and Helmholtz decomposition to separate shear and pressure waves in a waveguide. These authors also applied their technique to patients with amyotrophic lateral sclerosis (Romano et al., 2014). Guo et al. (2015) measured three parameters in skeletal muscle by inverting the curl field measured by MRE. Tweten et al. (2015) showed by simulation that two types of shear waves must exist, with propagation of both waves in different directions, in order to estimate accurately the three material parameters. In the human brain, Anderson et al. (2016) used multiple

excitation methods and showed that estimates of isotropic material parameters depended on the directional properties of the wave field.

While these recent studies have illustrated the plausibility of different approaches to estimate parameters for TI material models, several key issues remain to be addressed. In most studies, the performance of the anisotropic inversion algorithm has not been validated, either by using data from simulations or from phantoms with known anisotropic properties. The notable exception is the study of Qin et al. (2013), which found close agreement between shear moduli estimated by MRE and direct measurements. Most importantly, in prior experimental work, the criterion that both slow (pure transverse, or PT) and fast shear (quasi-transverse, or QT) waves must be present (at significant amplitudes, with multiple directions) in the estimation region in order to estimate accurately all three ITI parameters (Tweten et al., 2017, 2015) was not explicitly met.

1.4 Summary

The mechanical properties of soft biological tissue are useful for diagnosis of disease and injury, and for characterization of normal tissue to learn about development and aging. Knowledge of these properties is essential for the accurate simulation of injury biomechanics, especially TBI, and crucial for developing safe and reliable medical devices. New elastographic imaging methods and direct mechanical tests can illuminate these properties.

1.5 Specific Aims and Dissertation Outline

1.5.1 Specific aims

At the outset of this work, three specific aims were proposed:

Aim 1: Develop a method to identify separate contributions of anisotropic shear and tensile moduli to the wave propagation in fibrous materials such as *ex vivo* muscle tissue and aligned fibrin gels.

Aim 2: Estimate the shear and tensile anisotropic parameters of *ex vivo* white matter.

Aim 3: Study the non-linear behavior of ITI tissue and tissue surrogates by imaging wave (infinitesimal) motion superimposed on larger (finite) deformations.

Over the last year, the dissertation scope has been modified slightly, in part to facilitate a pilot project on MRE in the mouse liver, funded by industry (Genentech). Significant progress was still achieved in each of the proposed Aims.

The following was actually performed for each aim:

Aim 1: Developed a method to identify separate contributions of anisotropic shear and tensile moduli to the wave propagation in fibrous materials such as *ex vivo* muscle tissue and aligned fibrin gels.

Aim 2: Estimated the anisotropic shear parameters of *ex vivo* white matter.

Aim 3: Studied the non-linear behavior of a solid *in silica* by analyzing wave (infinitesimal) motion superimposed on larger (finite) deformations.

1.5.2 General Organization

Chapter 2 provides an overview of the mathematical theory required to perform this work. Basic principles of continuum mechanics, wave motion, and their relationships to MRE are briefly reviewed.

Chapter 3 describes experimental work on the excitation and imaging of slow and fast shear waves in fibrous soft tissue (Aim 1). The test materials were *ex vivo* muscle tissue (turkey breast) and fibrous surrogate biomaterial (magnetically aligned fibrin). Wave fields were directionally filtered and shear wave speeds were measured to estimate the anisotropic parameters that describe the response of fibrous soft materials to shear and tension. Data were compared to direct mechanical tests (dynamic shear tests).

In Chapter 4, shear anisotropy is characterized using MRE in white matter brain tissue (Aim 2). Excised portions of *ex vivo* porcine white matter brain tissue were studied using methods detailed in Chapter 3. Due to the small size of the sample, finite element simulations similar to the experiment were created to aid in parameter estimation, allowing estimation of parameters without relying on typical assumptions of infinite, uniform domain.

In Chapter 5, a method is proposed to probe nonlinear properties of soft tissue, primarily through simulation and theoretical analysis of waves in a nonlinear, hyperelastic material (Aim 3). The effect of an imposed, finite shear strain on shear wave speed is explored analytically in a Yeoh material model. This effect is confirmed by finite element simulations and analysis of simulated data, which replicate a proposed experiment and corresponding data processing steps.

Conclusions, experimental limitations, and future work are discussed in Chapter 6.

Chapter 2: Theoretical background and imaging methods

2.1 Overview

In this chapter, equations of motion for steady-state harmonic wave propagation in fibrous materials are derived. Understanding wave behavior in anisotropic materials is potentially valuable for characterizing soft fibrous biological tissues. The starting point is the equation of dynamic equilibrium (Newton's 2nd law) in a continuum. Constitutive relationships for isotropic and anisotropic (transversely isotropic), linear, elastic materials are then introduced, along with the kinematic equations that relate displacement and strain in small deformations. The resulting equation (Navier's equation) admits harmonic plane wave solutions, which can be found from the acoustic tensor, for a given propagation direction. We compare our approach and nomenclature to other descriptions, and describe the extension of our methods to the characterization of nonlinear materials. Finally, the theory and application of MRE to these models is explained.

2.2 Equilibrium

Newton's second law, which defines the force ($\mathbf{F} = m\mathbf{a}$) acting on a body and the resulting motion can be applied to a material element of an arbitrary solid:

$$\frac{\partial \sigma_{ij}}{\partial x_i} = \rho \frac{\partial^2 u_j}{\partial t^2} \quad (2.1)$$

to relate the components of the stress tensor ($\boldsymbol{\sigma}$) and displacement vector (\mathbf{u}) in a Cartesian reference frame for $i, j = 1, 2, 3$ (typically x, y, z coordinates).

2.3 Kinematics: Strain – displacement relationships

Given two particles at initial points P and P_0 of a body under load, the displacement of a particle is a function of position,

$$u_i = u_i(x_1, x_2, x_3), \quad (2.2)$$

which can be expanded by Taylor series around P_0 (Chou and Pagano, 1992):

$$u_i = u_i^0 + \frac{\partial u_i}{\partial x_j} (x_j - x_j^0) + \frac{1}{2!} \frac{\partial^2 u_i}{\partial x_j \partial x_k} (x_j - x_j^0)(x_k - x_k^0) + \dots, \quad (2.3)$$

Dropping the second and higher powers as $x_j - x_j^0$ and infinitesimal quantities, we can express this as:

$$u_i = u_i^0 + \frac{\partial u_i}{\partial x_j} dx_j \quad (2.4)$$

where $dx_j = x_j - x_j^0$. The gradient $\partial u_i / \partial x_j$ is a second-order tensor, because u_i is a vector.

Equation 2.4 can now be expressed as:

$$u_i = u_i^0 + \frac{1}{2} \left(\frac{\partial u_i}{\partial x_j} + \frac{\partial u_j}{\partial x_i} \right) dx_j + \frac{1}{2} \left(\frac{\partial u_i}{\partial x_j} - \frac{\partial u_j}{\partial x_i} \right) dx_j, \quad (2.5)$$

or

$$u_i = u_i^0 + \varepsilon_{ij} dx_j + \omega_{ij} dx_j, \quad (2.6)$$

where

$$\varepsilon_{ij} = \frac{1}{2} \left(\frac{\partial u_i}{\partial x_j} + \frac{\partial u_j}{\partial x_i} \right), \quad (2.7)$$

is the strain tensor, and

$$\omega_{ij} = \frac{1}{2} \left(\frac{\partial u_i}{\partial x_j} - \frac{\partial u_j}{\partial x_i} \right), \quad (2.8)$$

is the rotation tensor.

2.4 Constitutive Equations

2.4.1 Stress, strain and elasticity tensors

The stress and strain in an elastic material under small deformations may be related, in terms of their Cartesian components, as:

$$\sigma_{ij} = C_{ijkl} \varepsilon_{kl}, \quad (2.9)$$

which is a generalized form of Hooke's law; here C_{ijkl} is the rank-four elasticity tensor which describes the behavior of the material under general loading.

Voigt notation can be used to compactly represent the elasticity tensor as a 6×6 matrix (the “elasticity matrix” or “stiffness matrix”), allowing Equation 2.9 to become:

$$\begin{bmatrix} \sigma_{11} \\ \sigma_{22} \\ \sigma_{33} \\ \sigma_{23} \\ \sigma_{13} \\ \sigma_{12} \end{bmatrix} = \begin{bmatrix} c_{11} & c_{12} & c_{13} & c_{14} & c_{15} & c_{16} \\ & c_{22} & c_{23} & c_{24} & c_{25} & c_{26} \\ & & c_{33} & c_{34} & c_{35} & c_{36} \\ & & & c_{44} & c_{45} & c_{46} \\ & \text{sym.} & & & c_{55} & c_{56} \\ & & & & & c_{66} \end{bmatrix} \begin{bmatrix} \varepsilon_{11} \\ \varepsilon_{22} \\ \varepsilon_{33} \\ 2\varepsilon_{23} \\ 2\varepsilon_{13} \\ 2\varepsilon_{12} \end{bmatrix} \quad (2.10)$$

2.4.2 Isotropic, linear elastic materials

Using Lamé constants (λ_L, μ), the elasticity matrix for isotropic, elastic materials can be expressed as:

$$C = \begin{bmatrix} \lambda_L + 2\mu & \lambda_L & \lambda_L & 0 & 0 & 0 \\ & \lambda_L + 2\mu & \lambda_L & 0 & 0 & 0 \\ & & \lambda_L + 2\mu & 0 & 0 & 0 \\ & & & \mu & 0 & 0 \\ & \text{sym.} & & & \mu & 0 \\ & & & & & \mu \end{bmatrix}. \quad (2.11)$$

The Lamé constants used in Equation 2.11 can be expressed in terms of the engineering constants: Young's modulus, governing uniaxial tension; Poisson's ratio, governing transverse and axial strain; and shear modulus, governing the response to shear, respectively:

$$E = \frac{\mu(3\lambda+2\mu)}{\lambda_L+\mu}, \nu = \frac{\lambda_L}{2(\lambda_L+\mu)}, \text{ and } \mu = \frac{E}{2(1+\nu)}. \quad (2.12-14)$$

Using these terms, the compliance tensor can be expressed in Voigt notation as:

$$S = \frac{\lambda_L + \mu}{\mu(3\lambda_L + 2\mu)} \begin{bmatrix} 1 & \frac{-\lambda_L}{2(\lambda_L + \mu)} & \frac{-\lambda_L}{2(\lambda_L + \mu)} & 0 & 0 & 0 \\ \frac{-\lambda_L}{2(\lambda_L + \mu)} & 1 & \frac{-\lambda_L}{2(\lambda_L + \mu)} & 0 & 0 & 0 \\ \frac{-\lambda_L}{2(\lambda_L + \mu)} & \frac{-\lambda_L}{2(\lambda_L + \mu)} & 1 & 0 & 0 & 0 \\ 0 & 0 & 0 & 2(1 + \nu) & 0 & 0 \\ 0 & 0 & 0 & 0 & 2(1 + \nu) & 0 \\ 0 & 0 & 0 & 0 & 0 & 2(1 + \nu) \end{bmatrix} = \begin{bmatrix} \frac{1}{E} & \frac{-\nu}{E} & \frac{-\nu}{E} & 0 & 0 & 0 \\ \frac{-\nu}{E} & \frac{1}{E} & \frac{-\nu}{E} & 0 & 0 & 0 \\ \frac{-\nu}{E} & \frac{-\nu}{E} & \frac{1}{E} & 0 & 0 & 0 \\ 0 & 0 & 0 & \frac{1}{\mu} & 0 & 0 \\ 0 & 0 & 0 & 0 & \frac{1}{\mu} & 0 \\ 0 & 0 & 0 & 0 & 0 & \frac{1}{\mu} \end{bmatrix} \quad (2.15)$$

We can now write the linear elastic constitutive law in compact indicial notation for isotropic materials:

$$\sigma_{ij} = \lambda_L \varepsilon_{kk} \delta_{ij} + 2 \mu \varepsilon_{ij} . \quad (2.16)$$

2.4.3 Anisotropic (transversely isotropic) materials

The simplest anisotropic material is a transversely isotropic material model, where material properties are invariant to rotation about an axis normal to the plane of isotropy. We define such a material, with an axis defining the fiber direction, \mathbf{x}_1 , and \mathbf{A} as the unit vector in the fiber direction.

The deformation gradient is defined as:

$$\mathbf{F} = \frac{\partial \mathbf{x}}{\partial \mathbf{X}}, \quad \text{or} \quad F_{ij} = \frac{\partial x_i}{\partial X_j} \quad (2.17)$$

with \mathbf{X} representing the material vector in the reference configuration and \mathbf{x} representing the corresponding spatial vector in the deformed configuration. The right Cauchy-Green tensor is defined as:

$$\mathbf{C} = \mathbf{F}^T \mathbf{F}. \quad (2.18)$$

The volume ratio between the deformed and undeformed configurations is given by:

$$J = \det(\mathbf{F}). \quad (2.19)$$

And the principal invariants are given by:

$$I_1 = \text{tr}(\mathbf{C}), I_2 = \frac{1}{2}(\text{tr}(\mathbf{C})^2 - \text{tr}(\mathbf{C}^2)), I_3 = \det(\mathbf{C}) = J^2, I_4 = \mathbf{A} \cdot \mathbf{C} \mathbf{A}, \text{ and } I_5 = \mathbf{A} \cdot \mathbf{C}^2 \mathbf{A}. \quad (2.20-25)$$

A strain energy density function for nearly incompressible, transversely isotropic (NITI) elastic materials can be described by (Feng et al., 2013b):

$$W = \frac{\mu}{2}[(\bar{I}_1 - 3) + \zeta(\bar{I}_4 - 1)^2 + \phi \bar{I}_5^*] + \frac{\kappa}{2}(J - 1)^2. \quad (2.26)$$

Where $\bar{I}_1 = J^{-2/3} I_1$ and describes deformation, $\bar{I}_4 = J^{2/3}$ and describes fiber stretch, $\bar{I}_5 = J^{-4/3} I_5$ and describes fiber-matrix interaction. \bar{I}_5^* is defined as the isochoric pseudo-invariant, which contains no contribution from fiber stretch $\bar{I}_5^* = \bar{I}_5 - \bar{I}_4^2$. The last term $(\frac{\kappa}{2}(J - 1)^2)$ describes volumetric strain.

The components of the elasticity tensor of a nearly incompressible, transversely isotropic (NITI) material model (Feng et al., 2013b), are given below in Voigt notation. The fiber direction is assigned to be $\mathbf{a} = \mathbf{e}_1 = [1 \ 0 \ 0]^T$. The components of the elasticity matrix in Equation 2.10 are:

$$c_{11} = \kappa + \frac{4}{3}\mu \left(1 + \frac{4}{3}\zeta\right); \quad c_{22} = c_{33} = \kappa + \frac{4}{3}\mu \left(1 + \frac{1}{3}\zeta\right); \quad (2.27a-b)$$

$$c_{12} = c_{13} = c_{21} = c_{31} = \kappa - \frac{2}{3}\mu \left(1 + \frac{4}{3}\zeta\right); \quad c_{32} = c_{23} = \kappa - \frac{2}{3}\mu \left(1 - \frac{2}{3}\zeta\right); \quad (2.28a-b)$$

$$c_{44} = \mu; \quad c_{55} = c_{66} = \mu(1 + \phi). \quad (2.29a-b)$$

where μ is the shear modulus, κ is the bulk modulus, ϕ is the shear anisotropy, and ζ is the tensile anisotropy (Feng et al., 2013b). The compliance matrix, which is the inverse of the elasticity matrix in Voigt notation, is shown below using the current notation and in standard engineering nomenclature.

$$S = \begin{bmatrix} \frac{1}{\mu(4\zeta+3)} + \frac{1}{9\kappa} & \frac{-1}{2\mu(4\zeta+3)} + \frac{1}{9\kappa} & \frac{-1}{2\mu(4\zeta+3)} + \frac{1}{9\kappa} & 0 & 0 & 0 \\ \frac{-1}{2\mu(4\zeta+3)} + \frac{1}{9\kappa} & \frac{1+\zeta}{\mu(4\zeta+3)} + \frac{1}{9\kappa} & \frac{-(1+2\zeta)}{2\mu(4\zeta+3)} + \frac{1}{9\kappa} & 0 & 0 & 0 \\ \frac{-1}{2\mu(4\zeta+3)} + \frac{1}{9\kappa} & \frac{-(1+2\zeta)}{2\mu(4\zeta+3)} + \frac{1}{9\kappa} & \frac{1+\zeta}{\mu(4\zeta+3)} + \frac{1}{9\kappa} & 0 & 0 & 0 \\ 0 & 0 & 0 & \frac{1}{\mu} & 0 & 0 \\ 0 & 0 & 0 & 0 & \frac{1}{\mu(1+\phi)} & 0 \\ 0 & 0 & 0 & 0 & 0 & \frac{1}{\mu(1+\phi)} \end{bmatrix} =$$

$$\begin{bmatrix} \frac{1}{E_1} & -\frac{\nu_{21}}{E_2} & -\frac{\nu_{21}}{E_2} & 0 & 0 & 0 \\ -\frac{\nu_{12}}{E_1} & \frac{1}{E_2} & -\frac{\nu_2}{E_2} & 0 & 0 & 0 \\ -\frac{\nu_{12}}{E_1} & -\frac{\nu_2}{E_2} & \frac{1}{E_2} & 0 & 0 & 0 \\ 0 & 0 & 0 & \frac{1}{\mu_2} & 0 & 0 \\ 0 & 0 & 0 & 0 & \frac{1}{\mu_1} & 0 \\ 0 & 0 & 0 & 0 & 0 & \frac{1}{\mu_1} \end{bmatrix}. \quad (2.30)$$

In the incompressible limit, as bulk modulus becomes large ($\kappa \rightarrow \infty$), the components of the compliance matrix approach finite, well-defined limits that correspond clearly to standard

engineering constants (see Table 2.1). The relationships between these parameters allow us to define the following:

$$\phi = \frac{\mu_1}{\mu_2} - 1 \text{ and } \zeta = \frac{E_1}{E_2} - 1. \quad (2.31-32)$$

which describe the relative difference in shear moduli and the relative difference between Young's (tensile) moduli in NITI materials.

2.5 Harmonic plane wave propagation

2.5.1 General

For elastic plane waves traveling in a nearly incompressible TI (NITI) material, the assumed plane wave solution:

$$u_i = u_0 m_i \exp[I(K n_j x_j - \omega t)], \quad (2.33)$$

satisfies the equation of motion (EOM):

$$\frac{\partial \sigma_{ij}}{\partial x_i} = \rho \frac{\partial^2 u_j}{\partial t^2}. \quad (2.34)$$

Here $\frac{\partial \sigma_{ij}}{\partial x_i}$ is the divergence of the second order stress tensor, σ_{ij} , u_0 is the amplitude of the

displacement, $m_i = [m_1 \ m_2 \ m_3]^T$ is the polarization direction of the displacement, $n_i =$

$[n_1 \ n_2 \ n_3]^T$ is the propagation direction, K is the wavenumber, I is the imaginary number

($\sqrt{-1}$), ω is the excitation frequency, and ρ is the density (Holzapfel, 2000, pp. 144-145).

Substitution of the assumed solution (Eq. 2.34) and the constitutive law (Eq. 2.2) into the EOM results in the eigenvalue problem:

$$Q(\mathbf{n}) \cdot \mathbf{m} = \rho c^2 \mathbf{m}, \quad \text{or} \quad Q_{ij} m_j = \rho c^2 m_i \quad (2.35)$$

where \mathbf{Q} is the acoustic tensor with Cartesian components $Q_{ij} = C_{piqj}n_p n_q$, C_{piqj} are the elements of the elasticity tensor and c is the wave speed. The solution of this eigenvalue problem yields three eigenvalues $\lambda = \rho c^2$ and eigenvectors m_i .

2.5.2 Wave speeds in an isotropic medium

For the isotropic case, the acoustic tensor is:

$$\mathbf{Q} = \begin{bmatrix} \lambda_L + 2\mu & 0 & 0 \\ 0 & \mu & 0 \\ 0 & 0 & \mu \end{bmatrix}. \quad (2.36)$$

Assuming a wave propagation direction of $n_i = [1 \ 0 \ 0]^T$, there are three eigenvalues corresponding to three independent wave polarization directions, $m_1 = [1,0,0]$, $m_2 = [0,1,0]$ and $m_3 = [0,0,1]$, which are given by:

$$\Lambda_1 = \rho c_1^2 = (\lambda_L + 2\mu), \quad \Lambda_2 = \rho c_2^2 = \mu, \quad \Lambda_3 = \rho c_3^2 = \mu. \quad (2.37a-c)$$

Wave speeds through an isotropic material can then be shown to be:

$$c_1^2 = \frac{(\lambda + 2\mu)}{\rho}, \quad c_2^2 = c_3^2 = \frac{\mu}{\rho}. \quad (2.38a-b)$$

Where c_1 corresponds to the longitudinal wave speed through an isotropic medium and c_2 and c_3 both correspond to shear wave speeds. Since the material is isotropic, given two separate wave polarizations (m_2 and m_3), the shear wave speed is equivalent.

2.5.3 Wave speeds and polarizations in a transversely isotropic medium

Without loss of generality, we assume the propagation direction remains in the 1-2 plane and can be defined by $n_i = [\cos(\theta) \ \sin(\theta) \ 0]^T$ for a transversely isotropic solid. Substituting n_i and the elastic tensor terms from Eqs. 2.8-2.9 gives the acoustic tensor in the form of:

$$\mathbf{Q} = \begin{bmatrix} \left(\kappa + \frac{4\mu}{3} + \frac{16\mu\zeta}{9}\right) \cos^2(\theta) + \mu(1 + \phi) \sin^2(\theta) & \left(\kappa + \frac{\mu}{3} + \mu\phi - \frac{8\mu\zeta}{9}\right) \cos(\theta) \sin(\theta) & 0 \\ \left(\kappa + \frac{\mu}{3} + \mu\phi - \frac{8\mu\zeta}{9}\right) \cos(\theta) \sin(\theta) & \left(\kappa + \frac{4\mu}{3} + \frac{16\mu\zeta}{9}\right) \sin^2(\theta) + \mu(1 + \phi) \cos^2(\theta) & 0 \\ 0 & 0 & \mu(1 + \phi) \cos^2(\theta) + \mu \sin^2(\theta) \end{bmatrix}. \quad (2.39)$$

In the limit of $\kappa \rightarrow \infty$ (i.e., for an incompressible material), the eigenvalues are given by:

$$\begin{aligned} \Lambda_1 &= \rho c_s^2 = \mu(1 + \phi \cos^2 \theta), \quad \Lambda_2 = \rho c_f^2 = \mu(1 + \phi \cos^2 2\theta + \zeta \sin^2 2\theta), \\ \Lambda_3 &= \rho c_p^2 \rightarrow \infty, \end{aligned} \quad (2.40a-c)$$

where c_s is the slow shear wave speed, c_f is the fast shear wave speed, and c_p is the longitudinal wave speed. The wave speeds approach these approximations closely for finite values of bulk modulus representative of soft tissue (within 1-2% for $\kappa \approx 100\mu$; Tweten et al., 2015). The corresponding eigenvectors \mathbf{m}_i are the polarization directions: $\mathbf{m}_1 = \mathbf{m}_s$, $\mathbf{m}_2 = \mathbf{m}_f$, $\mathbf{m}_3 = \mathbf{m}_p$. The slow and fast shear wave polarization directions can also be defined by the following relationship:

$$\mathbf{m}_s = \frac{\mathbf{n} \times \mathbf{a}}{|\mathbf{n} \times \mathbf{a}|} \text{ and } \mathbf{m}_f = \mathbf{n} \times \mathbf{m}_s, \quad (2.41a-b)$$

where \mathbf{a} indicates the plane of isotropy (fiber direction). The wave polarizations, and propagation directions, and fiber orientation are shown relative to a transversely isotropic solid in Figure 2.1.

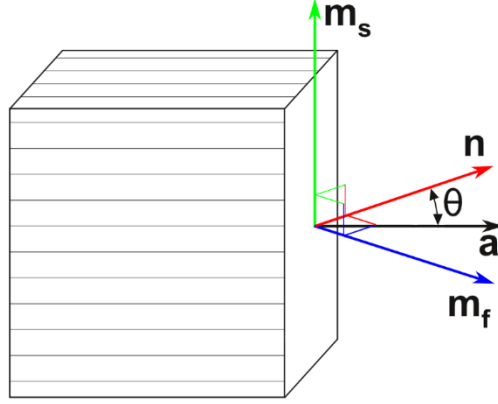


Figure 2.1: The propagation direction (denoted by unit vector \mathbf{n}) and polarization directions (unit vectors \mathbf{m}_s and \mathbf{m}_f) of slow and fast shear waves, respectively, in an incompressible, transversely isotropic, elastic material. The unit vector \mathbf{a} denotes the normal to the plane of isotropy. (Reproduced from: Schmidt et al., 2016)

Note that, as required in linear elasticity:

$$v_{21} = \frac{E_2}{E_1} v_{12}; \quad c_{44} = \frac{c_{33} - c_{32}}{2}. \quad (2.42a-b)$$

In the case of tensile isotropy ($\zeta = 0$):

$$E_1 = E_2 = \frac{9\kappa\mu}{3\kappa + \mu}; \quad v_{12} = v_{21} = v_2 = \frac{3\kappa - 2\mu}{2(3\kappa + \mu)}. \quad (2.43a-b)$$

$$\text{As } \kappa \rightarrow \infty: \quad E_1 = E_2 = 3\mu; \quad v_{12} = v_{21} = v_2 = \frac{1}{2}. \quad (2.44a-b)$$

In the case of shear isotropy ($\phi = 0$):

$$\mu_1 = \mu_2 = \mu. \quad (2.45)$$

In the incompressible limit ($\kappa \rightarrow \infty$) the components of the compliance matrix approach finite, well-defined limits that correspond clearly to standard engineering constants (Table 2.1).

Common nomenclature	Current nomenclature $\left[\Delta = \frac{\mu(4\zeta+3)}{9\kappa} \right]$	Incompressible limit ($\kappa \rightarrow \infty, \Delta \rightarrow 0$)
Quasi-transverse (QT) shear wave	Fast shear wave	$c_s^2 = \frac{\mu}{\rho} (1 + \phi \cos^2 \theta)$
Pure transverse (PT) shear wave	Slow shear wave	$c_f^2 = \frac{\mu}{\rho} (1 + \phi \cos^2 2\theta + \zeta \sin^2 2\theta)$
c_{11}	$\kappa + \mu \left(\frac{4}{3} + \frac{16\zeta}{9} \right)$	∞
c_{22}, c_{33}	$\kappa + \mu \left(\frac{4}{3} + \frac{4\zeta}{9} \right)$	∞
$c_{12}, c_{13}, c_{21}, c_{31}$	$\kappa - \mu \left(\frac{2}{3} + \frac{8\zeta}{9} \right)$	∞
c_{23}, c_{32}	$\kappa - \mu \left(\frac{2}{3} - \frac{4\zeta}{9} \right)$	∞
$c_{44}, \mu_2, \mu_T, \mu_{\perp}$	μ	μ
$c_{55}, c_{66}, \mu_1, \mu_L, \mu_{\parallel}$	$\mu(1 + \phi)$	$\mu(1 + \phi)$
E_1	$\frac{\mu(4\zeta+3)}{1+\Delta}$	$\mu(4\zeta + 3)$
E_2	$\frac{\mu(4\zeta+3)}{1+\zeta+\Delta}$	$\frac{\mu(4\zeta+3)}{1+\zeta}$
ν_{12}	$\frac{1-2\Delta}{2+2\Delta}$	$\frac{1}{2}$
ν_{21}	$\frac{1-2\Delta}{2(1+\zeta)+2\Delta}$	$\frac{1}{2(1+\zeta)}$
$\nu_{23}, \nu_{32}, \nu_2$	$\frac{1+2\zeta-2\Delta}{2(1+\zeta)+2\Delta}$	$\frac{1+2\zeta}{2(1+\zeta)}$

Table 2.1: Common nomenclature and relationship to nomenclature in this study.

2.6 Shear wave propagation in media under finite deformation

Thus far, shear waves have been described while propagating in an undeformed material, dependent on the elasticity tensor. Characterizing material that is highly deformed, however, is of interest when studying the material properties of tissues under injurious conditions. When describing the behavior of a hyperelastic material described by strain energy density function, the elasticity tensor of that material depends on the deformation gradient tensor; thus deformation

influences shear wave speeds. This topic is further discussed in Chapter 5 with analytical and computer simulation results.

2.7 Imaging Methods and Analysis

2.7.1 Introduction

The previous sections of this chapter have been devoted to the theoretical explanation of propagating waves in a soft, elastic solid; this section describes a method to visualize these shear waves experimentally. Few methods exist to noninvasively measure three-dimensional strain within materials (Kolsky, 1963). MRE is one such method to quantify material deformations in three dimensions.

2.7.2 Magnetic resonance imaging (MRI)

MRI signal is acquired from the spin precession of hydrogen nuclei in a large (fixed) magnetic field, usually referred to as the \mathbf{B}_0 field. Spins are modulated by the magnetic field gradients located within the large magnet bore, and the modulated frequency and phase of the precessions are correlated with spatial location in the magnetic field. These techniques are most frequently used for anatomical imaging of biological tissue, however, manipulation of spin precession amplitude and phase can also be used to measure tissue displacement and motion, through phase contrast imaging. Diffusion (of H^1 protons) within biological tissue can also be imaged utilizing phase contrast, in a method known as diffusion tensor imaging (DTI).

2.7.3 Magnetic resonance elastography (MRE)

In an MRE study, displacements from harmonic motion applied to a sample are measured from phase image “snapshots” of the propagating wave. To perform this, the magnetic field within the MRI scanner is modulated via the gradient field of the magnet in sync with the harmonic motion

applied to the sample (Muthupillai et al., 1995a). An example MR pulse diagram is shown in Figure 2.2.

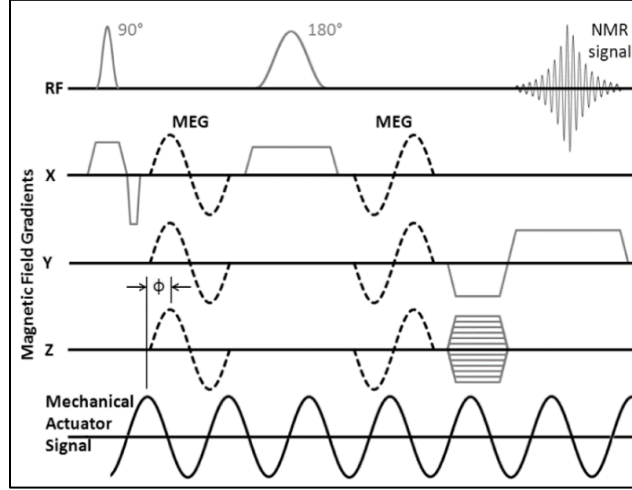


Figure 2.2: A modified spin-echo MRE pulse diagram. (Clayton et al., 2011a)

As MRE is a phase-contrast imaging method, phase accumulated must be converted to a non-arbitrary displacement unit. From a typical MRE sequence, each voxel in the image space will have a vector of motion-induced phase, $\boldsymbol{\varphi}(x_1, x_2, x_3)$, proportional to displacement, $\mathbf{u}(x_1, x_2, x_3)$, obtained from the MRE sequence (Muthupillai et al., 1995a). The 3D position of a material element of a substance such as water with nuclear spin (a “spin-packet”) is given by:

$$\mathbf{r} = \mathbf{r}_0 + \mathbf{u} \quad (2.46)$$

and:

$$\mathbf{u} = \mathbf{u}_0 \cos(\omega t - \mathbf{k} \cdot \mathbf{r}_0 + \theta), \quad (2.47)$$

where \mathbf{u}_0 , \mathbf{r}_0 , ω , \mathbf{k} and θ are the vibration displacement (m), the initial position of the spin-packet (m), vibration frequency (rad/s), spatial frequency vector (rad/m), and the vibration phase

(rad) respectively. It follows (Atay et al., 2008; Muthupillai et al., 1995a) that the component of the MR phase vector in the direction of the gradient, \mathbf{G} , is:

$$\varphi_G(\mathbf{r}_o, \theta) = \gamma \int_0^{2\pi N/\omega} (\mathbf{G} \cdot \mathbf{r}) dt = \frac{\gamma \pi N (\mathbf{G}_0 \cdot \mathbf{u}_0)}{\omega} \cos(\theta - \mathbf{k} \cdot \mathbf{r}_0), \quad (2.48)$$

where $\mathbf{G} = \mathbf{G}_0 \cos(\omega t)$ (Gauss/m or T/m) is the motion-encoding magnetic field gradient, applied in a sinusoidal fashion, γ (rad/s/T) is the gyro-magnetic ratio of water, and N is the number of motion-encoding gradient cycles used in the specific MRE sequence. Equation 2.48 can be simplified to the form of a proportional constant, C , directly relating MR phase to displacement:

$$\mathbf{u}(\mathbf{r}_0, \theta) = C \boldsymbol{\varphi}(\mathbf{r}_0, \theta). \quad (2.49)$$

Because of the sequential method (one direction at a time, $i = 1, 2, 3$) in which the gradients are applied during the sequence, the coefficient of proportionality (m/rad) can be expressed in terms of the i^{th} direction:

$$C_i = \frac{u_{\max,i}}{\varphi_{\max,i}} = \frac{\omega}{\gamma \pi N G_{0,i}}, \quad (2.50)$$

Here $G_{0,i}$ is the gradient amplitude in the respective direction. Example MRE experimental and simulated data are shown in Figures 2.3 and 2.4, respectively.

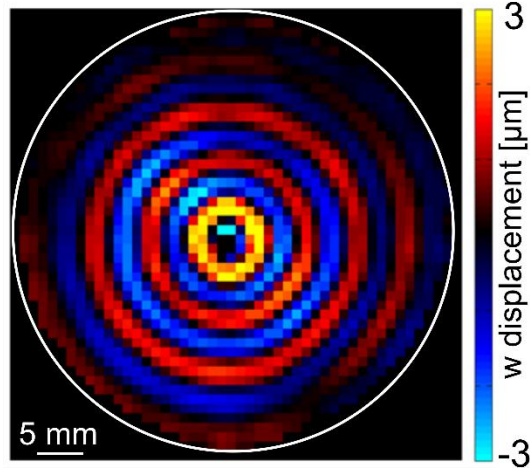


Figure 2.3: Experimental MRE displacement data acquired in gelatin/glycerol (isotropic, Okamoto et al., 2011) at 200 Hz mechanical actuation.

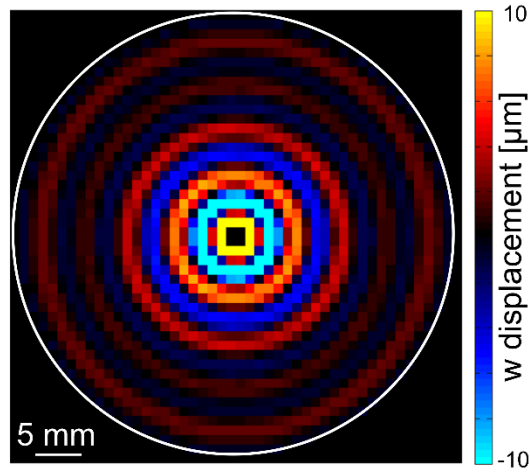


Figure 2.4: Simulated harmonic displacement data in a material representing gelatin ($\mu = 1.1$ kPa, $\rho = 1100$ kg/m³) at 200 Hz mechanical actuation.

2.7.4 Estimation of material parameters in MRE

Local frequency estimation

For isotropic materials, shear wavelength (λ) in an infinite mechanically isotropic medium is directly related to the shear modulus (μ):

$$\lambda = \frac{1}{f} \sqrt{\frac{\mu}{\rho}}, \quad (2.51)$$

and with rearranging gives:

$$\mu = \rho(f\lambda)^2, \quad (2.52)$$

where f is the frequency of the wave and ρ is the material density. Local frequency estimation (LFE), which relies on estimating the local spatial frequency of shear wave propagation, provides a simple, approximate method for the estimation of material properties from MRE data (Knutsson et al., 1994; Manduca et al., 1996). Local frequency estimates are found by applying a series of spatial filters, which are a product of radial and directional components. Assuming only shear waves are imaged, the shear wavelength is found from the dominant wavenumber (k) in the imaging domain (length L):

$$\lambda = \frac{L}{k}. \quad (2.53)$$

Referring to example MRE simulated data in Figure 2.4, we can show results from the application of LFE in Figure 2.5.

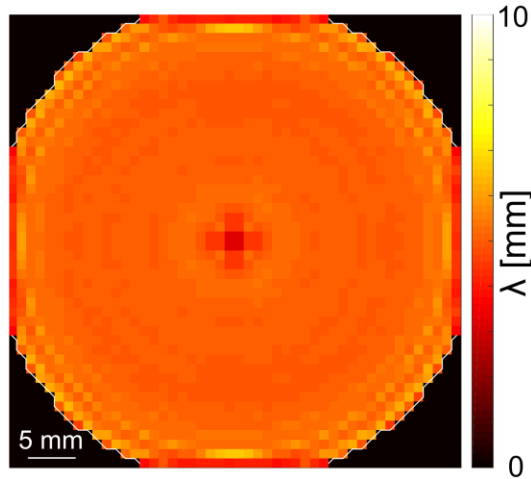


Figure 2.5: Simulated harmonic displacement data in a material representing gelatin ($\mu = 1.1$ kPa, $\rho = 1100$ kg/m³) at 200 Hz mechanical actuation.

Local direct inversion

Displacement fields acquired by an MRE sequence can be fitted to the elastic wave equations. This method is known as direct inversion (and for regional estimates, local direct inversion or LDI; Okamoto et al., 2011). LDI can be used to fit experimental data to an isotropic, linear viscoelastic model using the correspondence principle (Clayton et al., 2011a). In this approach, the shear modulus, μ , is replaced by a complex parameter, μ^* :

$$\mu = \mu^*(i\omega) = \mu'(\omega) + i\mu''(\omega), \quad (2.54)$$

where μ' refers to the shear storage modulus, μ'' refers to the shear loss modulus, and ω is the frequency of the wave. The linear, isotropic, locally homogeneous, viscoelastic Navier equation is expressed as:

$$(\mu' + i\mu'')\nabla^2 \mathbf{U}(x, y, z, \omega) = -\rho\omega^2 \mathbf{U}(x, y, z, \omega), \quad (2.55)$$

where ρ is the material density, \mathbf{U} refers to the shear wave displacement field acquired during an MRE experiment (after excluding displacements due to rigid body motion and longitudinal waves), and ∇^2 refers to the Laplacian operator. Typically, inversion is performed by total-least squares fitting, fitting data within a kernel of voxels (i.e., 7x7x7 voxels). Referring to example MRE simulated data in Figure 2.4, we can show results from the application of LFE in Figure 2.6.

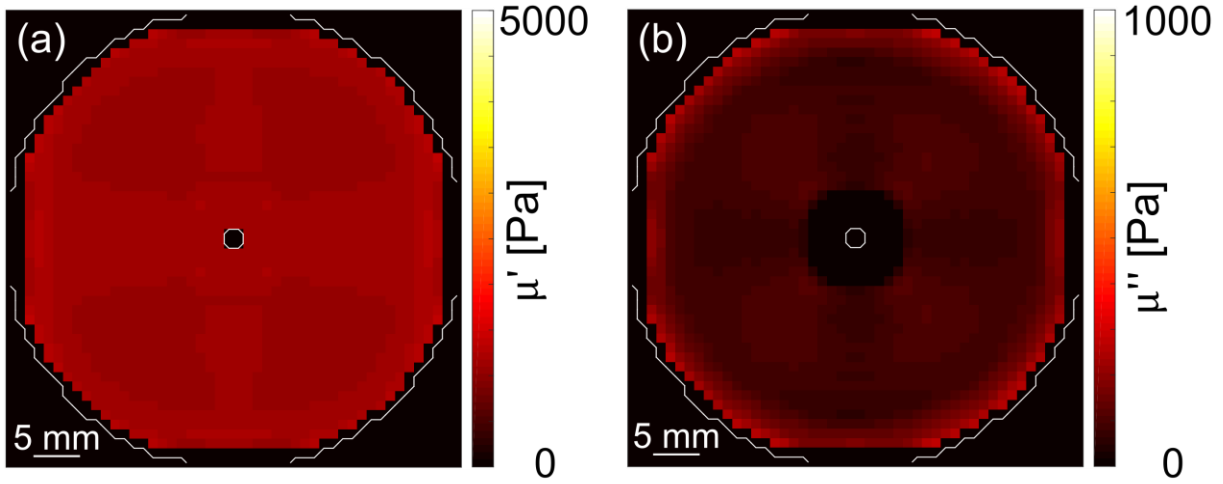


Figure 2.6: Simulated harmonic displacement data in a material representing gelatin ($\mu' = 1.1$ kPa, $\rho = 1100$ kg/m³) at 200 Hz mechanical actuation. (a) Shear storage modulus, μ' . (b) Shear loss modulus, μ'' .

2.8 Summary

Continuum mechanics and dynamics theory have been introduced in this chapter as background for the remainder of this dissertation. Steady-state harmonic wave equations of motion are derived. From the constitutive relationships for isotropic and transversely isotropic, linear, elastic materials, plane wave solutions in a given propagation direction are found from the corresponding acoustic tensor. The extension of these methods to nonlinear materials is introduced briefly. Finally, relevant imaging methods and corresponding material parameter estimation techniques are discussed.

Plane wave solutions for a transversely isotropic material are used to describe and characterize fibrous materials in Chapter 3. In Chapter 4, the behavior of shear waves in transversely isotropic material is used to characterize *ex vivo* white matter brain tissue, comparing data from experiments to results from analogous finite element models to account for non-idealities in the experiment (i.e.: sample size). In Chapter 5, plane wave solutions are derived for deformed,

nonlinear materials and compared to a finite element simulation and experimental methods are proposed.

Chapter 3: Magnetic resonance elastography of slow and fast shear waves illuminates differences in shear and tensile moduli in anisotropic tissue

3.1 Overview

In this chapter, the anisotropic shear and tensile modulus of soft fibrous tissue is characterized using MRE. In contrast to most MRE studies, in which tissue isotropy is assumed and a single shear, or tensile modulus is estimated, this study relies on an incompressible, transversely isotropic (ITI) material model. Such a material is characterized by three parameters: minimum shear modulus (μ), shear anisotropy ($\phi = \mu_1/\mu - 1$) and tensile anisotropy ($\zeta = E_1/E_2 - 1$). Two types of shear waves were visualized using MRE: “fast” (or “quasi-transverse”) and “slow” (or “pure transverse”) shear waves. These waves were analyzed for a given propagation direction to estimate anisotropic parameters μ , ϕ , and ζ in two fibrous soft materials: muscle tissue (turkey breast) *ex vivo* and aligned fibrin gels. As expected, the speed of slow shear waves depended on the angle between fiber direction and propagation direction. Fast shear waves were observed when the deformations due to wave motion induced stretch in the fiber direction. Finally, MRE estimates of anisotropic mechanical properties in turkey breast were compared to estimates from direct mechanical tests.

The material presented in this chapter is published in the Journal of Biomechanics (Schmidt et al., 2016).

3.2 Introduction

Accurate characterization of soft tissue material properties is important to medical clinicians and researchers. The identification of parameters for soft tissue is especially relevant to traumatic brain injury (TBI) research, as it will enable more accurate mechanical modeling and simulation of TBI. Magnetic resonance elastography (MRE) is a technique for non-invasive estimation of material parameters in soft tissues. In MRE, shear waves are excited in the soft tissue; the resulting shear wave speed is measured and used to estimate material parameters. MRE was originally developed using isotropic, elastic material models (Muthupillai et al., 1995b; Muthupillai and Ehman, 1996) and similar isotropic, elastic or viscoelastic models have been used to characterize tissues such as liver (Asbach et al., 2008; Klatt et al., 2010a; Mariappan et al., 2009), breast (Sinkus et al., 2005a), and brain (Atay et al., 2008; Clayton et al., 2011a; Feng et al., 2013a; Green et al., 2008; Johnson et al., 2013; Murphy et al., 2013; Sack et al., 2008). However, since biological tissue is often anisotropic (Feng et al., 2013b), techniques used in MRE should be extended to account for directionally-dependent material properties.

For a summary of elastography studies utilizing anisotropic material models, refer to Chapter 1, specifically section 1.3.2 and material parameter estimation using MRE.

While recent studies have illustrated the plausibility of different approaches to estimate parameters for TI material models, several key issues remain to be addressed. In most studies,

the performance of the anisotropic inversion algorithm has not been validated, either by using data from simulations or from phantoms with known anisotropic properties. The notable exception is the study of Qin and co-workers (Qin et al., 2013), which found close agreement between MRE and direct measurements of shear anisotropy. Most importantly, in prior experimental work, the criterion that both slow (pure transverse, or PT) and fast shear (quasi-transverse, or QT) waves must be present (at significant amplitudes, with multiple directions) in the estimation region in order to estimate accurately all three ITI parameters (Tweten et al., 2015) was not explicitly met. Many studies did not take into account the effects of tensile moduli on the fast shear-wave speed.

In this study, we explicitly separate wave fields into fast and slow components in multiple propagation directions. We estimate the two separate wave speeds occurring in transversely isotropic soft tissues and show how these wave speeds can be used to estimate the three elastic material parameters for a linear ITI model.

3.3 Methods

3.3.1 Theory: fast and slow shear-wave speeds in elastic, incompressible, transversely isotropic materials

In a linear ITI material model, there are three independent material parameters: shear modulus μ , shear anisotropy $\phi = \mu_1/\mu - 1$, and tensile anisotropy $\zeta = E_1/E_2 - 1$ (other parameters, which are linear combinations of these, can also be chosen). “Slow” (PT) shear waves in ITI materials exhibit displacements perpendicular to both the wave propagation direction, \mathbf{n} , and the normal to the plane of isotropy (nominally the fiber direction), \mathbf{a} . The unit vector in the direction of

displacement, or polarization direction, of the slow wave can be shown to be (Rouze et al., 2013; Tweten et al., 2015):

$$\mathbf{m}_s = \mathbf{n} \times \mathbf{a} / |\mathbf{n} \times \mathbf{a}|. \quad (3.1)$$

(The special case when \mathbf{n} and \mathbf{a} are parallel, is discussed below). Since the slow shear-wave polarization is always perpendicular to the fiber direction, it does not stretch the fibers and wave speed depends only on the baseline shear modulus, μ , shear anisotropy, ϕ , and the angle, θ , between \mathbf{n} and \mathbf{a} :

$$c_s^2 = (\mu/\rho)(1 + \phi \cos^2 \theta). \quad (3.2)$$

The polarization direction of a “fast” (QT) shear wave is perpendicular to both the propagation direction and the slow shear wave polarization direction and lies in the plane defined by \mathbf{n} and \mathbf{a} (Rouze et al., 2013; Tweten et al., 2015):

$$\mathbf{m}_f = \mathbf{n} \times \mathbf{m}_s \quad (3.3)$$

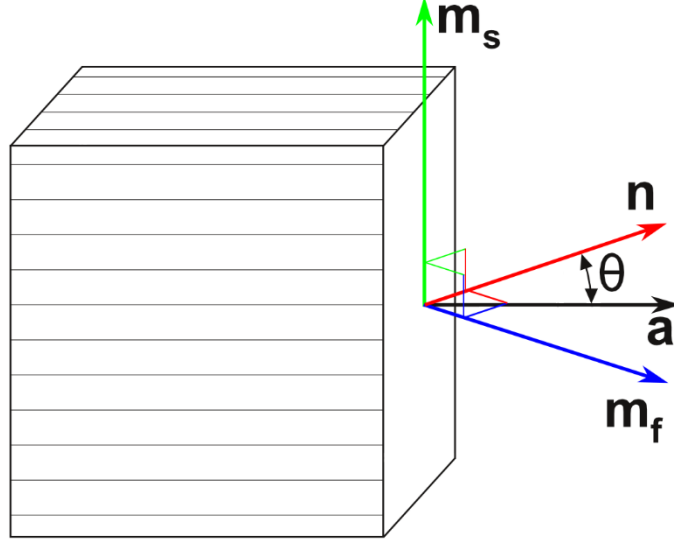


Figure 3.1: The propagation direction (denoted by unit vector \mathbf{n}) and polarization directions (unit vectors \mathbf{m}_s and \mathbf{m}_f) of slow and fast shear waves, respectively, in an incompressible, transversely isotropic, elastic material. The unit vector \mathbf{a} denotes the normal to the plane of isotropy.

Fig. 3.1 shows the relationship between \mathbf{m}_s , \mathbf{m}_f , \mathbf{n} and \mathbf{a} . Deformations associated with fast shear waves induce stretch in the fiber direction, and the speed of the fast shear wave thus depends on the tensile anisotropy, ζ (Tweten et al., 2015):

$$c_f^2 = (\mu/\rho)(1 + \phi \cos^2 2\theta + \zeta \sin^2 2\theta). \quad (3.4)$$

Note that when the propagation direction \mathbf{n} is parallel to the fiber direction \mathbf{a} , Eq. 3.1 and Eq. 3.3 are undefined, $\theta = 0$, and there is only one wave speed.

To extend the theory above to viscoelastic materials, the correspondence principle (Flügge, 1975) may be invoked, in which the complex shear modulus, $\mu^* = \mu' + i\mu''$, describes the relationship between harmonic stress and strain in the plane of isotropy. If dissipative effects are due to fluid motion, and thus approximately isotropic, the loss factor $\eta = \mu''/\mu'$ would govern waves in all directions. In this study, each material is studied at a single frequency, so that μ

represents the magnitude of the complex modulus $|\mu^*|$, and ϕ and ζ the anisotropy in moduli, at that frequency.

3.3.2 Experiments: slow and fast shear waves in cylindrical and cube specimens

Two different fibrous, biological materials, turkey breast and magnetically aligned fibrin gel, were studied to assess wave speed differences in tissue based on fiber orientation. Two sample geometries, cylindrical and cube, were used for each material (Fig. 3.2). (1) Turkey breast was acquired from a retail butcher and tested 3-5 days post-mortem. Samples were cooled during cutting and handling. (2) Fibrin gels with magnetically aligned fibrils were produced in the lab. Human plasminogen-free fibrinogen (EMD Millipore, Billerica, Massachusetts, USA, product no. 34157) and thrombin (Sigma-Aldrich, St. Louis, MO, product no. T4648) were mixed and polymerized following steps outlined in Namani et al. (2012). Polymerization and alignment of the fibrin-thrombin mixture was performed within the bore of an 11.7 T MRI magnet (Agilent/Magnex, Santa Clara, CA). Polymerization time was 90 minutes total; 60 minutes semi-immersed in a custom built thermal chamber filled with ice at 0° C, and the remaining 30 minutes in the same bath while being warmed with water tubing at 40°C.

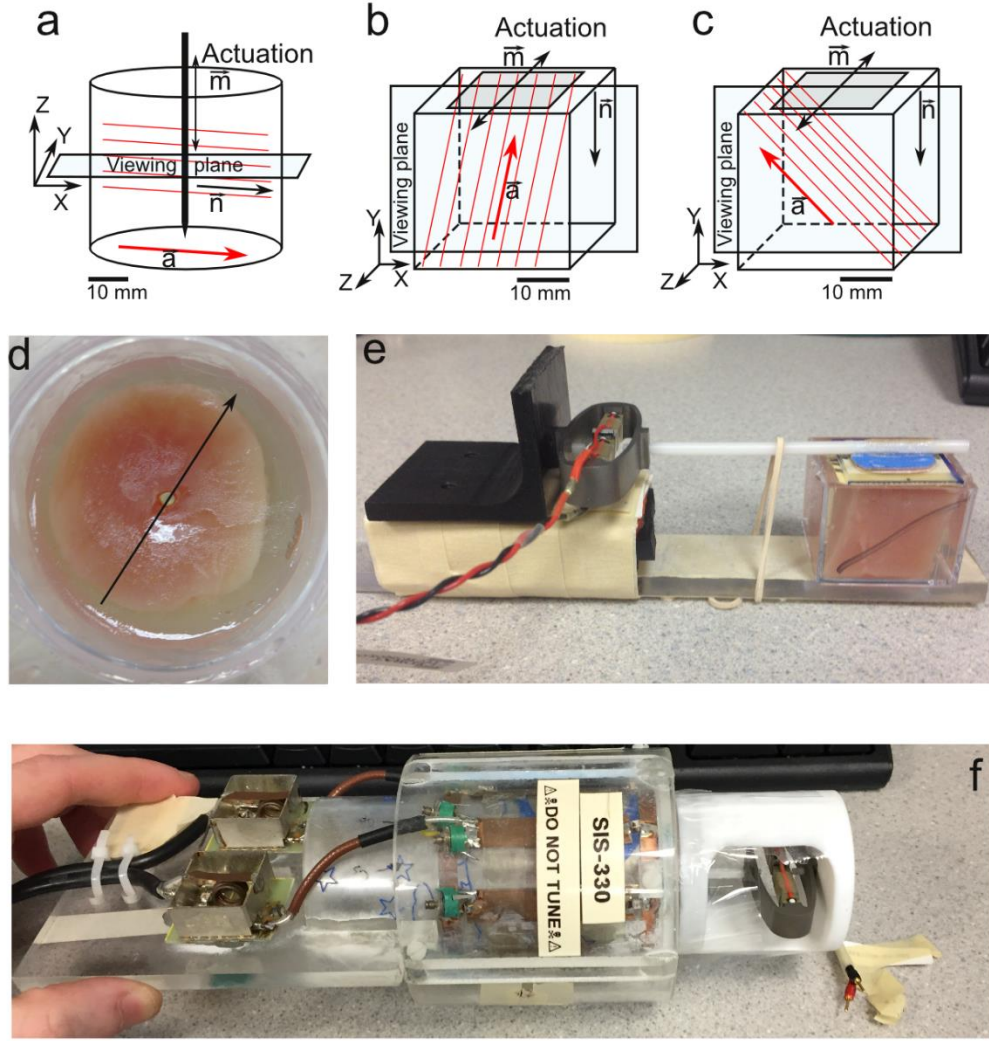


Figure 3.2: Schematic diagrams of: (a) cylindrical specimen with axial excitation; (b) cube specimen with tangential excitation in a plane parallel to the fiber direction to induce “fast” shear waves. (c) cube specimen with tangential excitation perpendicular to the dominant fiber direction to induce “slow” shear waves. (d) photograph of cylindrical turkey breast specimen embedded in gelatin (corresponding to panel a). (e) photograph of experimental setup for cube turkey breast (corresponding to panel b; actuator on left). (f) photograph of a cylindrical sample placed in RF coil with actuator on right.

Cylindrical (45 mm diameter) samples of both turkey breast and fibrin gel were embedded in a gelatin mixture including food grade gelatin (Knox) and 50% / 50% water/glycerol (Okamoto et al., 2011a) in a cylindrical container (48 mm inner diameter; Fig. 3.2 (a, d, f)). Sample thickness ranged from 13-25 mm and the remaining length of the cylinder was filled with the gelatin

mixture. Samples were imaged at ambient ($\sim 20^\circ\text{C}$) temperature. A 3-mm diameter Delrin rod embedded in the center of the specimen provided axial excitation. A piezoelectric actuator (Model APA100M-NM, CEDRAT Technologies, Meylan, France) powered by a low-current, high-voltage amplifier (LA75C, Cedrat Technologies, Meylan, France) was used to excite harmonic vibrations of the axial rod. This setup produced shear waves with approximately radial propagation ($\mathbf{n} \approx \mathbf{e}_r$).

Turkey breast cube samples consisted of a $\sim 25 \times 25 \times 25 \text{ mm}^3$ cube of tissue embedded in gelatin in a $31 \times 31 \times 25 \text{ mm}^3$ (LxWxH) plastic container, Fig. 3.2 (b, c, e). The tissue cubes were cut at a $\sim 45^\circ$ angle relative to the fiber direction and placed in the container so that fibers were oriented $\sim 45^\circ$ downward from the top surface. Aligned fibrin gel cube samples were produced by polymerizing the samples directly in a $20 \times 20 \times 20 \text{ mm}^3$ hollow Delrin cube tilted at an angle of 45° from the \mathbf{B}_0 field. An epoxy composite paddle with 80 grit sandpaper was pressed onto the top surface of the sample as shown in Fig. 3.2 (e) and horizontal excitation was applied using the piezo actuator described above, producing shear waves propagating downward ($\mathbf{n} \approx -\mathbf{e}_y$).

Frequencies of actuation were chosen to produce multiple wavelengths in the specimen, and multiple voxels per wavelength. For turkey breast, a consistent 800 Hz was chosen across all experimental specimens. For fibrin gels, 600 Hz was chosen for cubic specimens and 200 Hz was chosen for cylindrical specimens. Two excitation cases (Fig. 3.2 (b, c)) were applied to each cube sample. In one case (Fig. 3.2 (b)) the actuation direction, \mathbf{m} , was aligned with $\mathbf{m}_s = \mathbf{n} \times \mathbf{a}$ to induce slow shear waves and in the other case (Fig. 3.2 (c)) the actuation was aligned with $\mathbf{m}_f = \mathbf{n} \times \mathbf{m}_s$ to induce fast shear waves.

Imaging was performed using a 4.7 T magnet (Oxford Instruments, Oxfordshire, UK) with an Agilent/Varian DirectDrive imaging system. Images of shear-wave propagation in *ex vivo* turkey breast and aligned fibrin gel were acquired using previously-described spin-echo MRE sequences (Clayton et al., 2011a). MRE imaging parameters were: voxel size = 1.0 mm isotropic (all cylindrical samples, turkey breast cubes), voxel size = 0.5 mm (fibrin gel cubes), TR = 1000 ms, TE = 28-39 ms. Image data were interpolated to 0.5x0.5x1.0 mm and 0.25x0.25x0.5 mm resolution for analysis. Multiple (2-8) sinusoidal motion encoding cycles of gradient strength 10-12 G/cm were synchronized with motion to induce phase contrast proportional to displacement. Eight temporal samples were acquired per sinusoidal excitation period, by incrementing the phase delay between the imposed vibration and acquisition. To verify the average fiber orientation in turkey breast, diffusion tensor imaging (DTI) was performed in the same imaging session as MRE (30 directions, $b=2050 \text{ s/mm}^2$). Figure 3.3 shows a three-dimensional diffusion tensor field to indicate the fiber orientation inside a representative cube turkey breast sample. The relatively sparse networks of aligned fibrils in fibrin gels do not constrain water diffusion and thus DTI was not performed on the fibrin gels. Instead the direction of the magnetic field during the magnetic aligning process was physically marked on the sample container and was noted during all tests.

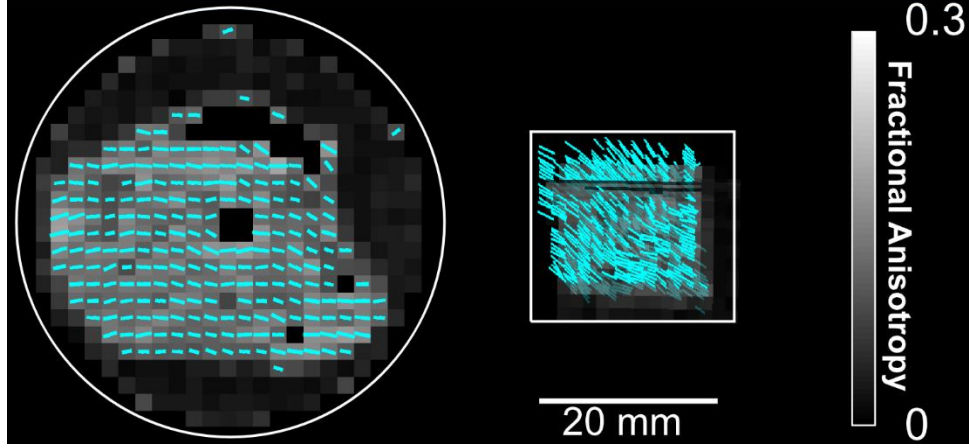


Figure 3.3: Fiber orientation estimated by DTI in (a) cylindrical and (b) cube specimens of turkey breast. Maximum principal diffusion direction vectors (cyan) are superimposed on fractional anisotropy maps (FA, grey) for each voxel.

For comparison with MRE, estimates of viscoelastic shear modulus from dynamic shear testing (DST) were obtained in separate circular samples of turkey breast following techniques in (Feng et al., 2013b; Namani et al., 2012). DST was performed on $N=33$ turkey breast samples with an average sample thickness of 3.91 ± 0.68 mm and sample diameter of 15.3 ± 1.0 mm in both parallel and perpendicular orientations of turkey breast and averaged over the frequencies of 30-40 Hz. This limited frequency range was chosen to avoid inertial effects (shear waves) in the sample. The displacement amplitude for DST in this frequency range was $25 \mu\text{m}$, corresponding to strain magnitudes in the range from 0.005 – 0.01 (0.5% - 1.0%).

3.3.3 Image analysis: characterization of anisotropic wave propagation

First, for a simple measure of anisotropy, radially-propagating shear waves in anisotropic cylindrical specimens were fitted to ellipses (Fig. 3.4). Peaks of the elliptical wavefront in multiple directions were manually picked on the 2D image of axial (w) displacement in the xy

plane, in five contiguous slices from each sample. Ellipses were fitted using an algorithm that minimized the squared-error between the curves and the picked points (Fitzgibbon et al., 1999).

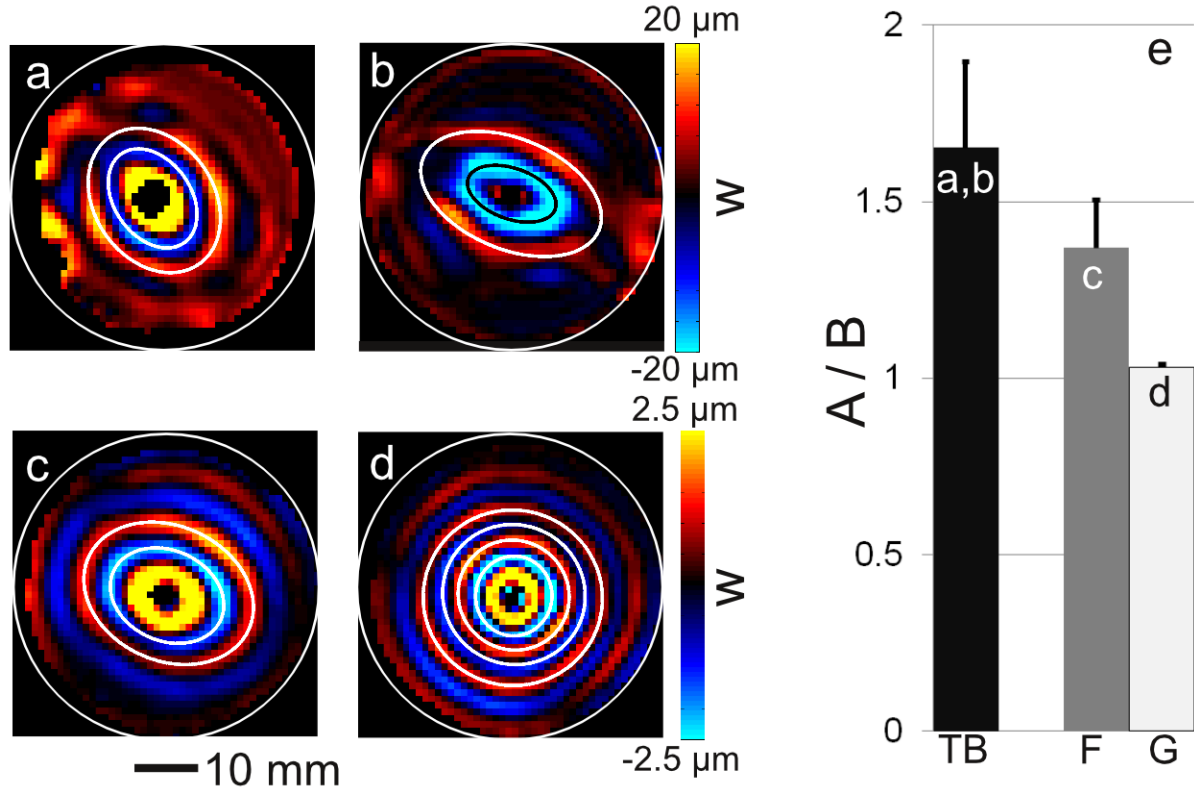


Figure 3.4: Wave propagation in axially-excited, cylindrical specimens. (a-c) Representative images of elliptical waves exhibiting direction-dependent propagation with different wave speeds in different directions. (a) Representative sample #1 of turkey breast, 800 Hz; (b) Representative sample #2 of turkey breast, 800 Hz; (c) aligned fibrin gel, 200 Hz. (d) Circular waves in (isotropic) gelatin, 200 Hz. (e) Ellipses were fitted to the wave images (white and black lines in b-d) and the average ratios of their semi-axes are shown for the different materials.

Second, directional filtering was used to isolate slow and fast shear waves in specific propagation and polarization directions. For each propagation direction, \mathbf{n} , and fiber orientation vector \mathbf{a} , two shear waves exist, with polarization directions \mathbf{m}_s and \mathbf{m}_f obtained from Eq. 3.1 and Eq. 3.3. The displacement field is separated into components of slow and fast shear waves by performing a dot product between the displacement field and the normalized slow and fast

polarization directions: $u_s = \mathbf{u} \cdot \mathbf{m}_s$ and $u_f = \mathbf{u} \cdot \mathbf{m}_f$ (Tweten et al., 2015). The displacement components u_s and u_f were then directionally filtered about the propagation direction, \mathbf{n} , using directional filters with a \cos^2 dependence on angle (Knutsson et al., 1994; Manduca et al., 2003). For cylindrical samples, wave fields were directionally filtered in 16 different directions, at angles of $\theta_{0m} = \frac{m\pi}{8}$ ($m = 1, 2, \dots, 16$) from the x -axis in the xy -plane normal to the cylinder axis, using a spatial filter defined by:

$$f(\theta) = \begin{cases} \cos^2 4(\theta - \theta_{0m}), & |\theta - \theta_{0m}| \leq \pi/8 \\ 0 & |\theta - \theta_{0m}| > \pi/8 \end{cases} \quad (3.5)$$

In these analyses, the unit vector \mathbf{a} (the normal to the plane of isotropy, or fiber axis, which determines the polarization directions, \mathbf{m}_s and \mathbf{m}_f , and the angle, θ) was estimated from the average of the major axes of the fitted ellipses for each sample. For comparison, the dominant fiber orientation was also estimated from the average maximum principal diffusion eigenvector, measured by DTI, of each voxel in the relevant slices. Figs. 3.5 (b, c) and 3.6 (c, d) show examples of directionally filtered waves in cylindrical and cube samples, respectively. From directionally filtered wave fields, peaks and valleys were selected manually to capture the wavelength. The wavelength in each of the 16 directions was averaged over 5 representative slices. Values of average wave speed as a function of angle, θ , were fitted to Eq. 3.2 using a weighted, least-squares fitting algorithm to estimate the slow wave-speed parameters, μ and ϕ .

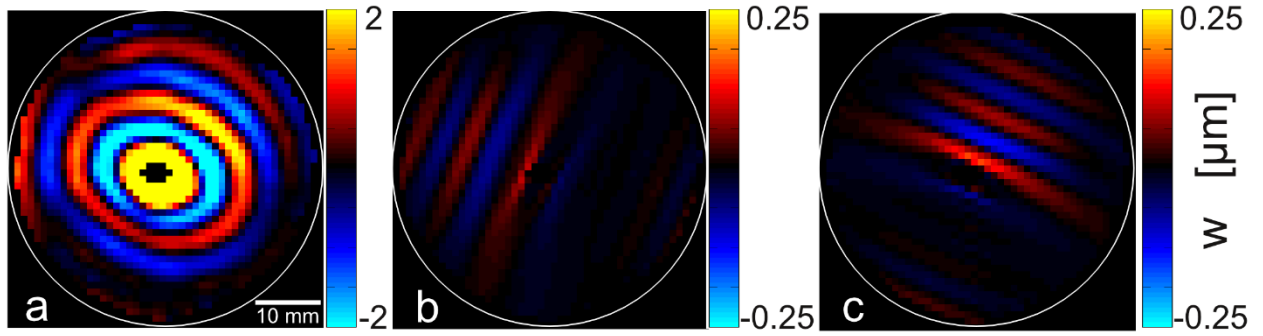


Figure 3.5: Wave propagation in a cylindrically aligned fibrin gel (200 Hz actuation) specimen, illustrating analysis by directional filtering. (a) Elliptical waves exhibiting direction dependent propagation with different wave speeds in different directions. (b-c) Displacement field after directional filtering in each of two propagation directions specified by angle, θ , from the dominant fiber direction. (b) $\theta = 0^\circ$ and (c) $\theta = 90^\circ$.

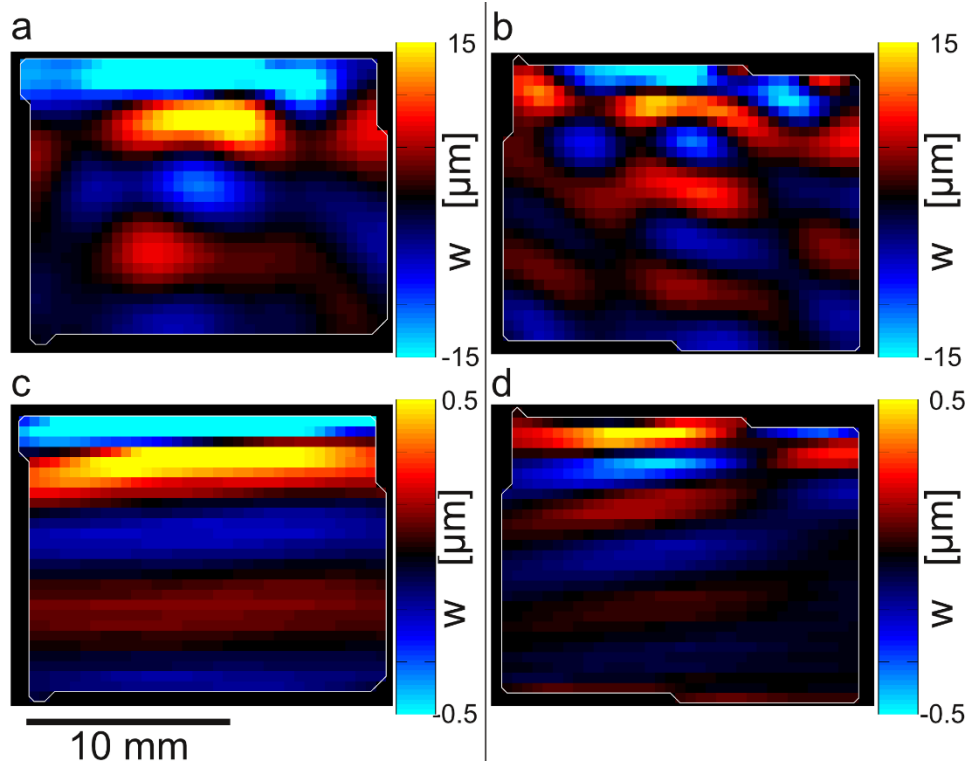


Figure 3.6: Wave propagation in a cube specimen of aligned fibrin with dominant fiber direction at 45° from horizontal (Figures 3.1(b,c)), illustrating analysis by directional filtering. (a) Excitation (600 Hz) in the m_f direction (with a component along the fibers, as in Figure 3.1(b)) leads to predominantly downward-propagating fast shear waves. (b) Excitation (600 Hz) in the m_s direction, perpendicular to the fibers, as in Figure 3.1(c), leads to predominantly downward-propagating slow shear waves. Panels (c,d): Directionally filtered waves in the $[0 \ -1 \ 0]$ direction corresponding to panels (a,b) respectively.

To characterize dissipative (viscous) effects, attenuation per wavelength was found from the ratios of amplitudes of successive peaks in directionally filtered waves in both experimental displacement data and in simulated displacement fields (Tweten et al, 2015). The method is illustrated in Figure 3.7. To avoid boundary effects, ratios were estimated only for cases in which multiple wavelengths were present, for peaks that were at least a half wavelength from the boundary (this restriction limited attenuation measurements to slow shear waves). The loss factor $\eta = \mu''/\mu'$ was estimated from the attenuation ratio using standard formulae (Auld, 1990). The attenuation ratio, r , is related to the loss factor, η by the following equations (Auld, 1990):

$$\eta = \frac{2\gamma}{1-\gamma^2}, \quad \gamma = \frac{-\ln(r)}{2\pi}. \quad (3.6a-b)$$

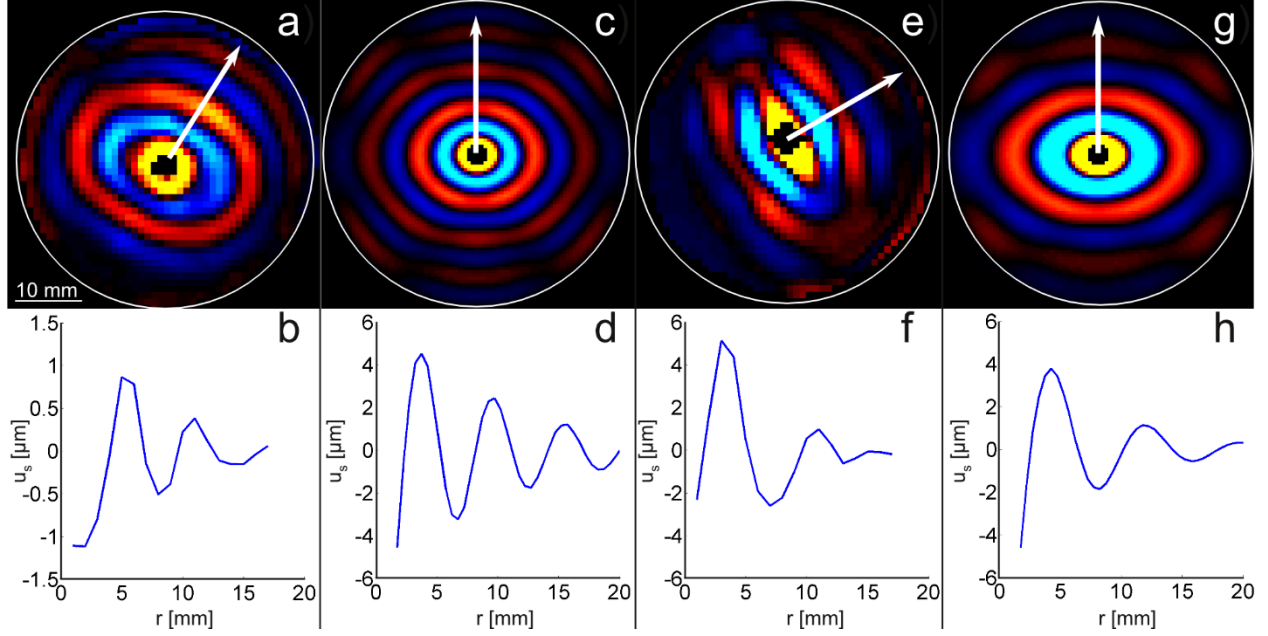


Figure 3.7: Shear wave attenuation. (a) Wave propagation (200 Hz) in a cylindrical specimen of aligned fibrin gel. (b) Directionally filtered slow-wave (u_s , $\theta = 90^\circ$) displacement in the fibrin specimen shown in (a), as a function of radial position. Markers show successive peaks used for attenuation ratio. (c) Wave propagation in a finite element (COMSOL) simulation of an ITI material excited at 200 Hz with estimated parameters for fibrin gel, including a loss factor of $\eta = 0.2$. (d) Directionally filtered slow-wave (u_s , $\theta = 90^\circ$) displacement in the simulation described in (c). (e) Wave propagation (800 Hz) in a cylindrical specimen of turkey breast. (f) Directionally filtered slow-wave (u_s , $\theta = 90^\circ$) displacement in the turkey breast specimen shown in (e). (g) Wave propagation in a finite simulation of an ITI material excited at 800 Hz, with estimated parameters for turkey breast, including a loss factor of $\eta = 0.4$. (h) Directionally filtered slow-wave (u_s , $\theta = 90^\circ$) displacement in the simulation described in (g).

3.4 Results

3.4.1 Imaging experiments

Wave patterns consistent with a transversely isotropic (TI) material model were observed in both cylindrical and cube samples. Axially-excited cylindrical samples (actuation in the \mathbf{m}_s direction) exhibited the slow shear-wave patterns predicted by mathematical models (Tweten et al., 2015). Elliptical waves were observed in specimens with a dominant fiber orientation (Fig. 3.4 (a, b, c)), and circular waves were observed in isotropic gel (Fig. 3.4 (d)), in planes perpendicular to the cylinder axis (Fig. 3.2 (a)). For ellipses fitted to radially-propagating wavefronts in axially excited cylindrical specimens, the ratio of major semi-axes and minor semi-axes was used to

describe shear anisotropy. The average ratio of semi-axes was found to be 1.65 ± 0.24 for turkey breast (800 Hz, n=4), 1.37 ± 0.14 for aligned fibrin (200 Hz, n = 3), and 1.03 ± 0.01 for isotropic gelatin (200 Hz, n = 3).

Analysis of the directionally-filtered wave speeds in cylindrical specimens (Fig 3.8 and Fig. 3.10(a, c)) revealed dependence of slow shear-wave speed, c_s , on the angle between fiber orientation and propagation direction, θ (Fig. 3.5). The observed dependence is consistent with theoretical predictions based on Eq. 2 (red curves in Fig 3.8) with fitted parameters. The parameters estimated for turkey breast were found to be $\mu = 33.1 \pm 11.4$ kPa and $\phi = 1.3 \pm 0.7$ for turkey breast (800 Hz, n = 4). For aligned fibrin gel, $\mu = 1.1 \pm 0.5$ kPa and $\phi = 1.1 \pm 0.2$ (200 Hz, n = 3). Close agreement between average fiber direction estimated from DTI (turkey breast) or magnetically induced alignment direction (fibrin) and the direction of fastest shear-wave propagation confirms that aligned fibers produce mechanical anisotropy.

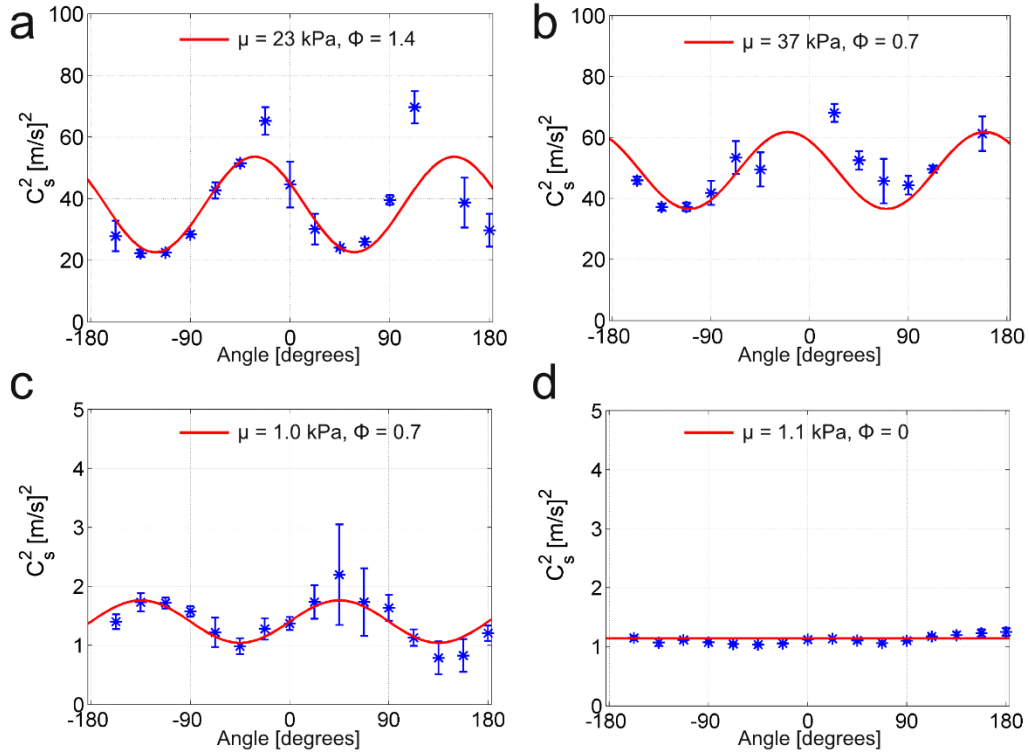


Figure 3.8: Average (\pm std. deviation) slow shear-wave speeds (blue *) plotted vs the angle between propagation direction and the horizontal axis of the cylinder, in cylindrical specimens. (a) Representative sample #1 of turkey breast (800 Hz). (b) Representative sample #2 of turkey breast (800 Hz). (c) Aligned fibrin gel (200 Hz). (d) Gelatin (200 Hz). Each plot is for a single sample; average values for each direction are computed over 5 slices. Theoretical curves (red lines) are obtained from Eq. 3.2 using values of μ and ϕ estimated by weighted, least-squares fitting for each sample.

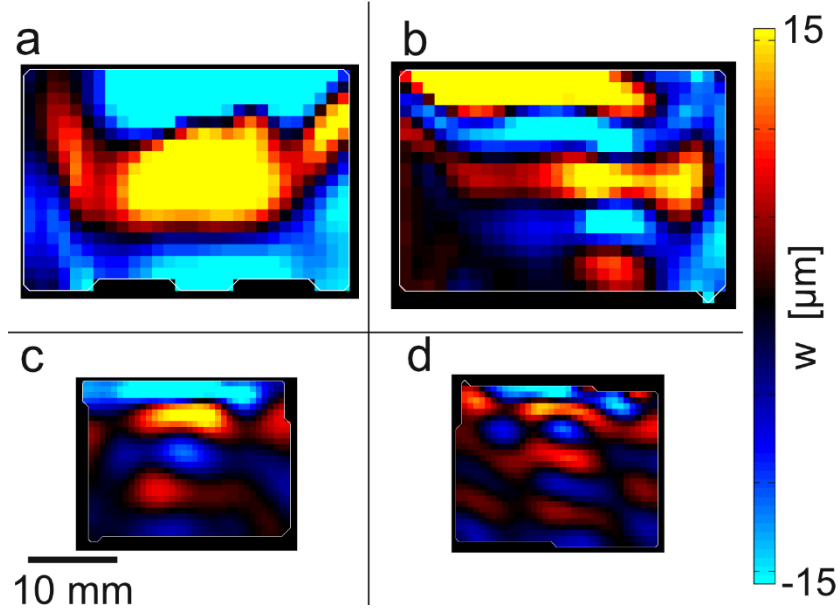


Figure 3.9: Wave propagation visualized by MRE in cube samples with different directions of excitation relative to fiber orientation. Fibers are oriented approximately 45° from horizontal as in Figure 2(b,c). Top panels (a,b) show fast and slow wave propagation in turkey breast actuated at 800 Hz and bottom panels (c,d) show aligned fibrin actuated at 600 Hz. Left panels (a,c): Actuation in the m_f direction with a component along the fibers (as in Figure 3.2(b)) leads to downward-propagating, fast shear waves. Right panels (b,d): Actuation in the m_s direction, perpendicular to the fibers (as in Figure 3.2(c)) leads to downward-propagating, slow shear waves.

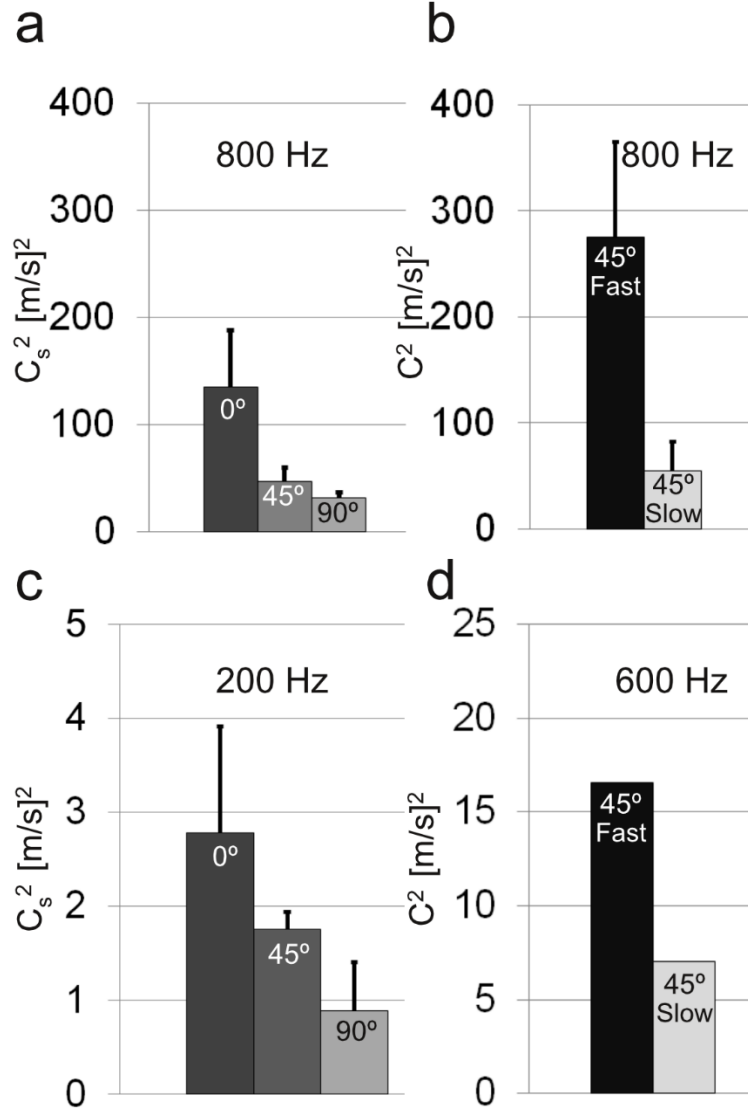


Figure 3.10: Summary of shear-wave speeds in turkey breast (a, b) and aligned fibrin (c, d) at different angles θ of propagation direction relative to fiber direction. (a) Slow shear-wave speed in cylindrical turkey breast specimens (800 Hz, N = 4 samples). Estimated material parameters: $\mu = 33.1 \pm 11.4$ kPa, $\phi = 1.3 \pm 0.7$ (b) Fast and slow shear-wave speeds in cube specimens (800 Hz, N=5). Estimated parameters: $\mu = 33.2 \pm 16.7$, $\zeta = 9.2 \pm 4.9$. (c) Slow shear-wave speeds in a cylindrical fibrin specimen (200 Hz, N=3). Estimated material parameters: $\mu = 1.1 \pm 0.5$ kPa, $\phi = 1.1 \pm 0.2$ (d) Average fast and slow shear-wave speeds in a cube specimen of aligned fibrin (600 Hz, N=1). Estimated parameters: $\mu = 4.7$ kPa, $\zeta = 2.7$.

In cube specimens, strong evidence for the importance of both slow and fast shear waves is provided by the dependence of propagation speed on polarization direction. Polarization

direction was controlled by actuation direction. When the actuation direction was in the plane containing the fibers and at an angle of $\sim 45^\circ$ from the fiber axis in this plane, displacements were induced in the \mathbf{m}_f direction. In this case, a substantial component of stretch is in the direction parallel to the fibers, the cubes exhibited primarily fast shear waves (Figs. 3.6(a) and 3.9(a,c)). In contrast, when the polarization direction was perpendicular to the fibers, in the \mathbf{m}_s direction, the cube exhibited slow shear waves (Figs. 3.6(b) and 3.9(b,d)). The difference between fast and slow shear wave speed in this sample is largely due to tensile anisotropy, characterized by the parameter ζ . This parameter was estimated from the ratio between slow and fast shear-wave speeds (Fig 3.10(b,d)), using Eqs. 3.2 and 3.4. Because Eqs. 3.2 and 3.4 contain three unknown parameters (after measuring the slow and fast wave speed and $\theta=45^\circ$), the average value of ϕ estimated from cylindrical specimens was used to solve for both μ and ζ . For turkey breast cubes, the estimated parameters are $\mu = 32.2 \pm 16.8$ kPa and $\zeta = 9.2 \pm 4.9$ (800 Hz, $n = 5$) and for aligned fibrin gel the estimated parameters are $\mu = 4.5$ kPa and $\zeta = 2.7$ (200 Hz, $n = 1$).

The attenuation per wavelength (ratio between successive peaks) for slow shear waves in turkey breast was $r = 0.27 \pm 0.18$, corresponding to a loss factor of $\eta = \mu''/\mu' = 0.43 \pm 0.17$ (Auld, 1990). In fibrin the attenuation per wavelength was $r = 0.50 \pm 0.21$ ($\eta = 0.22 \pm 0.11$) and in gelatin the attenuation ratio was $r = 0.67 \pm 0.13$ ($\eta = 0.13 \pm 0.06$). No statistically significant differences in attenuation per wavelength were found for different directions of propagation in MRE.

Parameter estimates are summarized in Table 3.1.

	Turkey breast		Aligned fibrin gel	
	Cylinder (800 Hz, N=4)	Cube (800 Hz, N=5)	Cylinder (200 Hz, N=3)	Cube (600 Hz, N=1)
μ kPa	33.1 ± 11.4	32.2 ± 16.8	1.1 ± 0.5	4.7
ϕ	1.3 ± 0.7	NA*	1.1 ± 0.2	NA*
ζ	NA	9.2 ± 4.9	NA	2.7
η	0.43 ± 0.17		0.22 ± 0.11	

Table 3.1: Summary of incompressible, transversely isotropic (ITI) material parameter estimates from MRE of turkey breast muscle tissue and aligned fibrin gel. Parameters are: baseline shear modulus, μ ; shear anisotropy, ϕ ; tensile anisotropy, ζ ; loss factor, η .(* To estimate ζ in cube specimens, ϕ was set to the value measured in cylindrical specimens.)

The amplitudes of slow and fast shear waves turkey breast and fibrin are summarized in Table 3.2.

	Turkey breast		Aligned fibrin gel	
	Cylinder (800 Hz, N=4)	Cube (800 Hz, N=5)	Cylinder (200 Hz, N=3)	Cube (600 Hz, N=1)
u_s (μm)	6.3 ± 1.2	4.9 ± 2.4	4.9 ± 0.7	2.2
u_f (μm)	NA	3.7 ± 2.7	NA	3.4

Table 3.2: Average amplitudes of displacements in slow (u_s) and fast (u_f) shear waves observed in cylindrical and cube specimens.

3.4.2 Direct mechanical characterization

Parallel and perpendicular shear moduli for turkey breast ($N = 33$) were averaged over the frequencies from 30-40 Hz using DST. The storage modulus was found to be $\mu'_{\parallel} = 4.8 \pm 1.6$ kPa when fibers were aligned parallel to the direction of imposed shear displacement and $\mu'_{\perp} = 3.2 \pm 1.1$ kPa when fibers were aligned perpendicular to the shear displacement. The loss modulus was $\mu''_{\parallel} = 2.2 \pm 0.7$ kPa for the parallel orientation and $\mu''_{\perp} = 1.1 \pm 0.3$ kPa for the perpendicular orientation. The ratio between parallel and perpendicular moduli $\mu'_{\parallel}/\mu'_{\perp} = 1.5 \pm 0.3$ for storage

modulus, $\mu''_{\parallel}/\mu''_{\perp} = 2.0 \pm 0.3$ for loss modulus, and $\mu_{\parallel}/\mu_{\perp} = 1.6 \pm 0.3$ ($\phi = 0.6 \pm 0.3$) for the magnitude. Fig. 3.11 summarizes these data.

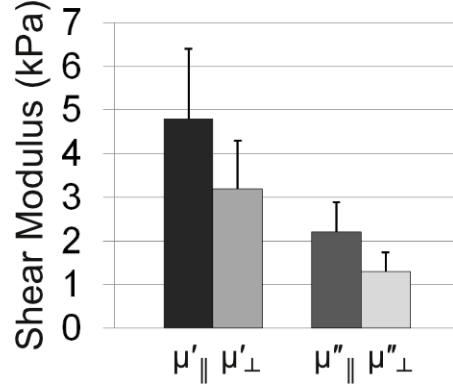


Figure 3.11: Storage (elastic) and loss (viscous) components of the complex shear modulus $\mu^* = \mu' + i\mu''$ of turkey breast (N=33, 30-40 Hz) measured by direct mechanical testing (DST). The ratio of the storage moduli was $\mu'_{\parallel}/\mu'_{\perp} = 1.5 \pm 0.3$, the ratio of the loss moduli was $\mu''_{\parallel}/\mu''_{\perp} = 2.0 \pm 0.3$, and the ratio of the magnitudes was $\mu_{\parallel}/\mu_{\perp} = 1.6 \pm 0.3$ ($\phi = 0.6 \pm 0.3$).

3.5 Discussion

In this experimental study, shear waves were imaged using MR elastography procedures in both muscle tissue *ex vivo* (turkey breast) and aligned fibrin gel. In axially-excited cylindrical samples, slow shear waves were found to propagate with elliptical wave fronts through both transversely isotropic materials, and with circular wave fronts in an isotropic medium (gelatin). In cube samples excited by tangential vibration on one face, measurements of slow and fast shear waves with differing polarization direction showed the effects of tensile anisotropy on wave speed. These results confirm that MRE can detect anisotropic shear moduli and tensile moduli in these two prototypical soft, fibrous, materials.

Direct mechanical tests (DST) in the current study confirmed mechanical anisotropy in turkey breast. Values of the shear anisotropy ratio from DST (turkey breast $\phi \sim 0.6$, or $\mu_{\parallel}/\mu_{\perp} \sim 1.6$ at 30-40 Hz) were comparable to values estimated from MRE ($\phi \sim 1.3$, or $\mu_{\parallel}/\mu_{\perp} \sim 2.3$, at 800 Hz). While both tests give ratios of shear modulus near 2, the fact that MRE estimates of anisotropy at 800 Hz are about 40% higher than DST at 30-40 Hz must be acknowledged. This difference may reflect limitations of each method. Accuracy and precision of MRE estimates are limited by the practical challenges of wavelength estimation from discretely sampled data with limited resolution. Results from DST may be affected by slip, nonlinearity or non-affine deformation. Alternatively, shear anisotropy may truly depend on frequency; the frequency ranges of the instruments in this study precluded a direct test of this possibility, but it is a topic for future investigation. Although DST of turkey breast was done at much lower frequencies (30-40 Hz) than in MRE (800 Hz), the values of the baseline storage modulus ($\mu \sim 4$ kPa at 30 Hz and $\mu \sim 33$ kPa at 800 Hz) are consistent with the expected increase in modulus with frequency in viscoelastic muscle tissue. Both DST and MRE estimates of μ are consistent with a previous MRE study of the viscoelastic properties of bovine muscle *ex vivo*, in which estimates of (isotropic) shear modulus increase from $\mu \sim 12$ kPa at 200 Hz to $\mu \sim 35$ kPa at 800 Hz (Riek et al., 2011).

In a previous study of aligned fibrin (Namani et al., 2012a), DST also detected anisotropy in shear ($\phi \sim 0.9$, at 20-40 Hz). This result is similar to estimates of shear anisotropy of aligned fibrin from MRE in the current study ($\phi \sim 0.6$ from measured wavelengths at 200 Hz). Also, the tensile anisotropy parameter for aligned fibrin estimated from MRE ($\zeta \sim 2.1$ at 600 Hz) in this

study is comparable to the tensile anisotropy estimated from asymmetric indentation of aligned fibrin ($\zeta \sim 3.5$, quasi-static) in previous work (Namani et al., 2012a).

The current results demonstrate the ability to both (1) characterize two distinct shear-wave types in soft transversely isotropic materials using MRE, and (2) use these shear wave measurements to estimate three elastic parameters. Notably, tensile anisotropy can cause large differences between slow and fast shear-wave speeds. Both fast and slow shear waves exhibit direction-dependent propagation speed. For slow shear waves, only shear anisotropy causes this directional dependence; tensile anisotropy plays no role in slow shear wave speed. In contrast, the directional dependence of fast shear wave speed is due to both shear anisotropy and tensile anisotropy. The estimation of mechanical parameters by directional filtering and isolation of separate shear-wave components is robust to noise (Tweten et al., 2015), since it does not rely on multiple numerical derivatives.

Romano et al. (2012, 2014) also used directional filters to isolate shear wave components. These authors analyzed wave speeds for a set of propagation and polarization directions aligned with a specific fiber tract, and estimated five to nine components of the elasticity tensor. For nearly-incompressible materials, elements of the elasticity tensor will have widely varying magnitude, as some elements approach infinity due to the contribution of the bulk modulus (see Appendix A). In the current approach, only three parameters (μ , ϕ , and ζ) are sought, which for incompressible materials, completely specify the compliance tensor. An advantage of the current

approach is that components of the compliance tensor converge to finite values as the bulk modulus approaches infinity.

The current material model is constrained by the assumptions of linear elasticity and incompressibility. Neither dissipation (viscosity, or complex shear modulus) nor nonlinearity is addressed comprehensively. The deformations in the current study are small ($<1\%$ strain) and thus linear theory is applicable. Though the focus of the current study is on elastic anisotropy, viscoelastic effects are clearly important for describing the complete response of tissue (Clayton et al., 2011b; Green et al., 2008; Qin et al., 2013). Dissipative effects are often attributed to fluid viscosity and approximated as isotropic, in which case the directional dependence of shear wave speeds can be attributed to anisotropy of elastic moduli. While this model was not rigorously tested in these materials, our observations of wave attenuation in MRE are consistent with an approximately isotropic loss factor (Fig. 3.7). Current estimates of loss factor from attenuation of waves in MRE in turkey breast ($\eta = 0.43$) are similar to those observed in prior studies of muscle ($\eta \approx 0.4$, Riek et al., 2011), as well as to the ratios of loss and storage moduli estimated by DST (Figure 3.10). Current estimates from MRE in fibrin ($\eta = 0.22$) approximate those from a prior study of fibrin ($\eta \approx 0.2$; Namani et al., 2012). The estimated loss factor in gelatin ($\eta = 0.13$) also agrees with prior observations ($\eta \approx 0.1$; Okamoto et al., 2011). The elastic constants estimated here may be interpreted as effective moduli at the given experimental frequency. In future work, complex moduli could be determined as functions of frequency.

The current study focused on the physics of wave propagation in ITI materials, and hence simple, manual methods were used to estimate wavelength and wave speed. This approach was chosen to separate the characterization of physical phenomena from the performance of automated algorithms. Future studies and related work (Tweten et al., 2015) will address the development of robust, automated methods for estimating wavelengths of slow and fast shear waves in TI materials.

Samples of roughly uniform material were used in this study. The current approach, in which the wavelength is estimated and averaged over five slices and then the average substituted into the equations to estimate the shear moduli, is adequate for globally homogenous materials, such as *ex vivo* specimens and phantoms. In actual tissue measurements *in vivo*, tissue homogeneity may only be assumed very locally. More work is needed to address parameter estimation in heterogeneous materials such as brain tissue *in vivo*. In such materials, it is critically important that both slow and fast shear waves propagating in multiple directions are present in a given volume, in order to obtain valid estimates of transversely anisotropic material properties in that region.

3.6 Conclusion

Both slow and fast shear waves propagate in soft, fibrous, materials and can be imaged by MRE. Shear-wave speed depends on the angles between propagation direction, polarization direction, and fiber direction. Three elastic parameters may be estimated from these data, allowing for concise characterization of nearly-incompressible, transversely isotropic materials. Such material

characterization can lead to improved modeling of white matter in the brain and a greater understanding of TBI.

Chapter 4: Measurement of anisotropic mechanical properties in porcine brain white matter *ex vivo* using magnetic resonance elastography

4.1 Overview

In this chapter, methods established in Chapter 3 to characterize anisotropic shear moduli were applied to white matter brain tissue *ex vivo*. These results have particular value for use in finite element modeling of brain biomechanics and traumatic brain injury (TBI). The current finding of anisotropy in white matter (WM) brain tissue adds to existing work on this topic in the literature, however, this study employs a unique implementation based on magnetic resonance elastography (MRE). “Slow” (pure transverse) shear waves are propagated at 100 Hz, 200 Hz and 300 Hz through sections of *ex vivo* porcine brain tissue including both WM and grey matter. Shear waves were found to propagate with elliptical fronts, consistent with TI material behavior. Regions of interest (ROI) were created to find local shear wavelengths parallel and perpendicular to the fiber orientation. Finite element (FE) simulations of a TI material with a range of plausible shear modulus (μ_2) and shear anisotropy parameters (ϕ) were performed and the results were analyzed in the same fashion as the experimental case. Parameters of the FE simulations which most closely matched each experiment were taken to represent the mechanical properties of that particular sample. Using this approach, WM in the *ex vivo* porcine brain was found to be mildly anisotropic in shear with estimates of minimum shear modulus (actuation frequencies listed in parenthesis):

$\mu_2 = 1.04 \pm 0.12$ kPa (at 100 Hz), $\mu_2 = 1.94 \pm 0.29$ kPa (at 200 Hz), and $\mu_2 = 2.88 \pm 0.34$ kPa (at 300 Hz) and corresponding shear anisotropy factors of $\phi = 0.27 \pm 0.09$ (at 100 Hz), $\phi = 0.29 \pm 0.14$ (at 200 Hz) and $\phi = 0.34 \pm 0.13$ (at 300 Hz). Future MRE studies will focus on tensile anisotropy, which will require both slow and fast shear waves for accurate estimation.

The material presented in this chapter is published in the Journal of the Mechanical Behavior of Biomedical Materials (Schmidt et al., 2018).

4.2 Introduction

Traumatic brain injury (TBI) is prevalent in the United States (Coronado et al., 2011) and worldwide. During TBI, impacts to the head lead to large skull accelerations, and brain tissue is deformed in tension and shear (Bayly et al., 2005; Margulies and Thibault, 1992). Accurate models are needed to fully understand the mechanism of tissue damage from impacts. Finite element (FE) models are often proposed as a method to predict injurious conditions (Ueno et al., 1995; Zhang et al., 2004). These methods require accurate knowledge of brain tissue properties in shear and tension, including their directional properties.

The response of brain tissue in shear was observed to be anisotropic under both small (Feng et al., 2013b) and large deformations (Feng et al., 2017); these authors applied a transversely isotropic model to interpret their data. Velardi et al. (2006) studied the experimental behavior of *ex vivo* porcine brain tissue in extension and proposed an anisotropic, hyperelastic constitutive model to explain their data. Prange and Margulies (2002) studied *ex vivo* porcine and human brain tissue and found a directional dependence in WM. Ning et al. (2006) characterized

brainstem experimental data as a transversely isotropic, viscoelastic material and compared observed behavior to the predictions of a corresponding numerical model.

MRE allows the estimation of mechanical properties in soft tissue from images of shear waves (Muthupillai et al., 1995a). MRE was originally developed using isotropic, elastic material models, which have evolved to include viscoelastic effects. Such isotropic models, either elastic or viscoelastic, have been applied in MRE studies involving liver (Asbach et al., 2008; Klatt et al., 2010a; Mariappan et al., 2009), breast (Sinkus et al., 2007) and brain (Atay et al., 2008; Clayton et al., 2011b; Green et al., 2008; Johnson et al., 2013). While most MRE studies assume “local homogeneity” of material properties, tissue heterogeneity has also been explored by Van Houten et al. (2001), using an inversion technique known as non-linear inversion.

The possibility of mechanical anisotropy in biological tissues should also be addressed by MRE. A transversely isotropic (TI) model is the simplest anisotropic model, with a single fiber orientation defining a plane of isotropy. Five parameters are required to completely define a general elastic TI material, while three parameters are sufficient to define an incompressible TI material. Recently, several MRE studies based on anisotropic material models have been performed. Most of this work has focused on estimation of two different shear moduli in planes parallel and perpendicular to the fiber orientation (2-parameter models). Sinkus et al. (2005) has published studies of shear anisotropy in breast tissue; Green et al. (2013), Wuerfel et al. (2010), Papazoglou et al. (2006), Qin et al. (2013) have studied muscle tissue. Shear anisotropy has also

been estimated in anisotropic biomaterials: Qin et al. (2013) studied anisotropic phantoms of a composite material and Namani et al. (2009) studied aligned fibrin gels.

More complete transversely isotropic models account for both shear and tensile anisotropy.

Romano et al. (2012) estimated five stiffness parameters in brain white matter corticospinal tracts utilizing spatial-spectral filters, Helmholtz decomposition, and waveguides. Three-parameter models have recently emerged as more compact, but still accurate, models of soft tissue, which is nearly incompressible. Guo et al. (2015) estimated three parameters in skeletal muscle using inversions of the curl of the displacement field. Tweten et al. (2017, 2015) used finite element (FE) simulations to establish basic requirements for estimation of three material parameters. Schmidt et al. (2016) measured both “slow” and “fast” shear waves in muscle tissue *ex vivo* and aligned fibrin gels, and used complementary information in these fields to estimate all three material parameters.

In the human brain, Romano et al. (2012) obtained estimates of five anisotropic stiffness parameters in corticospinal tracts in human subjects *in vivo*, but such estimates remain speculative since parameter values have not been confirmed by direct mechanical test or comparison to simulation. Qualitatively, however, anisotropy of WM has been detected by MRE *in vivo* in the human brain by Anderson et al. (2016), who used multiple excitation methods and showed that estimates of isotropic material parameters depended on the directional properties of the wave field. Still missing are clear estimates of a minimal set of intrinsic, anisotropic material

parameters for WM brain tissue, in which confidence has been established by comparison to direct test and simulations.

The goal of the current study is to quantify the anisotropic shear properties of *ex vivo* WM using MRE, by estimating parameters of simulations to fit experimental data. Shear waves were visualized and measured in *ex vivo* porcine WM embedded in gelatin (experiment) and in numerical (FE) simulations of shear waves in a TI material embedded in an isotropic material. Results from simulations were compared to experiment to estimate anisotropic shear moduli over multiple frequencies. By comparing experimental wave fields to numerical simulations that incorporate material anisotropy in a sub-domain of a finite-size sample, typical assumptions underlying estimates of material properties (i.e., an unbounded domain with uniform, isotropic properties) are not necessary. The results indicate mild, but non-negligible, mechanical anisotropy of WM brain tissue in shear.

4.3 Methods

4.3.1 Theory

In an incompressible TI, linear, elastic material model, valid for small deformations, the three independent material parameters can be defined by shear modulus, μ_2 , shear anisotropy, ($\phi = \mu_1/\mu_2 - 1$), and tensile anisotropy ($\zeta = E_1/E_2 - 1$), where μ_1 is the shear modulus that governs shear in planes containing the dominant fiber axis (the normal to the plane of isotropy, \mathbf{a}), μ_2 is the minimum shear modulus governing shear in the plane of isotropy (normal to the fiber axis), E_1 is the tensile modulus in the fiber direction and E_2 is the tensile modulus in directions perpendicular to fiber axis (Jones, 1998; Schmidt et al., 2016; Spencer, 1984; Tweten

et al., 2015). Two types of shear waves, dependent on these parameters, are possible in incompressible TI materials: (i) “slow” (pure transverse) waves, where the polarization of the shear wave, \mathbf{m}_s , is perpendicular to both the wave propagation direction, \mathbf{n} , and the fiber direction, \mathbf{a} ; and (ii) “fast” (quasi-transverse) waves, where the polarization of the shear wave, \mathbf{m}_f , is perpendicular to the polarization of the slow shear wave, and lies in the plane defined by \mathbf{n} and \mathbf{a} . Wave speeds of slow and fast shear waves can be defined, respectively, by the following expressions (Schmidt et al., 2016; Tweten et al., 2015):

$$c_s^2 = (\mu_2/\rho) (1 + \phi \cos^2 \theta), \quad (4.1)$$

$$c_f^2 = (\mu_2/\rho)(1 + \phi \cos^2 2\theta + \zeta \sin^2 2\theta). \quad (4.2)$$

In the simplest viscoelastic model of TI material behavior, dissipation can be modeled by an isotropic loss factor η , so that each real-valued, elastic modulus, for example μ_2 , is replaced by a complex-valued, viscoelastic modulus $\mu_2^* = \mu_2' + i\mu_2''$, where $\eta = \mu_2''/\mu_2'$.

4.3.1 Experiments

4.3.1.1 Sample preparation

Disk-shaped samples (~42mm diameter, ~14 mm thick), consisting of both WM and GM, were dissected from the corpus callosum and associated superior cortical GM in female domestic pigs (N=8, age 3 months, 40-45 kg) immediately after euthanasia (Fig.4.1, a-d). Samples were embedded in gelatin mixed with 50% water and 50% glycerol (Okamoto et al., 2011b) in a cylindrical container (48 mm inner diameter) The embedded samples were punctured axially by a 3-mm diameter plastic rod (Fig. 4.1,e). A piezoelectric actuator (APA150M, Cedrat Technologies, Meylan, France) powered by a low-current, high-voltage amplifier (LA75C, Cedrat Technologies, Meylan, France) was used to provide harmonic vibrations of the plastic rod

in the central axis (z) at 100, 200, and 300 Hz, generating radially-propagating shear waves ($\mathbf{n} \approx \mathbf{e}_R$). This preparation does not probe tensile anisotropy (no “fast” shear waves are produced). This is because shear wave propagation is normal to fiber orientation, producing no stretch along the fiber direction.

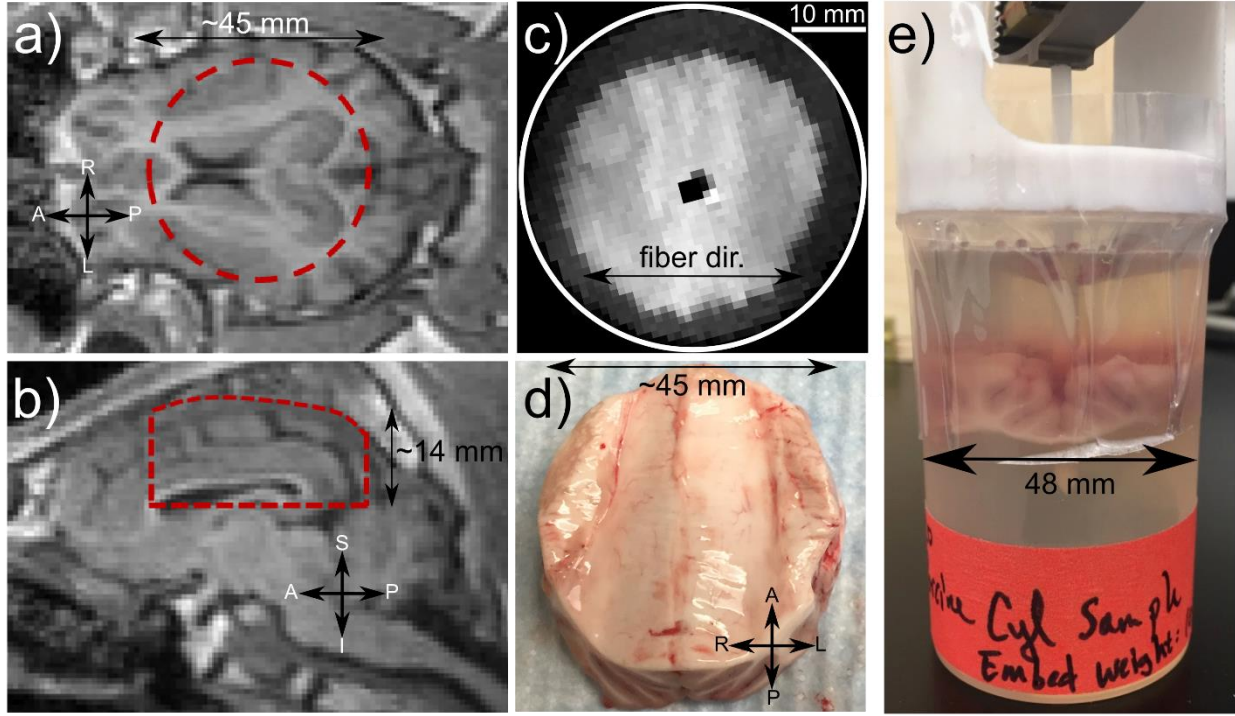


Figure 4.1: (a-b) T1-weighted (T1W) *in vivo* anatomical images from prior work (Bayly et al., unpublished) showing tissue volume used for current study (red dashed outlines). (c) T1W images of *ex vivo* sample used in the current study. Fiber orientation is left-to-right. (d) Photo of *ex vivo* sample of brain tissue used for this study. (e) Apparatus for MRE experiments: tissue embedded in gel inside cylindrical container, excited by harmonic motion of a central axial stinger.

4.3.1.2 Imaging

Images of shear-wave propagation in the disk-shaped WM/GM samples were acquired using previously-described spin-echo MRE sequences (Clayton et al., 2011; Schmidt et al., 2016).

Imaging was performed at 4.7 Tesla at room temperature ($\sim 21^\circ\text{C}$) with an Agilent/Varian

DirectDrive imaging system. MRE imaging parameters were: voxel size = 1.0 mm isotropic, TR

= 1100 - 1300 ms, TE = 30-47 ms. Multiple (1-3) sinusoidal motion encoding cycles of gradient strength 10-12 G/cm were synchronized with motion to induce phase contrast proportional to displacement. Eight temporal samples were acquired per sinusoidal excitation period, by incrementing the phase delay between the imposed vibration and acquisition. Anatomical (spin-echo, T1-weighted, TE = ~10ms, TR = 1000 ms, 2 averages) MRI was performed (Fig. 4.1, c) to identify the boundaries of the brain tissue sample and to distinguish white matter and gray matter. Diffusion weighted images (30 directions, $b=3000 \text{ s/mm}^2$) were acquired over the same volume to confirm the myelinated axon orientation. Time from euthanasia to the start of the experiments was ~1-2 h.

4.3.1.3 Computational modeling and simulations

A 3D, finite-element (FE) model of the MRE experiment was created using COMSOL™ Multiphysics 5.1. The model consists of a cylindrical slab (42 mm diameter, 14 mm thick) representing brain tissue embedded in a cylinder of gelatin (48 mm diameter, 48 mm long). The inclusion was assigned TI material properties with a single fiber direction and the gelatin was assigned isotropic properties (Fig. 4.2). Axial harmonic excitation of 25 μm was provided at 100, 200, and 300 Hz on the inner radius (1.5 μm) of the model. Assigned properties of the inclusion were: baseline storage modulus, μ_2 , varied from 0.5 – 1.5 kPa (at actuation frequency of 100 Hz), 1.2 – 2.5 kPa (at 200 Hz), 2 – 5 kPa (at 300 Hz), a loss factor, $\eta = 0.5$, typical of brain tissue (Feng et al., 2013b), density, $\rho = 1000 \text{ kg/m}^3$. Shear anisotropy, ϕ , was varied from 0 – 0.6. Tensile anisotropy (nonzero ζ) was not included as ζ does not affect pure transverse (“slow”) shear waves induced by excitation normal to fiber direction. The material properties assigned to gelatin were: shear storage modulus, $\mu = 1.0, 1.1, \text{ and } 1.2 \text{ kPa}$ (Okamoto et al., 2011b) at 100,

200, and 300 Hz actuation frequencies respectively; loss factor, $\eta = 0.1$; and density, $\rho = 1100 \text{ kg/m}^3$. Loss factors taken from prior studies were varied over a limited range to check that attenuation of wave amplitudes in simulations was similar to experiment. The parameters μ_2 and ϕ of the FE simulations with shear wave propagation most similar to the MRE experiment were taken as the estimates of μ_2 and ϕ within the selected slices of the *ex vivo* tissue sample.

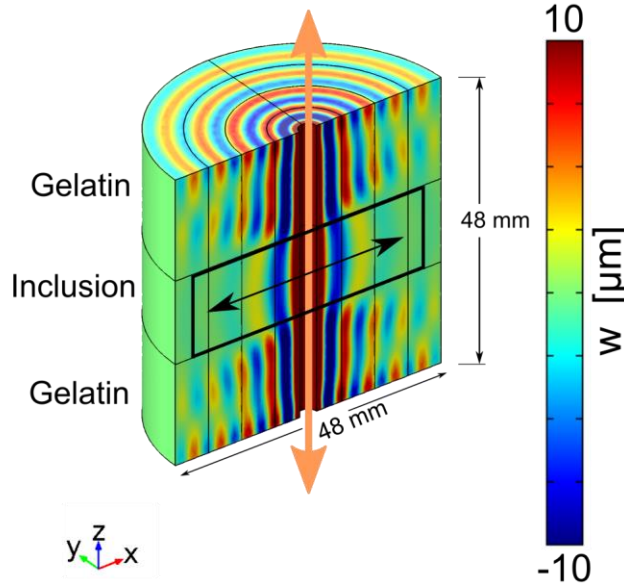


Figure 4.2: FE model (COMSOL™ Multiphysics v5.1) showing axial (w) displacement. A disk-shaped inclusion representing transversely isotropic (TI) WM is enclosed in an isotropic soft material representing gelatin. Inclusion: $\mu_2 = 2.0 \text{ kPa}$, $\mu_1 = 2.6 \text{ kPa}$ ($\phi=0.30$), $\eta = 0.5$, $\rho = 1000 \text{ kg/m}^3$. Surrounding gelatin: $\mu = 1.1 \text{ kPa}$, $\eta = 0.1$, $\rho = 1100 \text{ kg/m}^3$. Actuation frequency: 200 Hz. The black arrow points in the direction normal to the TI material's plane of isotropy (i.e., the fiber axis, a).

4.3.1.4 Analysis of experimental and simulated image data

The Fourier transform of the displacement data from all of the 8 acquisition phases was found using the FFT, and the coefficients at the fundamental harmonic were extracted, producing a three-dimensional field of Fourier coefficients. Data were then smoothed (Gaussian smoothing with a 3x3x3 voxel convolution kernel and a standard deviation of 1) in 3D. For estimation of apparent shear modulus and shear wavelength, the curl of the smoothed 3D displacement field was expected to eliminate effects of longitudinal waves.

As a simple measure of anisotropy, radially-propagating shear waves in WM were fitted to ellipses (see Fig. 4.3). Peaks of elliptical wave fronts were manually picked on a 2D image of axial (w) displacement in the xy plane (interpolated in the xy plane from 1 mm resolution to 0.5 mm resolution), in 3 contiguous slices within slices containing WM from each sample. The various FE simulations (across a plausible range of baseline shear moduli and shear anisotropy) were also subjected to the same analysis, except that peaks of elliptical wave fronts were picked from 3 contiguous, central slices by an automated 2D method. Points picked either manually or by automated method were fitted using an algorithm that minimized the squared-error between the ellipses and the picked points (Fitzgibbon et al., 1999). The ratio, R , between ellipse semi-axis lengths was recorded for each experimental sample or FE simulation, along with the angle of the longer semi-axis.

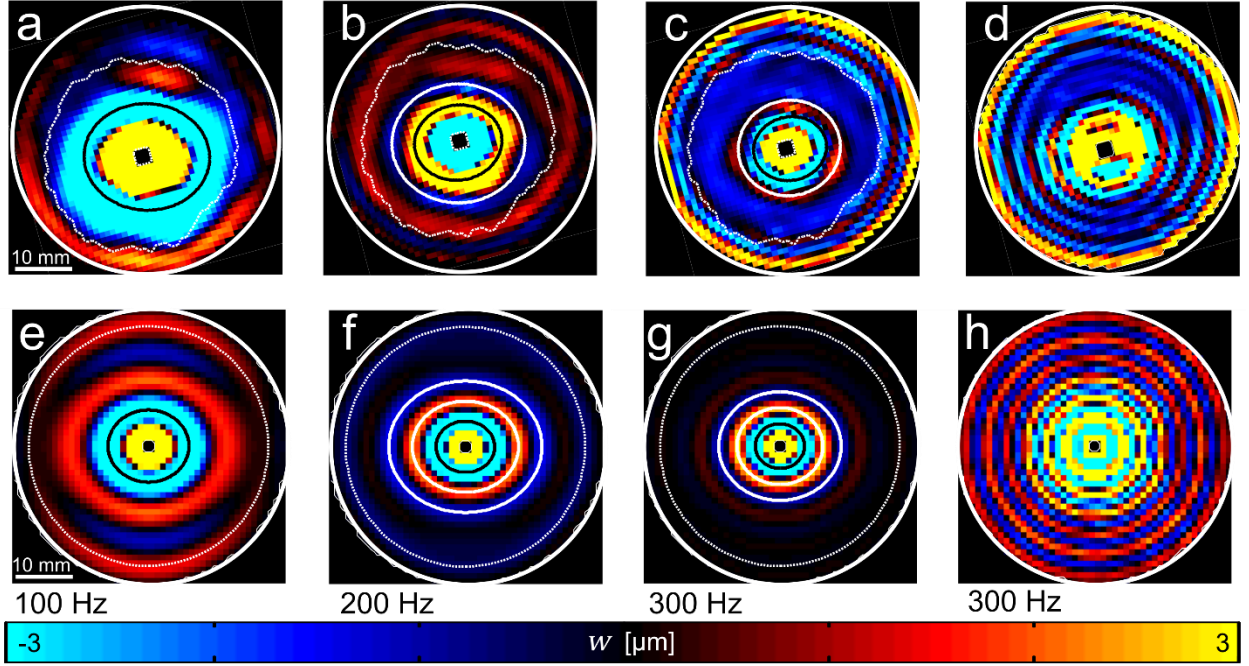


Figure 4.3: Shear-wave propagation in WM brain tissue (experiment, top row) and transversely isotropic FE models (simulation, bottom row) with fitted ellipses outlined. (a-c) MRE images of shear wave propagation in WM at (a) 100 Hz, (b) 200 Hz, and (c) 300 Hz. Shear-wave fronts are fitted by ellipses (black or white). The boundary of the tissue sample is outlined by a thin dotted white line. (d) Shear-wave propagation in a slice containing only gelatin at 300 Hz. (e-g) Shear wave propagation in FE simulations with similar mechanical properties to the experiment: (e) 100 Hz, $\mu_2 = 1100$ Pa, $\phi = 0.30$; (f) 200 Hz, $\mu_2 = 1600$ Pa, $\phi = 0.45$; (g) 300 Hz, $\mu_2 = 2300$ Pa, $\phi = 0.35$. (h) Shear-wave propagation in the isotropic/gelatin portion of the FE model at 300 Hz.

The apparent complex shear modulus $\mu^* = \mu' + i\mu''$ was estimated in both MRE experiments and FE simulations, using local direct inversion (LDI) of the three components of the curl of the displacement field (Okamoto et al., 2011b). To express these parameters in terms of kinematic features of the wave field, analogous to elliptical shape, storage modulus estimates were converted to local shear wavelength, defined as $\lambda^+ = \frac{1}{f} \sqrt{\frac{\mu'}{\rho}}$. To quantify directional variations in wavelength maps from LDI, regions of interest (ROIs, see Fig. 4.4) were defined by squares centered at equal distances from the cylinder axis, in directions parallel and perpendicular to the longer semi-axis.

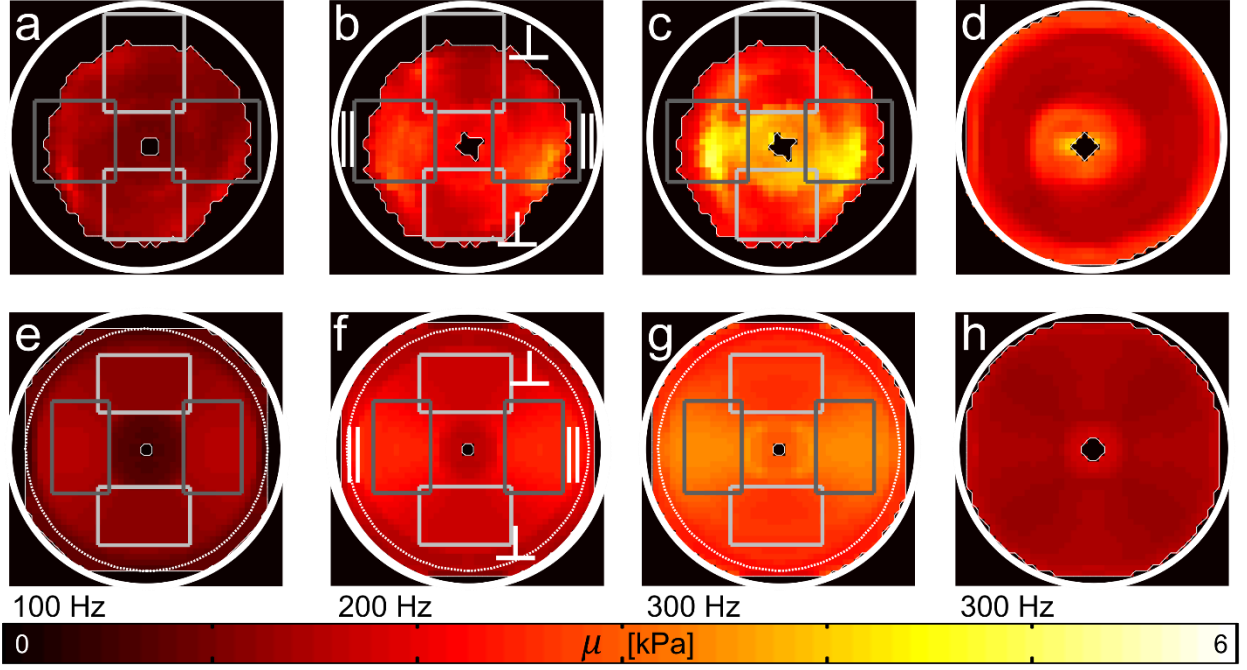


Figure 4.4: Apparent shear modulus in WM brain tissue and transversely isotropic (TI) FE models. Regions of interest (ROIs) parallel (||) and perpendicular (⊥) to fitted ellipse semi-major axis are highlighted. (a-c) Maps of apparent shear modulus at (a)100 Hz, (b) 200 Hz, (c) 300 Hz, estimated from MRE data in slices containing brain tissue. (d) Maps of apparent shear modulus at 300 Hz, estimated from MRE data in slices containing only gelatin. (e-g) Maps of apparent shear modulus estimated using data from FE simulations with mechanical properties matched to the experiment: (e) 100 Hz: $\mu_2 = 1100$ Pa, $\phi = 0.30$; (f) 200 Hz: $\mu_2 = 1600$ Pa, $\phi = 0.45$; (g) 300 Hz: $\mu_2 = 2300$ Pa, $\phi = 0.35$. (h) Maps of apparent shear modulus at 300 Hz, estimated using data from the isotropic/gelatin portion of the FE model.

4.3.1.5 Dynamic shear testing (DST)

For comparison with MRE, estimates of viscoelastic shear modulus (μ_1^* and μ_2^*) were also obtained by dynamic shear testing (DST) (Feng et al., 2013b; Namani et al., 2012b). Samples consisting of predominantly WM brain tissue ($N = 10$) acquired from the corpus callosum and samples consisting of predominantly GM brain tissue ($N=10$) acquired from the region superior to the corpus callosum within the frontal and parietal lobes of the brain were excised from 3 different female domestic pigs (age 3 months, 40-45 kg). The mean \pm std. deviation sample thickness was 2.75 ± 0.63 mm and the sample diameter was 13.39 ± 3.42 mm in WM samples, and in GM the average sample thickness was 3.37 ± 0.84 mm and a sample diameter of 14.93 ± 1.31 mm. Samples were tested in shear both parallel and perpendicular to the WM fiber axis

(determined visually), and in two arbitrary perpendicular directions in GM. Shear modulus estimates were averaged over the frequency range from 20 to 30 Hz. This range was chosen to avoid inertial effects (shear waves) within the sample (Feng et al., 2013b).

4.4 Results

4.4.1 MRE experiments and FE simulations exhibit elliptical shear wave propagation

MRE experiments were performed on cylindrical brain samples from eight pigs. Example shear wave images from a representative MRE experiment, and from the corresponding FE simulation found to best approximate this particular MRE experiment are shown in Fig. 4.3. Shear wave patterns are consistent with theoretical predictions based on wave speeds in a uniform, unbounded, TI material (Tweten et al., 2015). Elliptical waves were observed in regions with known white matter (corpus callosum). Circular waves were observed in slices containing only isotropic gelatin (Fig. 4.3,d).

4.4.2 Estimated local wavelength comparisons between experiment and FE models

Each MRE experiment was matched individually to the FE simulation with shear wave propagation that most resembled that of the experiment, in terms of both (1) local shear wavelength in parallel and perpendicular ROIs and (2) the ratio of elliptical semi-axis fit to shear wave fronts. Normalized root mean squared error (NRMSE) was found between local wavelength (λ^+) estimates in experiment and simulation, in both parallel ($NRMSE_{\lambda_1}$) and perpendicular ($NRMSE_{\lambda_2}$) ROIs, in the 8 image slices of the experimental sample that contained the most WM (closest to the center of the corpus callosum), and in the middle 8 slices of the TI inclusion of the FE models. Normalized RMS error ($NRMSE_R$) was also found between the

ellipse axis ratio (R) of the MRE experiment and FE simulations for the 3 slices in which ellipses were fitted. These three NRMSE estimates were combined to identify the FE simulation that most closely represented the specific experiment. The NRMSEs of each wavelength and the ellipse ratio were weighted and summed to provide an overall objective function that reflected both metrics (local wavelength and ellipse shape) equally. The following weighting scheme was used for this study:

$$NRMSE_{weighted} = \frac{1}{4}NRMSE_{\lambda_1} + \frac{1}{4}NRMSE_{\lambda_2} + \frac{1}{2}NRMSE_R. \quad (4.3)$$

Fig. 4.5 shows surfaces of NRMSE from the comparison between all FE simulations and a single representative MRE experiment. These surfaces show (i) the wavelength error between simulations and experiment in the perpendicular ROI ($NRMSE_{\lambda_2}$, Fig. 4.5, a), (ii) wavelength error in the parallel ROI ($NRMSE_{\lambda_1}$, Fig. 4.5, b), (iii) the error between ellipse axis ratios ($NRMSE_R$, Fig. 4.5, c), and (iv) a plot showing the weighed NRMSE combining all estimates into one weighted estimate. Parameter estimates for all samples (N=6 for 100 Hz, and N=8 for 200 and 300 Hz) were analyzed statistically and results are shown in Fig. 4.6.

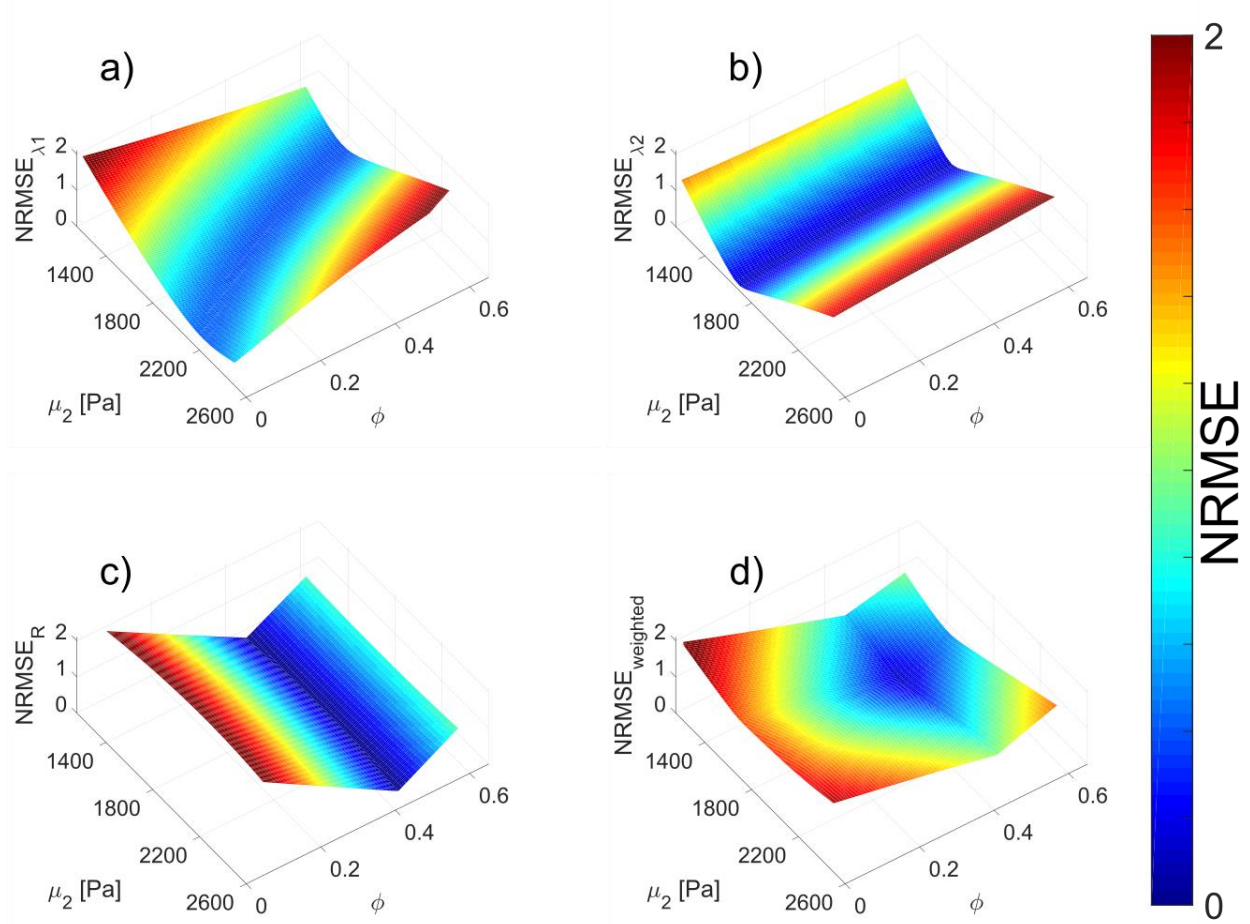


Figure 4.5: Parameter estimation by comparison of experiment to simulation. Results from inversion of data from MRE experiments are matched to results of inversion of data from a library of FE simulations performed with a range of plausible transversely isotropic (TI) material parameters. Results from \perp and \parallel ROIs are compared separately to identify effects of anisotropy. (a) Normalized RMS error (NRMSE) between wavelength (λ_2) estimates from experimental data and TI FE simulations in the \perp ROI. (b) NRMSE between wavelength (λ_1) estimates from experimental data and FE simulations in the \parallel ROI. (c) NRMSE between the ratio of semi-axes of ellipses fitted to shear-wave fronts in the experimental data and FE simulations. (d) Weighted total NRMSE between experiment and FE models (weighted sum of wavelength NRMSEs and axis ratio NRMSE).

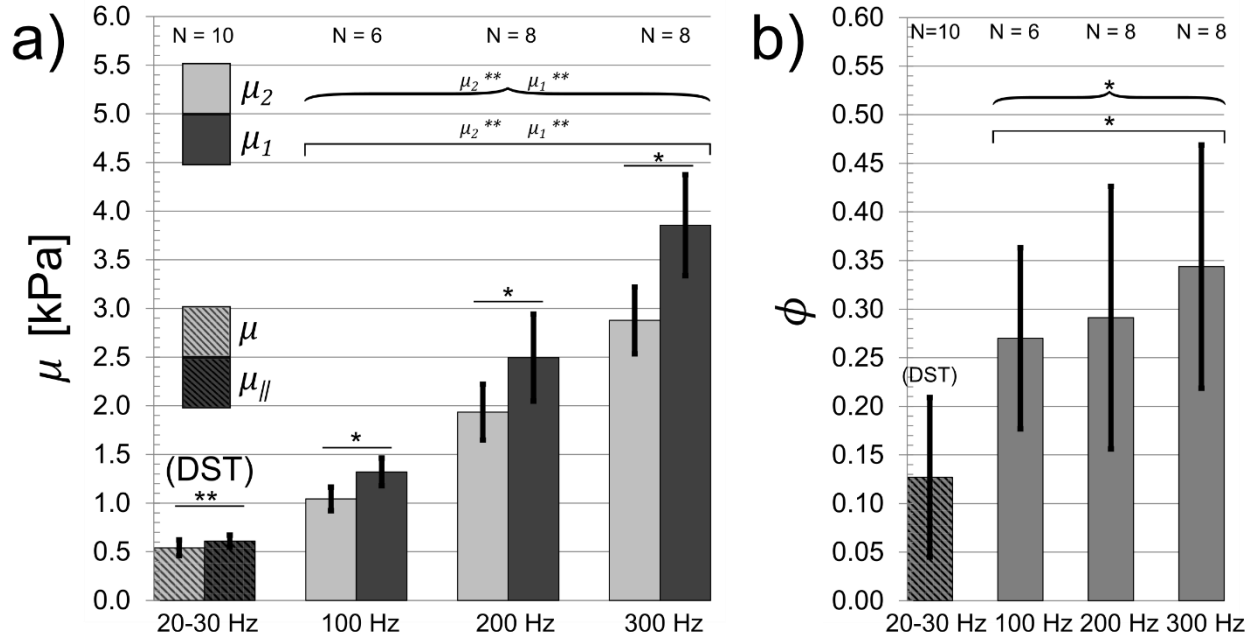


Figure 4.6: Summary of shear modulus and shear anisotropy estimates in WM brain tissue. (a) Shear moduli in planes parallel (μ_1) and perpendicular (μ_2) to fiber orientation. (b) Shear anisotropy ($\phi = \mu_1/\mu_2 - 1$). Solid bars (100 Hz, 200 Hz, 300 Hz) represent results from MRE/FE analysis. Cross-hatched bars (20-30 Hz) show results obtained by direct mechanical testing (DST). Lines across plots with stars indicate statistical significance (* $P < 0.05$, ** $P < 0.005$). Curly bracketed lines signify Friedman tests across 100 Hz, 200 Hz, and 300 Hz. Straight lines signify Wilcoxon signed rank tests between two sets of data.

WM in the *ex vivo* porcine brain was found to be anisotropic in shear with estimates of minimum shear modulus shown in Table 4.1. The shear modulus in planes parallel to fibers, μ_1 , was significantly larger than shear modulus in the plane of isotropy, μ_2 (Wilcoxon signed rank test) at 100, 200, and 300 Hz ($P < 0.05$, $P < 0.05$, $P < 0.05$, respectively). Both shear moduli showed significant increases with actuation frequency (μ_2 : $P < 0.005$; μ_1 : $P < 0.005$; Friedman test) as expected for viscoelastic materials. Notably the increase in the anisotropy factor ϕ was also statistically significant ($P < 0.05$).

4.4.3 Dynamic shear testing (DST) results

Shear moduli in planes parallel and perpendicular to the fiber axis for WM brain tissue (N=10) were estimated in a frequency range from 20 to 30 Hz using DST. This frequency range is as high as possible, while avoiding instrument resonances and inertial effects in the sample. The storage modulus was estimated to be $\mu'_{\parallel} = 0.61 \pm 0.06$ kPa when fibers were aligned parallel to the direction of imposed shear displacement and $\mu'_{\perp} = 0.54 \pm 0.08$ kPa when fibers were aligned perpendicular to shear displacement. The loss modulus was $\mu''_{\parallel} = 0.34 \pm 0.05$ kPa for the parallel orientation and $\mu''_{\perp} = 0.30 \pm 0.05$ kPa for the perpendicular orientation. The mean (\pm std. dev.) ratio between paired parallel and perpendicular moduli was $\mu'_{\parallel} / \mu'_{\perp} = 1.14 \pm 0.08$ for storage modulus, and $\mu''_{\parallel} / \mu''_{\perp} = 1.11 \pm 0.06$ for loss modulus. Shear moduli from two perpendicular arbitrary directions (denoted as a and b , since there is no reference fiber direction) in GM brain tissue (N=12) were averaged over frequencies from 20 to 30 Hz using DST. The storage modulus was found to be $\mu'_a = 0.49 \pm 0.09$ kPa in one direction of imposed shear displacement and $\mu'_b = 0.50 \pm 0.11$ kPa when the shear displacement was imposed in the perpendicular direction. The loss modulus was $\mu''_a = 0.20 \pm 0.05$ kPa for the first orientation and $\mu''_b = 0.23 \pm 0.06$ kPa for the second orientation. In GM, the ratio between moduli in these two arbitrary, perpendicular directions, was $\mu'_a / \mu'_b = 0.99 \pm 0.12$ for storage modulus and $\mu''_a / \mu''_b = 0.94 \pm 0.21$ for loss modulus. Wilcoxon signed rank test statistical analysis was performed to show WM μ_1 and μ_2 shear moduli to be significantly different than each other (storage modulus: $P < 0.005$, loss modulus: $P < 0.005$). Similar statistical analysis showed GM μ_a and μ_b shear moduli to be not significantly different (storage modulus: $P = 0.38$, loss modulus: $P = 0.084$).

Frequency [Hz]	μ_2 [kPa]	ϕ
100	1.04 ± 0.12	0.27 ± 0.09
200	1.94 ± 0.29	0.29 ± 0.14
300	2.88 ± 0.34	0.34 ± 0.13

Table 4.1: A summary of the findings in Chapter 4 using MRE. Baseline shear moduli (μ_2) and the shear moduli anisotropy factor (ϕ) for three experimental actuation frequencies (100, 200, and 300 Hz) are shown. The data are also expressed in Figure 4.6 (non cross-hatched bars).

4.5 Discussion and Conclusions

In this study, slow shear waves were imaged using MR elastography techniques in WM *ex vivo* brain tissue. In centrally-excited, cylindrical samples, outwardly propagating slow shear waves exhibited elliptical wave fronts and local wavelengths that depended on the direction of propagation, consistent with TI behavior (Schmidt et al., 2016). Baseline shear moduli and shear anisotropy of *ex vivo* porcine WM brain tissue were estimated by comparing experimental shear wave data to simulations of shear waves in TI materials.

MRE and direct mechanical tests (DST) in the current study both indicated the presence of mild shear anisotropy in porcine WM brain tissue. Shear modulus estimates obtained by fitting the current MRE results with FE simulations (shear modulus magnitudes 1.0 kPa at 100 Hz, 1.9 kPa at 200 Hz, and 2.9 kPa at 300 Hz) were larger than estimates obtained by DST (average shear modulus magnitude ~ 0.65 kPa). These trends are consistent with the expected increase in modulus with increase in actuation frequency in viscoelastic biological tissue. Shear anisotropy

factors (ϕ) of 0.25-0.35, estimated by fitting the current MRE studies with FE simulations, were roughly double those observed by DST in the current study, but closer to the shear anisotropy factors observed by DST (Feng et al., 2013b) in ovine corpus callosum WM. Differences may reveal limitations of each method, but we particularly note limitations of DST. DST estimates can be affected by sample flatness, normal force, order of testing (which direction is tested first), slip, nonlinearity, or non-affine deformation. MRE estimates of parameters are limited by the practical challenges of image resolution (discretization of shear waves) and domain size (which limits the number of wavelengths). Both methods potentially obscure local variations on a scale smaller than the wavelength of a shear wave (for our MRE experiments this was $\sim 5 - 10$ mm), or the size of the DST sample ($\sim 13-15$ mm). Shear anisotropy may also depend on frequency. Differences between shear anisotropy estimates from MRE and DST are similar to those found in previous studies involving muscle tissue (Schmidt et al., 2016). Given the limitations of each method, we believe that the shear anisotropy estimates from MRE, which are also consistent with simulation and visual observations of wavefronts, are more accurate. It should be noted that these results do not validate or prove the ability of this model to predict behavior in another situation, but illustrate the ability of this model, with these parameters, to explain the current observations.

While the focus of this study is on MRE estimation of material properties, we note that the current estimates of material properties from DST in the porcine brain between 20 - 30 Hz are comparable to those from previous DST studies on *ex vivo* ovine brain (Feng et al., 2013b). Shear storage modulus in planes parallel to the fiber orientation in WM were very similar between the two studies, while shear storage modulus perpendicular to the fiber axis is $\sim 20\%$

larger in the current study, leading to the lower shear anisotropy ratio observed by DST in the current study. Both studies found GM to be isotropic by DST, while Feng et al. (2013) found a lower modulus in GM. Both studies found similar, approximately isotropic, loss factors, in both GM and WM by DST.

Taking into account differences in frequency and anatomical region, the current parameter estimates from MRE may be compared to results in the literature obtained by direct mechanical testing. Arbogast and Margulies (1998) studied porcine WM brain tissue (brainstem) using DST from frequencies $\sim 20 - 200$ Hz, spanning much of the range of the MRE experiment. They found shear modulus values at 100 and 200 Hz similar to ours ($\sim 1.7 - 2.25$ kPa) and shear anisotropy ratio similar to the current estimate ($\phi \sim 0.3$). It should be noted that Arbogast and Margulies (1998) used a much higher strain ($2.5 - 7.5$ %) than was applied in either the current DST or MRE tests. Hrapko et al. (2008) studied porcine brain (corona radiata, acquired within three different directional planes) using rotational rheometry within the frequency range of $1 - 10$ Hz. The shear anisotropy ratio in the corpus callosum region, estimated in the current MRE-based study is similar to the corresponding estimate from Hrapko et al. (2008) (~ 0.3 vs $\sim 0.2 - 0.4$, respectively), despite the significant difference in actuation frequency ($100 - 300$ Hz vs $1 - 10$ Hz, respectively). Average shear moduli from Hrapko et al. (2008) are consistent with our DST estimates ($\sim 0.4 - 0.6$ kPa at $1 - 10$ Hz vs ~ 0.65 kPa at $20 - 30$ Hz, respectively).

The anisotropy estimated in the current study is mild (i.e., not an order of magnitude) and not as large as what might be expected given the diffusion anisotropy of brain WM. The degree of

anisotropy is also smaller than the level assumed in recent modeling studies (Giordano et al., 2014). The level of anisotropy is consistent with the magnitude of the directional dependence of shear moduli observed by Anderson et al. (2016).

The current study is limited by the assumption that the tissue is linearly viscoelastic with loss factors typical of brain ($\eta \approx 0.5$) and gelatin ($\eta \approx 0.1$). Loss factors were not optimized by fitting, but provided attenuation of shear waves similar to that observed in experiments. The assumption of incompressibility may introduce some errors in the current study and *in vivo* studies, due to the actual slight compressibility of tissue and the consequent existence of longitudinal waves (although the curl operation is intended to eliminate longitudinal waves from the MRE analysis). The assumption of an unbounded, uniform domain is not necessary because the FE model includes bounded sub-domains with different properties. It should be noted, however, that shear waves traveling through WM tissue may be influenced by nearby GM, as perfect segmentation between tissue types was not possible. Structural anisotropy of the experiment as a whole does affect wave motion, and thus may influence estimates of material anisotropy (intrinsic) based on global features of wave propagation (elliptical axis ratio). Local estimates of wavelength should not be strongly affected. Manual identification of points on ellipses may also introduce imprecision. Importantly, we have made no attempt to quantify the tensile anisotropy, which is likely to exist and to be important in brain behavior, but which is not manifested under these experimental conditions. Future studies will focus on: (i) complementary estimates of tensile anisotropy of WM using MRE with “fast” or quasi-transverse/QT shear waves which introduce fiber stretch; and (ii) estimation of shear and tensile anisotropy in the human brain *in vivo*.

4.6 Conclusions

White matter in the porcine brain *ex vivo* was found to be mildly anisotropic in shear using MRE. Anisotropic material parameters were estimated from the parameters of FE simulations that most closely matched data from MRE experiments. These material parameter estimates enhance our understanding of the mechanical properties of WM in brain tissue *ex vivo*, and provide confidence in our future ability to estimate anisotropic mechanical properties of WM in the intact, living brain. Ultimately, MRE-derived estimates of anisotropic properties of WM *in vivo* will lead to improved computational models of brain biomechanics and deeper understanding of TBI.

Chapter 5: Probing mechanical nonlinearity of soft tissue: a path forward using MRE

5.1 Overview: Nonlinear mechanical characterization of soft tissues

In this chapter, a preliminary theoretical and computational study is presented to demonstrate the potential of MRE to probe nonlinear material behavior. This study is performed to assess the feasibility of future experimental studies, and to guide the development of appropriate procedures. The effect of nonlinear deformation on shear waves and thus MRE experiments is shown analytically and via finite element simulation using an assumed nonlinear constitutive model. Finally, a possible experimental apparatus and protocol are presented, along with proposed post-processing methods.

5.2 Significance

Elastographic methods such as MRE have been shown to be useful for non-invasive characterization of biological tissues (Manduca et al., 2001). Almost no published elastographic studies, however, characterize soft tissue past the linear regime. Elastographic methods are appropriate for human studies since small magnitude tissue strains are safe. In phantoms, tissue surrogate biomaterials, or *ex vivo* tissue, however, mechanical characterization can be performed past the linear regime. This is important because, for example, injury thresholds in brain tissue have been found to exceed 0.2 strain in neural tissue (optic nerve; Bain and Meaney, 2000).

MRE can also be used to study nonlinear behavior of tissue surrogate materials or *ex vivo* tissue. Studying nonlinear behavior of soft tissues by MRE could eliminate some of the difficulties associated with direct mechanical tests of soft materials, especially slippage when gripping tissue, ambiguous and/or heterogeneous contact between the tissue and the instrument, and environmental factors like tissue dehydration. This chapter describes the potential use of MRE to study nonlinear properties of soft tissue.

5.3 Nonlinear deformation effects on shear waves

5.3.1 Brief theoretical review

In prior studies (Chatelin et al., 2013; Gasser et al., 2006; Meaney, 2003) soft tissues have been modeled as hyperelastic or hyper-viscoelastic materials. In a hyperelastic material model, the stress-strain relationship is derivable from a strain-energy density function (Ogden, 1997). The first hyperelastic models developed were Neo-Hookean and Mooney-Rivlin solids, developed to describe the behavior of rubber under large deformations (Mooney, 1940; Rivlin, 1948). In this study, we will start with a Neo-Hookean material model, and extend it to include contributions to the strain energy from higher order powers of the first invariant (I_1), i.e. by the selecting the Yeoh material model (Martins et al., 2006). We will derive theoretical shear wave speeds from the acoustic tensor that governs infinitesimal shear waves superimposed on finite deformations.

In terms of the material parameters used in the commercial software, ABAQUS (“ABAQUS Documentation, Dassault Systemes,” 2014), a Neo-Hookean strain energy density is defined as:

$$W = C_{10}(\bar{I}_1 - 3) + \frac{1}{D_1}(J - 1)^2, \quad (5.1)$$

where W is the strain energy per unit of reference volume; C_{10} and D_1 are the material parameters. Given the deformation gradient tensor $\mathbf{F} = \frac{\partial \mathbf{x}}{\partial \mathbf{X}} (F_{iR} = \frac{\partial x_i}{\partial X_R})$, $\mathbf{C} = \mathbf{F}^T \mathbf{F}$, $I_1 = \text{trace}(\mathbf{C})$, $I_1 = \det(\mathbf{C})$, and $J = \det \mathbf{F} = I_3^{1/2}$, \bar{I}_1 is the first deviatoric strain invariant defined as: $\bar{I}_1 = \bar{\lambda}_1^2 + \bar{\lambda}_2^2 + \bar{\lambda}_3^2$ where the deviatoric stretches $\bar{\lambda}_i = J^{-\frac{1}{3}} \lambda_i$; λ_i are the principal stretches, and J is the volume ratio. The initial shear modulus and bulk modulus (which govern small deformations with respect to the un-deformed reference configuration) are given by:

$$\mu_0 = 2C_{10}, \text{ and } K_0 = \frac{2}{D_1}. \quad (5.2)$$

The neo-Hookean material model is readily extended to the Yeoh material model. The Yeoh strain energy potential is implemented in ABAQUS (“ABAQUS Documentation, Dassault Systemes,” 2014) as:

$$W = C_{10}(\bar{I}_1 - 3) + C_{20}(\bar{I}_1 - 3)^2 + C_{30}(\bar{I}_1 - 3)^3 + \frac{1}{D_1}(J^{el} - 1)^2 + \frac{1}{D_2}(J^{el} - 1)^4 + \frac{1}{D_3}(J^{el} - 1)^6 \quad (5.3a)$$

where C_{20} , C_{30} , D_2 and D_3 are higher order material parameters. For simplicity, in this study we set $C_{20} = 0$ and neglect higher order volumetric terms involving D_2 and D_3 , so W becomes:

$$W = C_{10}(\bar{I}_1 - 3) + C_{30}(\bar{I}_1 - 3)^3 + \frac{1}{D_1}(J^{el} - 1)^2. \quad (5.3b)$$

In nonlinear materials, the equation of motion $\frac{\partial}{\partial x_j} \sigma_{ij} = \rho \frac{d^2 u_i}{dt^2}$ can be linearized and written for incremental motion, with $u_i = u_{0i} + \tilde{u}_i$, where the “0” subscript indicates the deformation applied to reach an operating point (finite strain) and “ \sim ” indicates the incremental motion (linearization about a point). The incremental constitutive law for an elastic solid can then be written as:

$$\sigma_{ij} = \sigma_{0ij} + A_{0ijkl}\tilde{\varepsilon}_{0kl}, \quad (5.4)$$

where A_{0ijkl} is the incremental elasticity tensor, and the incremental strain can be written as:

$$\tilde{\varepsilon}_{0kl} = \frac{1}{2} \left(\frac{\partial \tilde{u}_k}{\partial x_l} + \frac{\partial \tilde{u}_l}{\partial x_k} \right). \quad (5.5)$$

Note that Cartesian coordinates are used throughout. The incremental elasticity tensor has the form:

$$A_{0ijkl} = \frac{\partial^2 W}{\partial F_{jR} \partial F_{lS}} F_{iR} F_{kS}, \quad (5.6)$$

The nominal deformation gradient tensor in simple shear can be expressed as a matrix in Cartesian coordinates:

$$\mathbf{F} = \begin{bmatrix} 1 & \alpha & 0 \\ 0 & 1 & 0 \\ 0 & 0 & 1 \end{bmatrix} \text{ where } \alpha = \tan(\theta) = \frac{u_0}{d}, \quad (5.7)$$

where α defines the magnitude of the imposed simple shear, θ is the angle of the imposed simple shear, and d is the length of the side of the solid.

For simulations of simple shear, strains on the material will be expressed in terms of engineering strain $\gamma_{12} = 2\varepsilon_{12}$. The FE simulation software ABAQUS provides results in terms of logarithmic strain:

$$\varepsilon_{12}^{log} = \ln(\mathbf{V}), \quad (5.8)$$

where the left stretch tensor, $\mathbf{V} = \sqrt{\mathbf{F} \cdot \mathbf{F}^T}$.

We will use the logarithmic engineering shear strain to describe finite deformations:

$$\gamma_{12}^{log} = 2\varepsilon_{12}^{log}. \quad (5.9)$$

For infinitesimal strain in ideal simple shear, $\alpha = \gamma_{12}^{log}$. As α increases, there will be small differences between α and γ_{12}^{log} ; for the largest α used in this model (0.20), the difference is $\sim 0.6\%$. Figure 5.1 demonstrates the deformation and strains applied to a solid (a) and the dynamic, incremental deformation (b).

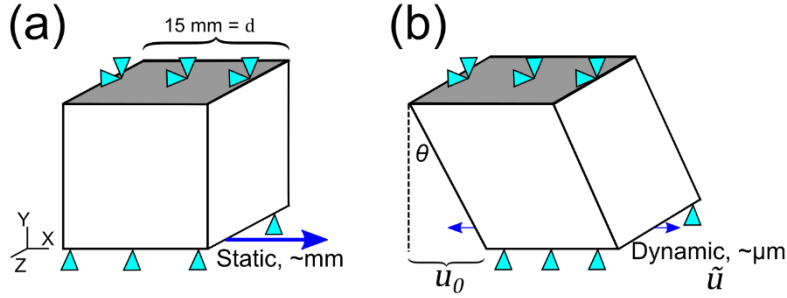


Figure 5.1: Free-body diagram of a solid undergoing two deformations. (a) a static, finite deformation of a solid body to a specified operating point (u_0 ; corresponding to experimental displacement on the order of millimeters). (b) a superimposed dynamic deformation (\tilde{u}) associated with incremental displacements on the order of micrometers. The angle, θ , represents the angle of imposed shear.

To extend this theory to a propagating plane wave we start with the equation:

$$\tilde{\mathbf{u}}(\mathbf{x}, t) = \tilde{\mathbf{u}}_a \exp[iK(\mathbf{n} \cdot \mathbf{x} - ct)] = \tilde{\mathbf{u}}_a \mathbf{m} \exp(i\omega t - K \mathbf{n} \cdot \mathbf{x}), \quad (5.10)$$

where I refers to the imaginary number ($\sqrt{-1}$), wave propagation is designated by the unit vector, \mathbf{n} , and the polarization direction (direction of particle motion) is specified by the vector \mathbf{m} , where $\tilde{\mathbf{u}}_a = \tilde{u}_a \mathbf{m}$. The propagation speed $c = \omega/k$ (m/s), where K is the wavenumber (rad/m) and ω is frequency (rad/s). Substituting this equation into the equation of motion:

$$\frac{\partial}{\partial x_j} \left(A_{0ijkl} \frac{\partial \tilde{u}_k}{\partial x_l} \right) = \rho \frac{\partial^2 \tilde{u}_i}{\partial t^2}, \quad (5.11)$$

we have the following eigenvalue problem:

$$A_{0ijkl} n_j n_l m_k = \rho c^2 m_i \text{ or } Q_{ik} m_k = \rho c^2 m_i. \quad (5.12)$$

Here the Cartesian components of the acoustic tensor are $Q_{ik} = A_{0ijkl} n_j n_l$. The eigenvalue problem may be solved to find the wave propagation speeds (c^2) and polarization directions (\mathbf{m}) of plane wave solutions. The deviatoric incremental acoustic tensor is determined by the material parameters and is shown below for a Yeoh material model with a wave propagation vector, $\mathbf{n} = [0 \ 1 \ 0]$, indicating a downward propagating wave in the y direction and at a finite shear strain quantity α :

$$Q = \begin{bmatrix} 2C_{30}\alpha^6 + 30C_{30}\alpha^4 + \frac{2}{3}C_{10}\alpha^2 + 2C_{10} & -\frac{4}{3}\alpha(9C_{30}\alpha^4 + C_{10}) & 0 \\ -\frac{4}{3}\alpha(9C_{30}\alpha^4 + C_{10}) & 8\left(C_{30}\alpha^6 + C_{30}\alpha^4 + \frac{2}{9}C_{10}\alpha^2 + \frac{C_{10}}{3} + \frac{\kappa}{8}\right) & 0 \\ 0 & 0 & \frac{2}{3}(\alpha^2 + 3)(3C_{30}\alpha^4 + C_{10}) \end{bmatrix}. \quad (5.13)$$

For the wave propagation vector indicated above, and in the limit as the bulk modulus approaches infinity, the following eigenvalues are found:

$$\lambda_1 = \rho c_l^2 \rightarrow \infty, \lambda_2 = \rho c_s^2 = \frac{2}{3}(\alpha^2 + 3)(3C_{30}\alpha^4 + C_{10}) \text{ and } \lambda_3 = \rho c_f^2 = 2C_{30}\alpha^6 + 30C_{30}\alpha^4 + \frac{2}{3}C_{10}\alpha^2 + 2C_{10}, \quad (5.14a-c)$$

where ρ is the density of the material, c_s and c_f refer to the slow (also known as “pure transverse”) and fast (“quasi-transverse”) shear wave speed respectively, and c_l refers to the longitudinal wave speed.

5.3.2 Finite element simulations of nonlinear deformations and MRE

To gain more intuitive understanding of the theory of waves in nonlinear materials and insight into the application of nonlinear material models to a MRE experiment, finite element (FE) models of shear waves in deformed samples were created. The FE models were assigned a Yeoh hyperelastic material model and were of a physical size similar to that studied in MRE experiments (Schmidt et al., 2016). Practically, to perform nonlinear MRE studies, two deformations must occur in series. First, a relatively large finite deformation is imposed to strain

the solid to a specified operating point (Figure 5.1a). Second, a small dynamic excitation is applied to produce (infinitesimal) shear waves superimposed on the finite deformation (Figure 5.1b), similar to the procedure in a traditional elastography experiment (Schmidt et al., 2016).

A 3D FE model of the proposed experiment was created using ABAQUS CAE 6.14-2. The model consists of a $15 \times 15 \times 15 \text{ mm}^3$ cube representing mechanically isotropic soft tissue. The cube was assigned nominal soft tissue properties (Table 5.1) in a Yeoh material model. The properties (C_{30}) were selected such that the shear stiffness will increase approximately by three-fold at 0.2 strain, compared to its properties in the undeformed reference configuration. The steps of the model were defined as follows:

- Step 0, the initial boundary conditions were applied to the model:
 - The top ($Y=d=15 \text{ mm}$) face was fixed (assigned values of zero to U_1 , U_2 , U_3 ; corresponding to displacements in the X, Y, and Z directions, respectively)
 - The bottom ($Y=0$) was fixed in the Y and Z directions for the duration of the studies (assigned values of zero to U_2 and U_3).
 - The other sides of the cube remained free.
- Step 1, the large deformation (millimeter magnitude) step was implemented with the following boundary conditions:
 - the bottom ($Y=0$) surface was given a displacement of $[0, 0.75, 1.50, 2.25, 3.0]$ mm corresponding to imposed simple shearing strains of $[0, 0.05, 0.10, 0.15, 0.20]$.
- Step 2, the superimposed shear waves displacements (micrometer magnitude) were induced in the model by the following boundary conditions:

- the application of oscillating micrometer displacements in the X-direction of $U_1=2.5 \times 10^{-5}$ meters at a frequency of 600 Hz (steady-state dynamics, frequency domain) on the bottom surface ($Y=0$) of the cube after the displacements in Y and Z were fixed.

Figure 5.2 shows the different steps and the U_1 (in the X direction) deformations encountered in each step.

Yeoh parameters:			Intended units (SI; meter)
	C10	500	Pa
	C20	0	--
	C30	50000	--
	D1	1×10^{-5}	--
	D2	100000	--
	D3	100000	--
Density		1000	kg/m ³
Viscoelastic parameters:			
	Re[g1*]	0.0159	--
	Im[g1*]	1×10^{-5}	--
	A	1	--
	Re[k1*]	1×10^{-5}	--
	Im[k1*]	1×10^{-5}	--
	B	1	--

Table 5.1: Material parameters assigned to the FE model. The column on the right indicates the intended units of the parameters. Large values for D_2 and D_3 are chosen to neglect higher order volumetric terms (see Equation 5.3b).

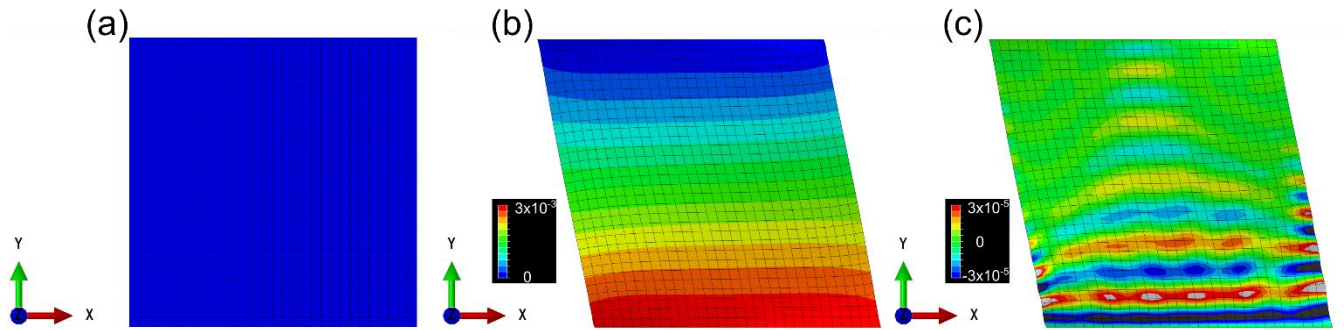


Figure 5.2: Deformations applied to the 15mm^3 model in step 0 (a), step 1 (b), and step 2 (c). Step 0, the initial step, does not involve any displacements or strains on the material. Step 1, the deformation of the solid to the operating point involves finite strain, and displacements on the order of mm. Step 2, the incremental displacement involves harmonic displacements on the order of μm at 600 Hz.

Figure 5.3 shows the strain distribution and deformations in the different steps of the simulation across the array of simulations performed.

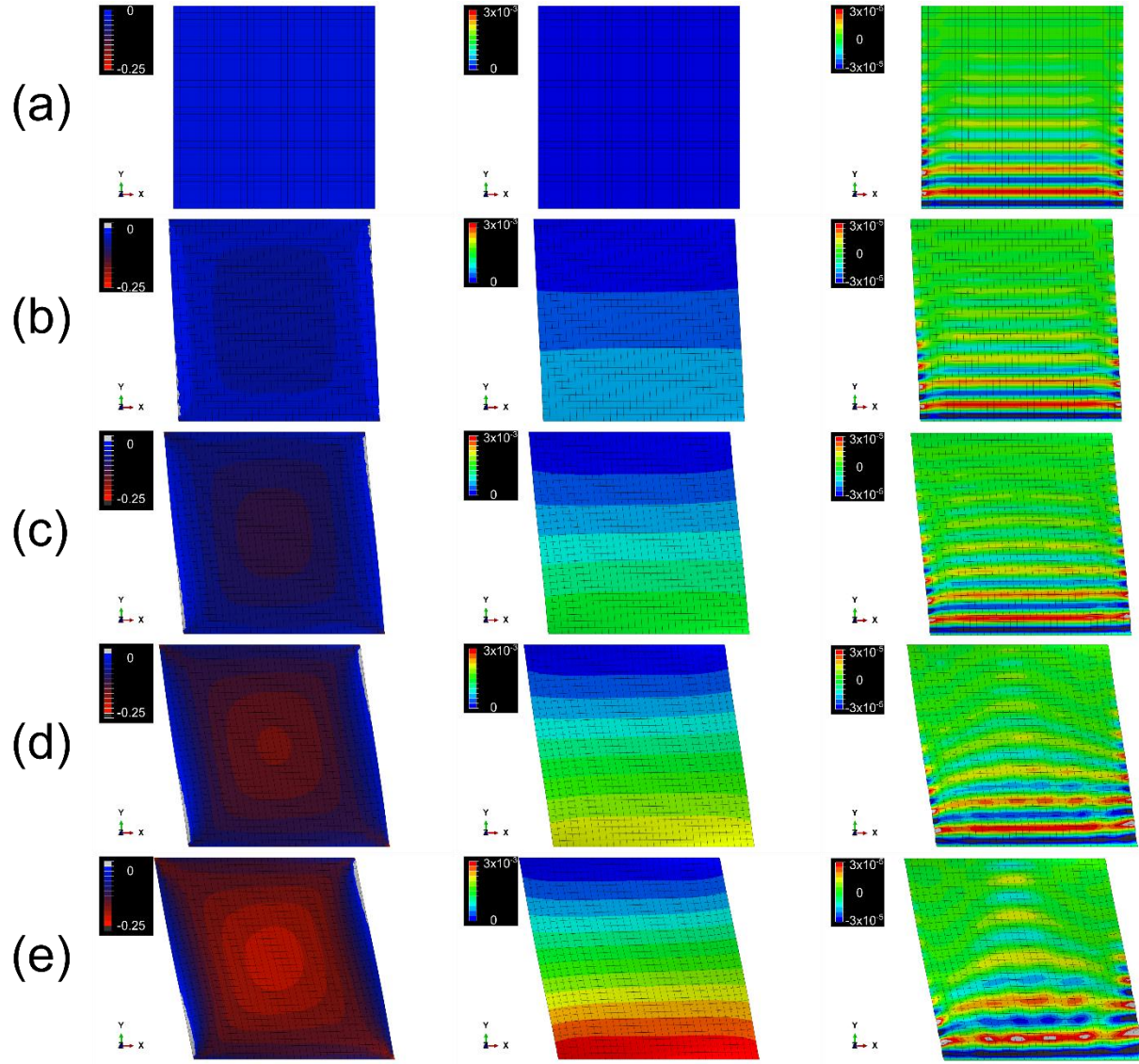


Figure 5.3: (first column) Logarithmic shear strain (γ_{12}^{log}) and (second column) displacement in the FE model after the imposed deformation of step 1. (third column) Shear waves in the model from step 2 at a frequency of actuation of 600 Hz. Rows (a-e) correspond to applied finite displacements of [0, 0.75, 1.50, 2.25, 3.0] mm and thus to the targeted imposed strains (α) of [0, 0.05, 0.10, 0.15, 0.20].

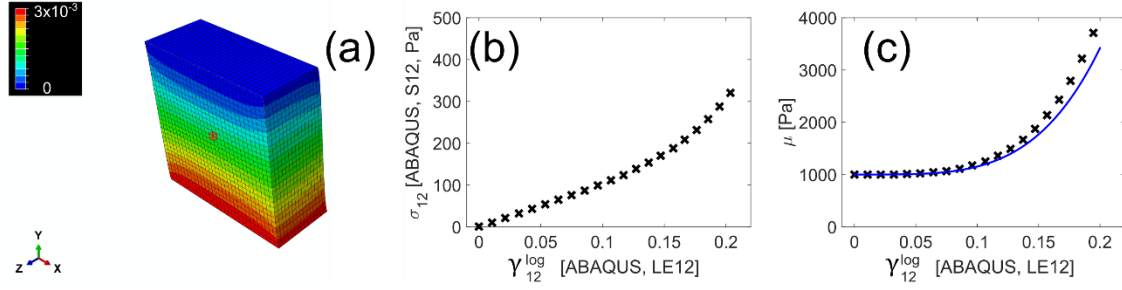


Figure 5.4: Stress and strain in the center of the FE model during the large deformation step (step 1). (a) Half of the model is displayed (cut plane is the YX plane). All data in (b) and (c) are from the element highlighted in red in the middle (in X, Y, and Z directions) of the model. (b) Shear stress as a function of shear strain. Note the increase of stress as the strain is increased. (c) The derivative of the data in (b) showing the instantaneous (tangent) shear modulus at different strain states. Data are compared to theoretical predictions (blue line).

5.3.3 Data analysis

We aim to detect either (1) a change in shear wavelength if using local frequency estimation (LFE) inversion (Knutsson et al., 1994) or manual measurement (Schmidt et al., 2016) or (2) a change in apparent shear modulus estimated by local direct inversion (LDI) methods (Okamoto et al., 2011b). In the finite element study above, parameters were chosen so the change in material properties was evident at $\alpha \sim 0.2$ strain. Figure 5.5 shows the change in shear wavelength (a) and shear moduli (b) with shear strain (0 to ~ 0.2).

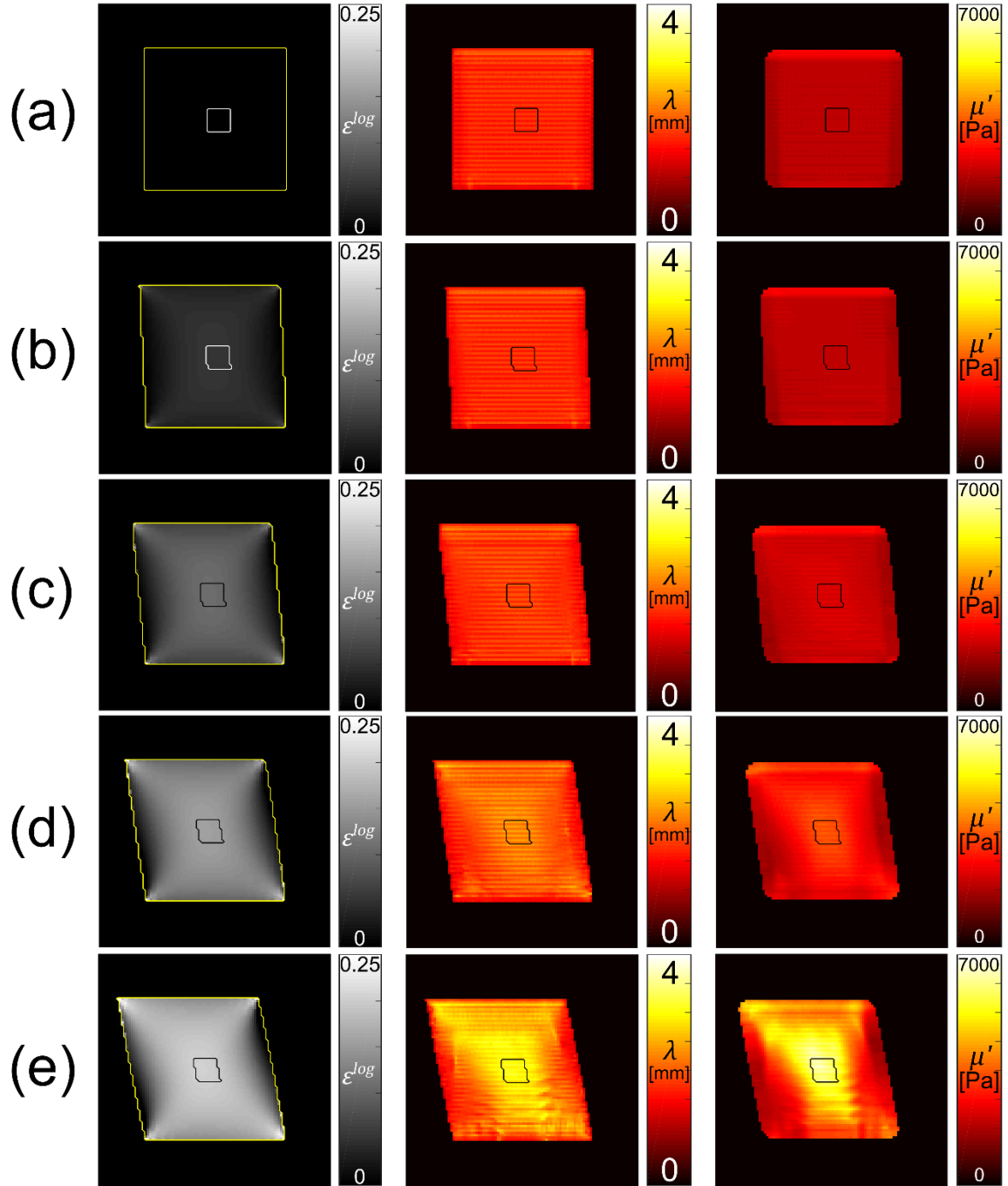


Figure 5.5: Overview of logarithmic strain from ABAQUS (left column), estimates of shear modulus from local frequency estimation inversion (center column), and estimates of shear modulus local direct inversion (right column). Rows (a) – (e) represent differing operating points: applied strains of [0, 0.05, 0.10, 0.15, 0.20], respectively. The box within the deformed cube represents the area in the xy plane where data were averaged.

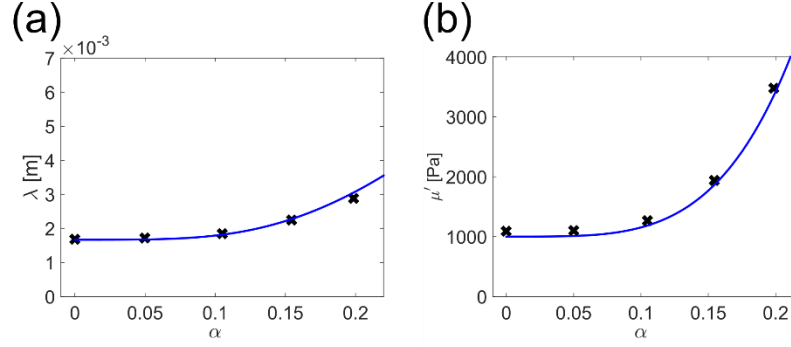


Figure 5.6: Results of shear wave inversion in a deformed cube of Yeoh material, compared to theoretical predictions. Shear wavelength and shear modulus increase with finite deformation. Each black “x” represents averages in the boxed region of the corresponding panel in Figure 5.5: either the middle column (local frequency estimation, LFE, Knutsson et al., (1994)) or right column (local direct inversion, LDI, Okamoto et al., (2011b)). (a) Shear wavelength, estimated by LFE, increases with finite deformation. (b) Shear modulus, estimated by LDI, increases with finite deformation.

5.4 Proposed experimental methods

5.4.1 Overview

The experimental execution of this study poses several challenges. First, consistent finite deformation of tissue is required. Researchers performing mechanical tests on biological tissue must account for the viscoelastic relaxation of the tissue after a force is applied. In effect, relaxation would cause the tissue to seem less stiff over the course of an MRE study (on the order of minutes). Thus, it is important that the large finite deformation is applied semi-harmonically, such that the tissue only stays stationary in a deformed state for less than its relaxation time, before releasing the deformation back to the un-deformed state and repeating the process.

To achieve a consistent displacement, an automated and controlled mechanism for finite deformation is necessary. Any apparatus operating within an MRI scanner must not contain ferrous materials, and should minimize non-ferrous metal in the bore of the scanner as well.

MRE studies on a similar sample size (Schmidt et al., 2016) typically use an actuator capable of producing displacements on the order of tens of micrometers at frequencies of 50 – 2000+ Hz. However, these actuators are not capable of achieving displacements on the order of 3 – 5 mm, needed to impose finite strains. Thus, two separate actuators must be used in this study, one providing the large deformation and another providing the smaller “superimposed” deformation for MRE studies.

Hydraulics are a plausible way to transfer deformations from a computer-controlled actuator from an area outside the MRI scanner to the sample inside the scanner bore. This apparatus could be used in combination with the existing actuator used for MRE studies. Figure 5.7 shows the block diagram of a proposed system.

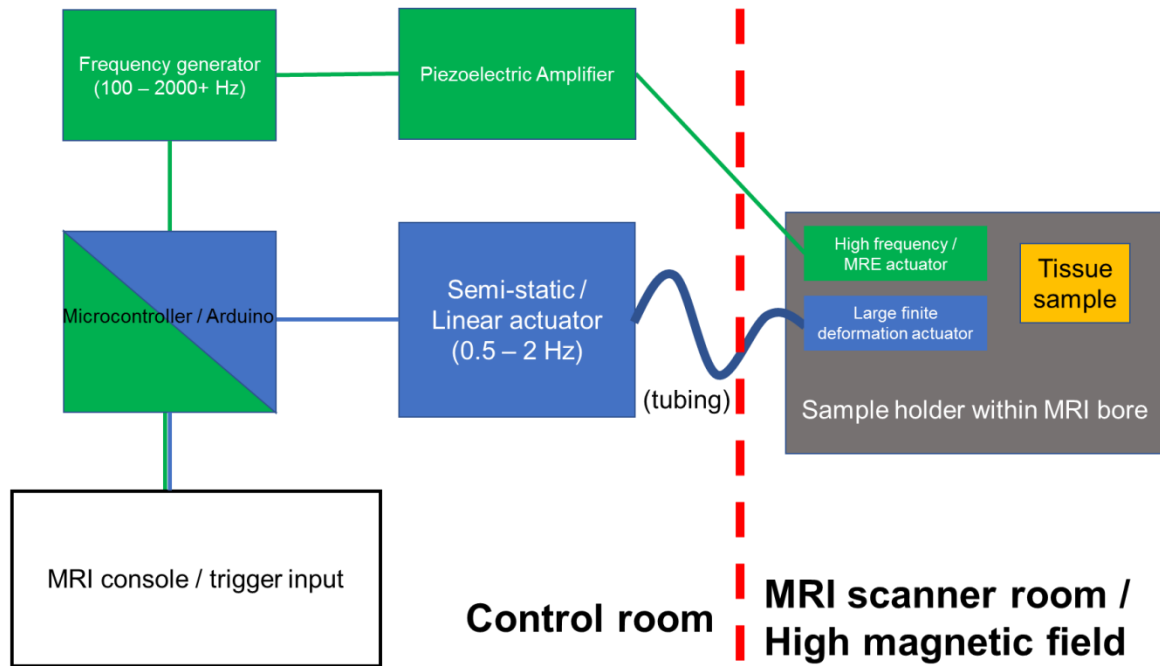


Figure 5.7: Overview of the proposed experimental design, including the locations of components with respect to the MRI console and high magnetic field found in and around the MR magnet. Blue components refer to the mechanism for finite deformation (using tubing for transferring the deformation from the control room to the MRI scanner). Green components refer to the mechanism to induce superimposed waves, which is similar to the actuation used in many MRE studies.

5.4.2 Experimental apparatus

The sample must be centered within the MRI bore; a concept drawing of the sample holder is shown in Figure 5.8. The large deformations will be imposed via the syringe (left) and the small superimposed deformations induced by the piezoelectric actuator (right). The piezoelectric actuator will be connected to the sample by the rod attached to the sample surface, and the large finite deformation will be applied by flow to the syringe, causing the syringe plunger to engage with a deformable sample container.

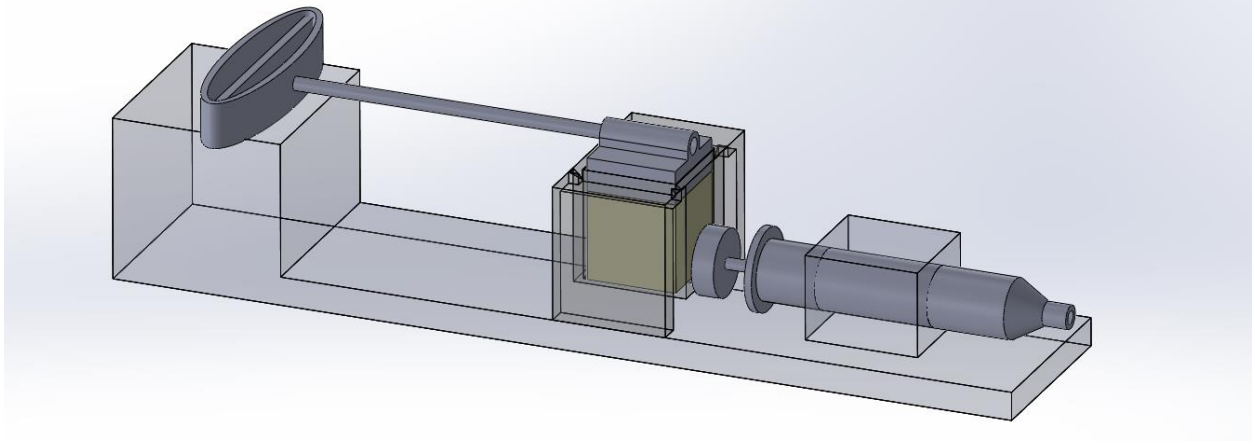


Figure 5.8: Concept drawing of a sample holder to be housed within the MR magnet bore. The system must deform the sample in shear to a specified operating point (displacements on order of mm), and induce shear wave deformations at high frequency (displacements on order of μm). The syringe on the right provides the large deformation and the piezoelectric actuator attached to the rod on the left provides high frequency, small-amplitude shear wave excitation (typically used in small animal and phantom MRE studies; Clayton et al., 2011; Schmidt et al., 2016).

A prototype of the deformable sample container is shown in Figure 5.9. The deformable container is made from a 3D printed material (PLA) and is in the shape of a cube. The cube in Figure 5.9 (a) is printed as shown and the finished product in Figure 5.9 (b) is formed by melting PLA to bond two sides of the cube together. The cube is capable of deforming to an imposed shear strain of $\alpha \sim 0.2 - 0.3$.

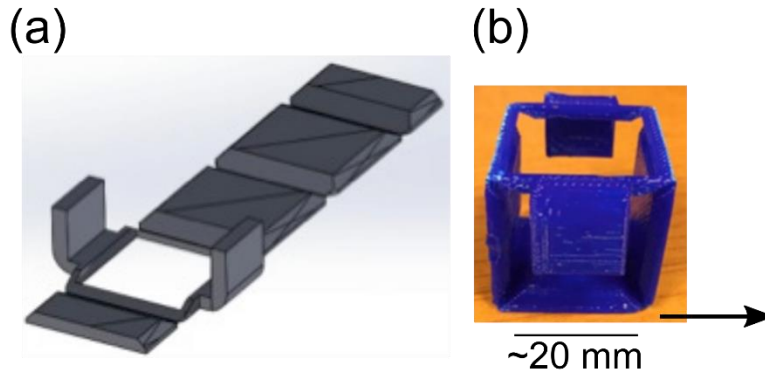


Figure 5.9: Sample holder (deformable cube) prototype. (a) CAD drawing of the deformable cube. (b) the finished sample holder cube; deformable by the application of force in the direction of the black arrow.

To supply the fluid pressure and thus deformation of the cube via the syringe, the syringe must be moved a consistent amount in a cyclic fashion. Figure 5.10 shows the linear actuator attached to a syringe to supply the necessary fluid pressure to actuate the corresponding syringe located within the MRI scanner (through tubing). The setup is held in position by a rigid piece of aluminum. The linear actuator (Actuonix 16-50-63-6-R) is controlled by a generic Arduino (Uno R3) microcontroller via attachment to the 5V, GND, and digital pulse-width modulated (PWM) terminals. Depending on the length of the PWM pulse (1000 – 2000 μs), the actuator can be moved from home (0 mm) to extended position (50 mm), respectively.

The scanner and MRE sequences require a trigger to synchronize the superimposed shear deformations with the imaging gradients. The micro-controller would communicate with the scanner when the sample is able to be scanned (when the sample is at the intended operating point) and when it should not be scanned (when the linear actuator and syringe are moving). Thus, the microcontroller will then “pass-through” the function generator’s relatively high frequency signal during the specified intervals. This functionality is detailed in Figure 5.11.



Figure 5.10: Proposed apparatus to provide finite deformation within MR scanner. Linear actuator (left) connected to a syringe filled with fluid (right) – intended to stay within the MRI control room. The syringe is attached by tubing to the corresponding syringe within the apparatus in Figure 5.7. The linear actuator is controlled by a micro-controller.

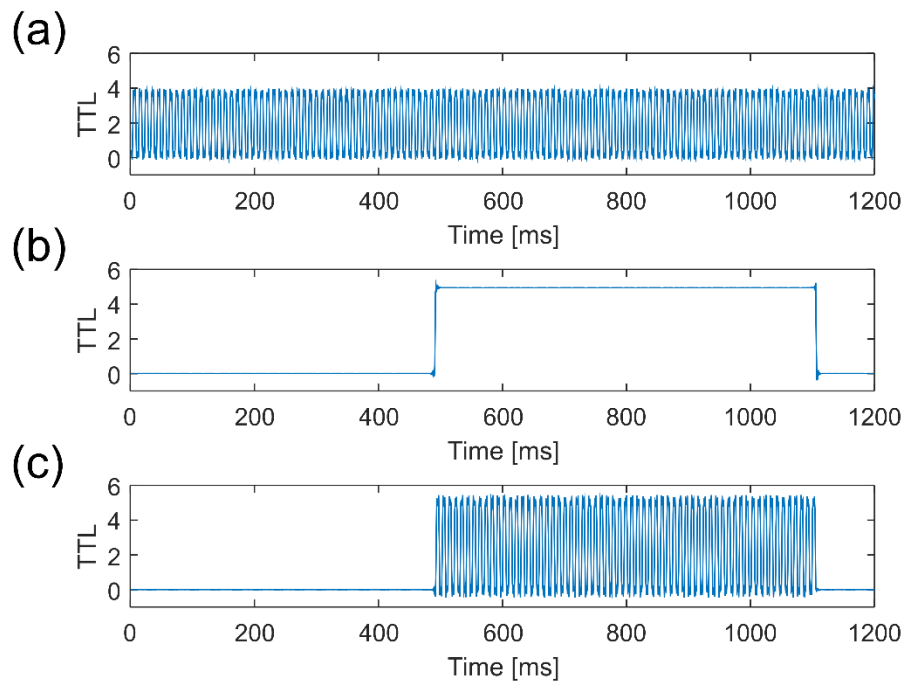


Figure 5.11: A micro-controller (Arduino Uno R3) can combine input signals and output pulses to control scanning. (a) The function generator that drives the piezoelectric actuator can provide a TTL signal at the vibration frequency (e.g., 100 Hz), as input to the micro-controller. (b) An analogous TTL signal can be provided by the finite deformation mechanism as input to the micro-controller. The signal is 5V when the deformation has been performed and the sample is in-position and 0V otherwise. (c) A combination of these signals (AND operator), will be output from the micro-controller to trigger the scanner.

5.4.3 Experimental protocol

The MRE protocol for this study resembles the other MRE studies detailed in this thesis, particularly in Chapter 3. A modified spin-echo MRI sequence (Feng et al., 2013a) will be used, triggered only when the large deformation has been performed and the syringe is not in motion (see Section 5.4.2). An MRE actuation frequency should be selected which allows the appropriate amount of shear wavelengths to be visible in the sample during both the un-deformed study as well as when the tissue is stretched and the stiffness (and thus shear wavelength) is increased. For example, a frequency of 500-600 Hz should suffice if the tissue nominal linear shear modulus is 1000 Pa (see the FE study in Section 5.3.3). Analysis of the 3D displacement fields should proceed in a similar fashion to 5.3.3.

5.5 Conclusions

This chapter describes a method to measure shear waves and estimate nonlinear material parameters in soft tissue using MRE. Theoretical wave speeds were computed for shear waves superimposed on finite deformations in a standard, nonlinear, hyperelastic (Yeoh) material. Corresponding FE models were created with an initial finite shear strain and superimposed shear waves. Using the assumed material model, the superimposed shear waves had longer wavelengths when the material was under higher finite strains, consistent with analytical predictions. Finally, an experimental protocol was proposed to perform this experimental measurement in soft tissues and biomaterials. The results of this study could potentially provide useful information to compare with direct mechanical tests of the nonlinear properties of white matter in the brain.

Chapter 6: Summary, Conclusions, and Future Directions

This thesis focuses on the application of MR elastography to extend our understanding of fibrous soft tissues, especially white matter in the brain. Experimental methods were established to use MR elastography to characterize nearly incompressible, transversely isotropic linear elastic materials. Experimental methods were also proposed, along with simulation and analytical work, to extend these methods to the nonlinear regime.

6.1 Summary of Work

The original specific aims of the dissertation are below. Over the last year, the dissertation scope has been modified slightly, in part to facilitate a pilot project on MRE in the mouse liver, funded by industry (Genentech). However, significant progress on each Aim has been achieved. The findings achieved during each of the aims are summarized shortly below each aim.

Aim 1: Develop a method to identify separate contributions of anisotropic shear and tensile moduli to the wave propagation in fibrous materials such as ex vivo muscle tissue and aligned fibrin gels.

A method was developed to characterize the shear and tensile moduli of fibrous tissues using MR elastography. The separate contributions of the anisotropic shear and tensile moduli were found by estimating the wave speed of two separate shear waves. These efforts are described in

Chapter 3. This study was the first to separate and estimate two separate shear waves in fibrous materials in this field.

Aim 2: *Estimate the shear and tensile anisotropic parameters of ex vivo white matter.*

Using the methods developed in Aim 1, anisotropic shear moduli of white matter *ex vivo* were estimated. Finite element models were created with plausible material properties and compared to experimental data. Using this “inverse” FE modeling approach, anisotropic shear moduli parameters were estimated for *ex vivo* porcine brain tissue. These results are discussed in Chapter 4.

Aim 3: *Study the non-linear behavior of ITI tissue and tissue surrogates by imaging wave (infinitesimal) motion superimposed on larger (finite) deformations.*

The non-linear behavior of an isotropic, hyperelastic (Yeoh material), was studied analytically and via finite element simulation. A corresponding experimental method and apparatus was proposed for future MRE studies of nonlinear behavior.

6.2 Limitations

6.2.1 MRI and MRE resolution

MRI offers lower imaging resolution than optical imaging and computed tomography. MRI has various advantages, however, including three-dimensional volume imaging and lack of exposure to ionizing radiation. The resolution of material property estimates from MRE is dependent on, and limited by, shear wavelength. To verify the existence of shear waves and obtain accurate estimates of shear wavelength in an MRE experiment, at a minimum, 7-8 voxels/wave must be present. Typically, spatial resolution on the order of 1/4 to 1/3 of the shear wavelength is

achievable, as needed to estimate the wavelength. In addition, estimates from MRE are frequently smoothed or averaged over a larger number of voxels.

6.2.2 Transverse isotropy as a model for fibrous tissues

The simplest model for anisotropic materials is transverse isotropy. In a transversely isotropic material, a single dominant fiber axis defines its symmetry, and properties are invariant with respect to rotations about this axis. As shown in Chapter 2, incompressible transversely isotropic materials can be described by three material parameters. Many biological tissues, especially white matter brain tissue contain a variety of fiber orientations within a small volume. Here these materials are approximated by models with a single fiber orientation. In Chapter 4, great effort was required to find white matter within the *ex vivo* porcine brain that most satisfied this assumption.

6.2.3 Assumption of material incompressibility

As noted in Chapter 2, the ability of three material parameters to describe transversely isotropic material behavior is based on the assumption of incompressibility. Most biological tissue is known to be slightly compressible, which leads to the existence of longitudinal waves in the material. Steps are taken to minimize the effects of these waves, including the use of the curl operator in isotropic materials or directional filtering. Because of their much longer wavelength, much of the displacement due to longitudinal motion at frequencies typically studied in this work (longest length scale < 5 cm), can be separated from the much shorter shear waves by simple high-pass spatial filtering.

6.3 Future directions

6.3.1 Orthotropic material models

Orthotropy allows for the characterization of materials with more than one fiber orientation. As explained in 6.2.2, biological tissues frequently exhibit diverse fiber orientations. Allowing for more fiber orientations would allow for characterization of more white matter regions within the brain.

6.3.2 Noncontact excitation

The use of acoustic radiation force (ARF) as the source of mechanical actuation for MRE studies would open an exciting frontier. In many of the studies described in Chapter 3 and 4, because of the proximity to contact with the actuation rod (punctured through the sample), much of the sample could not be characterized. In addition, with the existing apparatus, the sample cannot be repeatedly studied in different orientations. Acoustic radiation force, in contrast, would allow repeated excitation of motion deep in the material.

6.3.2 MRE applied to estimate nonlinear material properties

As outlined in Chapter 5, MRE has not yet been used to characterize the nonlinear properties of soft tissue. By combining a relatively large finite deformation with an incremental deformation found in MRE, nonlinear properties could be characterized. This technique might resolve the disparate results of the many direct mechanical characterization studies of soft tissue. MRE avoids several of the most important and challenging difficulties associated with direct mechanical tests, such as gaining traction on a soft tissue specimen and imposing consistent deformations (e.g., simple shear) consistent with the theory behind each method.

6.4 Conclusion

Soft tissue mechanical properties have been of interest to medicine for centuries. Their potential applications include insight into disease, improving the performance and reliability of implants, and increasing the accuracy of simulations of injury mechanics, especially TBI. Biological tissues exhibit complex behavior, such as material anisotropy and nonlinearity at finite strain, that should be taken into account. These complexities are addressed in this dissertation through the application of novel experimental MRE techniques and finite element analysis. The results from these studies increase our understanding of wave propagation through fibrous soft tissue and advance our ability to characterize these materials throughout development, aging, injury, and disease.

References

- ABAQUS Documentation, Dassault Systemes, 2014. . Providence, RI, USA.
- Anderson, A.T., Van Houten, E.E.W., McGarry, M.D.J., Paulsen, K.D., Holtrop, J.L., Sutton, B.P., Georgiadis, J.G., Johnson, C.L., 2016. Observation of direction-dependent mechanical properties in the human brain with multi-excitation MR elastography. *J. Mech. Behav. Biomed. Mater.* 59, 538–546. doi:10.1016/j.jmbbm.2016.03.005
- Arbogast, K.B., Margulies, S.S., 1998. Material characterization of the brainstem from oscillatory shear tests. *J. Biomech.* 31, 801–807.
- Aristizabal, S., Amador, C., Qiang, B., Kinnick, R.R., Nenadic, I.Z., Greenleaf, J.F., Urban, M.W., 2014. Shear wave vibrometry evaluation in transverse isotropic tissue mimicking phantoms and skeletal muscle. *Phys. Med. Biol.* 59, 7735–7752. doi:10.1088/0031-9155/59/24/7735
- Asbach, P., Klatt, D., Hamhaber, U., Braun, J., Somasundaram, R., Hamm, B., Sack, I., 2008. Assessment of liver viscoelasticity using multifrequency MR elastography. *Magn. Reson. Med.* 60, 373–379. doi:10.1002/mrm.21636
- Atay, S.M., Kroenke, C.D., Sabet, A., Bayly, P. V, 2008. Measurement of the dynamic shear modulus of mouse brain tissue in vivo by magnetic resonance elastography. *J. Biomech. Eng.* 130. doi:10.1115/1.2899575
- Auld, B.A., 1990. *Acoustic fields and waves in solids*, 2nd ed. Krieger Publishing Company, New York, NY.
- Bain, A.C., Meaney, D.F., 2000. Tissue-level thresholds for axonal damage in an experimental model of central nervous system white matter injury. *J Biomech Eng* 122, 615–622.
- Bayly, P. V, Cohen, T.S., Leister, E.P., Ajo, D., Leuthardt, E.C., Genin, G.M., 2005. Deformation of the human brain induced by mild acceleration. *J. Neurotrauma* 22, 845–856. doi:10.1089/neu.2005.22.845
- Benabid, A.L., Chabardes, S., Mitrofanis, J., Pollak, P., 2009. Deep brain stimulation of the subthalamic nucleus for the treatment of Parkinson’s disease. *Lancet Neurol.* 8, 67–81. doi:10.1016/S1474-4422(08)70291-6
- Böl, M., Ehret, A.E., Leichenring, K., Weichert, C., Kruse, R., 2014. On the anisotropy of skeletal muscle tissue under compression. *Acta Biomater.* 10, 3225–3234. doi:10.1016/j.actbio.2014.03.003
- Brands, D.W.A., Bovendeerd, P.H.M., Wismans, J.S.H.M., 2002. On the potential importance of non-linear viscoelastic material modelling for numerical prediction of brain tissue response: test and application. *Stapp Car Crash J.* 46, 103–121.
- Brum, J., Bernal, M., Gennisson, J.L., Tanter, M., 2014. *In vivo* evaluation of the elastic anisotropy of the human Achilles tendon using shear wave dispersion analysis. *Phys. Med. Biol.* 59, 505–523. doi:10.1088/0031-9155/59/3/505
- Chatelin, S., Deck, C., Willinger, R., 2013. An anisotropic viscous hyperelastic constitutive law

- for brain material finite-element modeling. *J. Biorheol.* 27, 26–37. doi:10.1007/s12573-012-0055-6
- Chou, P.C., Pagano, N.J., 1992. *Elasticity : tensor, dyadic, and engineering approaches*. Dover Publications, New York.
- Clayton, E.H., Garbow, J.R., Bayly, P. V., 2011a. Frequency-dependent viscoelastic parameters of mouse brain tissue estimated by MR elastography. *Phys. Med. Biol.* 56, 2391–2406. doi:10.1088/0031-9155/56/8/005
- Clayton, E.H., Garbow, J.R., Bayly, P. V., 2011b. Frequency-dependent viscoelastic parameters of mouse brain tissue estimated by MR elastography. *Phys Med Biol* 56, 2391–2406. doi:S0031-9155(11)77666-7 [pii]10.1088/0031-9155/56/8/005
- Coronado, V.G., Xu, L., Basavaraju, S. V., McGuire, L.C., Wald, M.M., Faul, M.D., Guzman, B.R., Hemphill, J.D., Centers for Disease Control and Prevention (CDC), 2011. Surveillance for traumatic brain injury-related deaths--United States, 1997-2007., *Morbidity and mortality weekly report. Surveillance summaries* (Washington, D.C. : 2002). doi:2011-723-011/21044
- Desmoulin, G.T., Dionne, J.-P., 2009. Blast-Induced Neurotrauma: Surrogate Use, Loading Mechanisms, and Cellular Responses. *J. Trauma Inj. Infect. Crit. Care* 67, 1113–1122. doi:10.1097/TA.0b013e3181bb8e84
- Faul, M., Xu, L., Wald, M., Coronado, V., 2010. Traumatic Brain Injury in the United States: Emergency Department Visits, Hospitalizations and Deaths 2002-2006.
- Feng, Y., Clayton, E.H., Chang, Y., Okamoto, R.J., Bayly, P. V., 2013a. Viscoelastic properties of the ferret brain measured in vivo at multiple frequencies by magnetic resonance elastography. *J. Biomech.* 46, 863–870. doi:10.1016/j.jbiomech.2012.12.024
- Feng, Y., Lee, C.H., Sun, L., Ji, S., Zhao, X., 2017. Characterizing white matter tissue in large strain via asymmetric indentation and inverse finite element modeling. *J. Mech. Behav. Biomed. Mater.* 65, 490–501. doi:10.1016/j.jmbbm.2016.09.020
- Feng, Y., Okamoto, R.J., Namani, R., Genin, G.M., Bayly, P. V., 2013b. Measurements of mechanical anisotropy in brain tissue and implications for transversely isotropic material models of white matter. *J. Mech. Behav. Biomed. Mater.* 23, 117–132. doi:10.1016/j.jmbbm.2013.04.007
- Fitzgibbon, A., Pilu, M., Fisher, R.B., 1999. Direct least square fitting of ellipses. *IEEE Trans. Pattern Anal. Mach. Intell.* 21, 476–480. doi:10.1109/34.765658
- Flügge, W., 1975. *Viscoelasticity*, 2d rev. ed. Springer-Verlag, New York, NY.
- Gasser, T.C., Ogden, R.W., Holzapfel, G.A., 2006. Hyperelastic modelling of arterial layers with distributed collagen fibre orientations. *J. R. Soc. Interface* 3, 15–35. doi:3253307783333263 [pii] 10.1098/rsif.2005.0073
- Gennisson, J.L., Catheline, S., Chaffai, S., Fink, M., 2003. Transient elastography in anisotropic medium: Application to the measurement of slow and fast shear wave speeds in muscles. *J. Acoust. Soc. Am.* 114, 536–541. doi:Doi 10.1121/1.1579008
- Giordano, C., Cloots, R.J.H., van Dommelen, J.A.W., Kleiven, S., 2014. The influence of anisotropy on brain injury prediction. *J. Biomech.* 47, 1052–1059. doi:10.1016/j.jbiomech.2013.12.036
- Green, M.A., Bilston, L.E., Sinkus, R., 2008. In vivo brain viscoelastic properties measured by magnetic resonance elastography. *NMR Biomed.* 21, 755–764. doi:10.1002/nbm.1254

- Green, M. a., Geng, G., Qin, E., Sinkus, R., Gandevia, S.C., Bilston, L.E., 2013. Measuring anisotropic muscle stiffness properties using elastography. *NMR Biomed.* 26, 1387–1394. doi:10.1002/nbm.2964
- Groothuis, J., Ramsey, N.F., Ramakers, G.M.J., Van Der Plasse, G., 2014. Physiological challenges for intracortical electrodes. *Brain Stimul.* 7, 1–6. doi:10.1016/j.brs.2013.07.001
- Guo, J., Hirsch, S., Scheel, M., Braun, J., Sack, I., 2015. Three-parameter shear wave inversion in MR elastography of incompressible transverse isotropic media: Application to in vivo lower leg muscles. *Magn. Reson. Med.* 0, n/a-n/a. doi:10.1002/mrm.25740
- Holbourn, A.H.S., 1943. Mechanics of Head Injuries. *Lancet* 242, 438–441. doi:10.1016/s0140-6736(00)87453-x
- Holzappel, G.A., 2000. *Nonlinear Solid Mechanics: A Continuum Approach for Engineering.* John Wiley & Sons, Ltd.
- Hrapko, M., van Dommelen, J.A., Peters, G.W., Wismans, J.S., 2008. The influence of test conditions on characterization of the mechanical properties of brain tissue. *J Biomech Eng* 130, 31003. doi:10.1115/1.2907746
- Iatridis, J.C., Setton, L.A., Weidenbaum, M., Mow, V.C., 1997. Alterations in the mechanical behavior of the human lumbar nucleus pulposus with degeneration and aging. *J. Orthop. Res.* 15, 318–322. doi:10.1002/jor.1100150224
- Johnson, C.L., McGarry, M.D.J., Van Houten, E.E.W., Weaver, J.B., Paulsen, K.D., Sutton, B.P., Georgiadis, J.G., 2013. Magnetic resonance elastography of the brain using multishot spiral readouts with self-navigated motion correction. *Magn. Reson. Med.* 70, 404–412. doi:10.1002/mrm.24473
- Jones, R.M., 1998. *Mechanics Of Composite Materials, Materials Science and Engineering Series.* Taylor & Francis.
- Klatt, D., Friedrich, C., Korth, Y., Vogt, R., Braun, J., Sack, I., 2010a. Viscoelastic properties of liver measured by oscillatory rheometry and multifrequency magnetic resonance elastography. *Biorheology* 47, 133–141. doi:10.3233/BIR-2010-0565
- Klatt, D., Papazoglou, S., Braun, J., Sack, I., 2010b. Viscoelasticity-based MR elastography of skeletal muscle. *Phys. Med. Biol.* 55, 6445–6459. doi:10.1088/0031-9155/55/21/007
- Kleiven, S., Hardy, W.N., 2002. Correlation of an FE Model of the Human Head with Local Brain Motion – Consequences for Injury Prediction. *Stapp Car Crash J.* 46, 123–144.
- Knutsson, H., Westin, C.-F., Granlund, G., 1994. Local multiscale frequency and bandwidth estimation, in: *Proceedings of 1st International Conference on Image Processing. IEEE Comput. Soc. Press*, pp. 36–40. doi:10.1109/ICIP.1994.413270
- Kolsky, H., 1963. *Stress waves in solids.* Dover Publications, New York,.
- Lew, H.L., Poole, J.H., Guillory, S.B., Salerno, R.M., Leskin, G., Sigford, B., 2006. Guest editorial. Persistent problems after traumatic brain injury: the need for long-term follow-up and coordinated care. *J. Rehabil. Res. Dev.* 43, vii–x.
- Manduca, A., Lake, D.S., Kruse, S.A., Ehman, R.L., 2003. Spatio-temporal directional filtering for improved inversion of MR elastography images. *Med. Image Anal.* 7, 465–473. doi:10.1016/S1361-8415(03)00038-0
- Manduca, A., Muthupillai, R., Rossman, P.J., Greenleaf, J.F., Ehman, R.L., 1996. Local Wavelength Estimation for Magnetic Resonance Elastography. *Image Process. ...* 3, 527–530. doi:10.1109/ICIP.1996.560548

- Manduca, A., Oliphant, T.E., Dresner, M.A., Mahowald, J.L., Kruse, S.A., Amromin, E., Felmlee, J.P., Greenleaf, J.F., Ehman, R.L., 2001. Magnetic resonance elastography: non-invasive mapping of tissue elasticity. *Med Image Anal* 5, 237–254. doi:S1361841500000396 [pii]
- Mao, H., Zhang, L., Jiang, B., Genthikatti, V. V., Jin, X., Zhu, F., Makwana, R., Gill, A., Jandir, G., Singh, A., Yang, K.H., 2013. Development of a Finite Element Human Head Model Partially Validated With Thirty Five Experimental Cases. *J. Biomech. Eng.* 135, 111002. doi:10.1115/1.4025101
- Margulies, S.S., Thibault, L.E., 1992. A proposed tolerance criterion for diffuse axonal injury in man. *J Biomech* 25, 917–923.
- Mariappan, Y.K., Glaser, K.J., Manduca, A., Romano, A.J., Venkatesh, S.K., Yin, M., Ehman, R.L., 2009. High-frequency mode conversion technique for stiff lesion detection with magnetic resonance elastography (MRE). *Magn. Reson. Med.* 62, 1457–1465. doi:10.1002/mrm.22091
- Martins, P.A.L.S., Jorge, R.M., N., Ferreira, A.J.M., 2006. A Comparative Study of Several Material Models for Prediction of Hyperelastic Properties: Application to Silicone-Rubber and Soft Tissues. *Strain* 42, 135–147. doi:doi:10.1111/j.1475-1305.2006.00257.x
- McCracken, P.J., Manduca, A., Felmlee, J., Ehman, R.L., 2005. Mechanical transient-based magnetic resonance elastography. *Magn. Reson. Med.* 53, 628–639. doi:10.1002/mrm.20388
- Meaney, D.F., 2003. Relationship between structural modeling and hyperelastic material behavior: application to CNS white matter. *Biomech. Model. Mechanobiol.* 1, 279–293. doi:10.1007/s10237-002-0020-1
- Mooney, M., 1940. A theory of large elastic deformation. *J. Appl. Phys.* 11, 582–592. doi:10.1063/1.1712836
- Murphy, M.C., Huston, J., Jack, C.R., Glaser, K.J., Senjem, M.L., Chen, J., Manduca, A., Felmlee, J.P., Ehman, R.L., 2013. Measuring the characteristic topography of brain stiffness with magnetic resonance elastography. *PLoS One* 8, 1–14. doi:10.1371/journal.pone.0081668
- Muthupillai, R., Ehman, R.L., 1996. Magnetic resonance elastography. *Nat. Med.* 2, 601–603.
- Muthupillai, R., Lomas, D.J., Rossman, P.J., Greenleaf, J.F., Manduca, A., Ehman, R.L., 1995a. Magnetic resonance elastography by direct visualization of propagating acoustic strain waves. *Sci. (New York, N Y)* 269, 1854–1857.
- Muthupillai, R., Lomas, D.J., Rossman, P.J., Greenleaf, J.F., Manduca, A., Ehman, R.L., 1995b. Magnetic resonance elastography by direct visualization of propagating acoustic strain waves. *Science* 269, 1854–7.
- Namani, R., Feng, Y., Okamoto, R.J., Jesuraj, N., Sakiyama-Elbert, S.E., Genin, G.M., Bayly, P. V., 2012a. Elastic characterization of transversely isotropic soft materials by dynamic shear and asymmetric indentation. *J. Biomech. Eng.* 134, 61004. doi:10.1115/1.4006848
- Namani, R., Feng, Y., Okamoto, R.J., Jesuraj, N., Sakiyama-Elbert, S.E., Genin, G.M., Bayly, P. V., 2012b. Elastic characterization of transversely isotropic soft materials by dynamic shear and asymmetric indentation. *J Biomech Eng* 134, 61004. doi:10.1115/1.4006848
- Namani, R., Wood, M.D., Sakiyama-Elbert, S.E., Bayly, P. V., 2009. Anisotropic mechanical properties of magnetically aligned fibrin gels measured by magnetic resonance

- elastography. *J. Biomech.* 42, 2047–2053. doi:10.1016/j.jbiomech.2009.06.007
- Ning, X., Zhu, Q., Lanir, Y., Margulies, S.S., 2006. A Transversely Isotropic Viscoelastic Constitutive Equation for Brainstem Undergoing Finite Deformation. *J. Biomech. Eng.* 128, 925. doi:10.1115/1.2354208
- Ogden, R.W., 1997. Non-linear elastic deformations. Dover Publications, Mineola, N.Y.
- Okamoto, R.J., Clayton, E.H., Bayly, P. V, 2011a. Viscoelastic properties of soft gels: comparison of magnetic resonance elastography and dynamic shear testing in the shear wave regime. *Phys. Med. Biol.* 56, 6379–400. doi:10.1088/0031-9155/56/19/014
- Okamoto, R.J., Clayton, E.H., Bayly, P. V, 2011b. Viscoelastic properties of soft gels: comparison of magnetic resonance elastography and dynamic shear testing in the shear wave regime. *Phys Med Biol* 56, 6379–6400. doi:S0031-9155(11)88885-0 [pii] 10.1088/0031-9155/56/19/014
- Papazoglou, S., Rump, J., Braun, J., Sack, I., 2006. Shear wave group velocity inversion in MR elastography of human skeletal muscle. *Magn. Reson. Med.* 56, 489–497. doi:10.1002/mrm.20993
- Perlmutter, J.S., Mink, J.W., 2006. Deep Brain Stimulation. *Annu. Rev. Neurosci.* 29, 229–257. doi:10.1146/annurev.neuro.29.051605.112824
- Ploch, C.C., Mansi, C.S.S.A., Jayamohan, J., Kuhl, E., 2016. Using 3D Printing to Create Personalized Brain Models for Neurosurgical Training and Preoperative Planning. *World Neurosurg.* 90, 668–674. doi:10.1016/j.wneu.2016.02.081
- Prange, M.T., Margulies, S.S., 2002. Regional, Directional, and Age-Dependent Properties of the Brain Undergoing Large Deformation. *J. Biomech. Eng.* 124, 244. doi:10.1115/1.1449907
- Qin, E.C., Lauriane, J., Lambert, S.A., Paradis, V., Sinkus, R., Bilston, L.E., 2014. In Vivo Anisotropic Mechanical Properties of Dystrophic Skeletal Muscles Measured by Anisotropic MR Elastographic Imaging : The mdx Mouse Model of Muscular Dystrophy. *Radiology* 273, 726–735. doi:10.1148/radiol.14132661
- Qin, E.C., Sinkus, R., Geng, G., Cheng, S., Green, M., Rae, C.D., Bilston, L.E., 2013. Combining MR elastography and diffusion tensor imaging for the assessment of anisotropic mechanical properties: a phantom study. *J. Magn. Reson. Imaging* 37, 217–226. doi:10.1002/jmri.23797
- Riek, K., Klatt, D., Nuzha, H., Mueller, S., Neumann, U., Sack, I., Braun, J., 2011. Wide-range dynamic magnetic resonance elastography. *J. Biomech.* 44, 1380–1386. doi:10.1016/j.jbiomech.2010.12.031
- Rivlin, R.S., 1948. Large Elastic Deformations of Isotropic Materials. IV. Further Developments of the General Theory. *Philos. Trans. R. Soc. London* 241, 379. doi:10.1098/rsta.1948.0024
- Romano, A., Guo, J., Prokscha, T., Meyer, T., Hirsch, S., Braun, J., Sack, I., Scheel, M., 2014. In vivo waveguide elastography: Effects of neurodegeneration in patients with amyotrophic lateral sclerosis. *Magn. Reson. Med.* 1761, 1755–1761. doi:10.1002/mrm.25067
- Romano, A., Scheel, M., Hirsch, S., Braun, J., Sack, I., 2012. In vivo waveguide elastography of white matter tracts in the human brain. *Magn. Reson. Med.* 68, 1410–1422. doi:10.1002/mrm.24141
- Romano, A., Scheel, M., Hirsch, S., Braun, J., Sack, I., 2012. In vivo waveguide elastography of white matter tracts in the human brain. *Magn. Reson. Med.* 68, 1410–1422. doi:10.1002/mrm.24141

- Rouze, N.C., Wang, M.H., Palmeri, M.L., Nightingale, K.R., 2013. Finite element modeling of impulsive excitation and shear wave propagation in an incompressible, transversely isotropic medium. *J. Biomech.* 46, 2761–2768. doi:10.1016/j.jbiomech.2013.09.008
- Royer, D., Gennisson, J.L., Deffieux, T., Tanter, M., 2011. On the elasticity of transverse isotropic soft tissues. *J. Acoust. Soc. Am.* 129, 2757–2760. doi:10.1121/1.3559681
- Sack, I., Beierbach, B., Hamhaber, U., Klatt, D., Braun, J., 2008. Non-invasive measurement of brain viscoelasticity using magnetic resonance elastography. *NMR Biomed.* 21, 265–271. doi:10.1002/nbm.1189
- Salatino, J.W., Ludwig, K.A., Kozai, T.D.Y., Purcell, E.K., 2017. Glial responses to implanted electrodes in the brain. *Nat. Biomed. Eng.* 1, 862–877. doi:10.1038/s41551-017-0154-1
- Schmidt, J.L., Tweten, D.J., Badachhape, A.A., Reiter, A.J., Okamoto, R.J., Garbow, J.R., Bayly, P.V., 2018. Measurement of anisotropic mechanical properties in porcine brain white matter ex vivo using magnetic resonance elastography. *J. Mech. Behav. Biomed. Mater.* 79, 30–37. doi:10.1016/j.jmbbm.2017.11.045
- Schmidt, J.L., Tweten, D.J., Benegal, A.N., Walker, C.H., Portnoi, T.E., Okamoto, R.J., Garbow, J.R., Bayly, P. V., 2016. Magnetic resonance elastography of slow and fast shear waves illuminates differences in shear and tensile moduli in anisotropic tissue. *J. Biomech.* 49, 1042–1049. doi:10.1016/j.jbiomech.2016.02.018
- Schulz-Heik, R.J., Poole, J.H., Dahdah, M.N., Sullivan, C., Date, E.S., Salerno, R.M., Schwab, K., Harris, O., 2016. Long-term outcomes after moderate-to-severe traumatic brain injury among military veterans: Successes and challenges. *Brain Inj.* 30, 271–279. doi:10.3109/02699052.2015.1113567
- Sinkus, R., Siegmann, K., Xydeas, T., Tanter, M., Claussen, C., Fink, M., 2007. MR elastography of breast lesions: Understanding the solid/liquid duality can improve the specificity of contrast-enhanced MR mammography. *Magn. Reson. Med.* 58, 1135–1144. doi:10.1002/mrm.21404
- Sinkus, R., Tanter, M., Catheline, S., Lorenzen, J., Kuhl, C., Sondermann, E., Fink, M., 2005a. Imaging anisotropic and viscous properties of breast tissue by magnetic resonance-elastography. *Magn. Reson. Med.* 53, 372–387. doi:10.1002/mrm.20355
- Sinkus, R., Tanter, M., Xydeas, T., Catheline, S., Bercoff, J., Fink, M., 2005b. Viscoelastic shear properties of in vivo breast lesions measured by MR elastography. *Magn. Reson. Imaging* 23, 159–165. doi:10.1016/j.mri.2004.11.060
- Spencer, A., 1984. Continuum theory of the mechanics of fibre-reinforced composites. Springer-Verlag, Wien ; New York.
- Tweten, D., Okamoto, R., Bayly, P., 2017. Requirements for accurate estimation of anisotropic material parameters by magnetic resonance elastography: A computational study. *Magn. Reson. Med.* 0. doi:10.1002/mrm.26600
- Tweten, D.J., Okamoto, R.J., Schmidt, J.L., Garbow, J.R., Bayly, P. V., 2015. Estimation of material parameters from slow and fast shear waves in an incompressible, transversely isotropic material. *J. Biomech.* 48, 4002–4009. doi:10.1016/j.jbiomech.2015.09.009
- Ueno, K., Melvin, J.W., Li, L., Lighthall, J.W., 1995. Development of Tissue Level Brain Injury Criteria by Finite Element Analysis. *J. Neurotrauma* 12, 695–706.
- Urban, J.P.G., Winlove, C.P., 2007. Pathophysiology of the intervertebral disc and the challenges for MRI. *J. Magn. Reson. Imaging* 25, 419–432. doi:10.1002/jmri.20874

- Van Houten, E.E.W., Miga, M.I., Weaver, J.B., Kennedy, F.E., Paulsen, K.D., 2001. Three-dimensional subzoned-based reconstruction algorithm for MR elastography. *Magn. Reson. Med.* 45, 827–837. doi:10.1002/mrm.1111
- Vavalle, N.A., Davis, M.L., Stitzel, J.D., Gayzik, F.S., 2015. Quantitative Validation of a Human Body Finite Element Model Using Rigid Body Impacts. *Ann. Biomed. Eng.* 43, 2163–2174. doi:10.1007/s10439-015-1286-7
- Velardi, F., Fraternali, F., Angelillo, M., 2006. Anisotropic constitutive equations and experimental tensile behavior of brain tissue. *Biomech Model Mechanobiol* 5, 53–61. doi:10.1007/s10237-005-0007-9
- Wang, M., Byram, B., Palmeri, M., Rouze, N., Nightingale, K., 2013. Imaging transverse isotropic properties of muscle by monitoring acoustic radiation force induced shear waves using a 2-D matrix ultrasound array. *IEEE Trans. Med. Imaging* 32, 1671–1684. doi:10.1109/TMI.2013.2262948
- Wuerfel, J., Paul, F., Beierbach, B., Hamhaber, U., Klatt, D., Papazoglou, S., Zipp, F., Martus, P., Braun, J., Sack, I., 2010. MR-elastography reveals degradation of tissue integrity in multiple sclerosis. *Neuroimage* 49, 2520–2525. doi:10.1016/j.neuroimage.2009.06.018
- Zhang, L., Yang, K.H., King, A.I., 2004. A Proposed Injury Threshold for Mild Traumatic Brain Injury. *J. Biomech. Eng.* 126, 226–236. doi:10.1115/1.1691446
- Zhu, F., Wagner, C., Dal Cengio Leonardi, A., Jin, X., VandeVord, P., Chou, C., Yang, K.H., King, A.I., 2012. Using a gel/plastic surrogate to study the biomechanical response of the head under air shock loading: A combined experimental and numerical investigation. *Biomech. Model. Mechanobiol.* 11, 341–353. doi:10.1007/s10237-011-0314-2

Vita

John L. Schmidt

Degrees

Ph.D. Mechanical Engineering, December 2017
M.S. Mechanical Engineering, August 2015
B.A. Physics, May 2012

Professional Experience

Engineering Intern IV, Seagate Technology, 2012

Professional Societies

American Society of Mechanical Engineers
American Physical Society
Sigma Xi

Journal Publications

Schmidt J. L., Tweten D. J., Benegal A. N., Walker C. H., Portnoi T. E., Okamoto R. J., Garbow J. R., Bayly P. V. 2016. “Magnetic resonance elastography of slow and fast shear waves illuminates differences in shear and tensile moduli in anisotropic tissue”, *J Biomech*, **49**(7), 1042-1049.

Schmidt J. L., Tweten D. J., Badachhape A. A., Reiter A. J., Okamoto R. J., Garbow J. R., Bayly P. V. 2018 “Measurement of anisotropic mechanical properties in porcine brain white matter *ex vivo* using magnetic resonance elastography”. *J Mech Beh Biomed Matls*, **79**, 30-37

Tweten D. J., Okamoto R. J., **Schmidt J. L.**, Garbow J. R., Bayly P. V. 2015. “Estimation of material parameters from slow and fast shear waves in an incompressible, transversely isotropic material”. *J Biomech*, **48**(15), 4002-4009

Guertler C. A., Okamoto R. J., **Schmidt J. L.**, Badachhape A. A., Johnson C. L., Bayly P.V. “Mechanical Properties of Porcine Brain

Tissue In Vivo and Ex Vivo Estimated by MR Elastography”
(Submitted).

Beauchemin P.-F., Bayly P. V., Garbow J. R., **Schmidt J. L.**,
Okamoto R. J., Chériet F., Périé D. “Frequency dependent shear
properties of bovine *ex vivo* intervertebral disc”. (Submitted)

**Conference
Abstracts and
Proceedings**

Schmidt J. L., Tweten D. J., Badachhape A. A., Okamoto R. J.,
Garbow J. R., Bayly P.V., “Estimation of Anisotropic Shear
Moduli in White Matter of the Brain by Magnetic Resonance
Elastography and Finite Element Modeling.” *Design of Medical
Devices Conference*, Minneapolis, Minnesota. April 2017.

Schmidt J. L., Tweten D. J., Badachhape A. A., Okamoto R. J.,
Garbow J. R., Bayly P.V., “Anisotropic shear modulus estimation
in ex vivo white matter of the brain using magnetic resonance
elastography and finite element modeling.” *International Society
for Magnetic Resonance in Medicine Annual Meeting*, Honolulu,
Hawaii. April 2017.

Award: Educational Stipend.

Schmidt J. L., Tweten D. J., Badachhape A. A., Okamoto R. J.,
Garbow J. R., Bayly P.V., “Magnetic resonance elastography of
white matter brain tissue ex-vivo.” *ASME International
Mechanical Engineering Congress and Exposition*, Phoenix,
Arizona. November 2016.

Schmidt J. L., Tweten D. J., Badachhape A. A., Okamoto R. J.,
Garbow J. R., Bayly P.V., “Mechanical anisotropy of ex vivo
bovine intervertebral disc from magnetic resonance elastography.”
Biomedical Engineering Society Annual Meeting, Minneapolis,
Minnesota. October 2016.

Schmidt J. L., Tweten D. J., Badachhape A. A., Okamoto R. J.,
Garbow J. R., Bayly P.V., “Magnetic resonance elastography of
white matter brain tissue ex-vivo.” *Summer Biomechanics,
Bioengineering, and Biotransport Conference*, National Harbor,
Maryland. June 2016.

Schmidt J. L., Tweten D. J., Mahoney M. M., Portnoi T. E., Okamoto R. J., Garbow J. R., Bayly P. V., “Experimental measurement of shear and tensile moduli in anisotropic tissue using magnetic resonance elastography.” *Summer Biomechanics, Bioengineering, and Biotransport Conference*, Snowbird, Utah. June 2015.

Schmidt J. L., Tweten D. J., Mahoney M. M., Portnoi T. E., Okamoto R. J., Garbow J. R., Bayly P. V., “Magnetic resonance elastography of slow and fast shear waves illuminates differences in shear and tensile moduli in anisotropic tissue.” *International Society for Magnetic Resonance in Medicine Annual Meeting*, Toronto, Ontario, Canada. June 2015.

Award: Educational Stipend.

Schmidt J. L., Banerjee P., “Electrical Conductivity Modeling and Validation in Unidirectional Carbon Fiber Reinforced Polymer Composites.” *COMSOL Conference*, Boston, Massachusetts. October 2013.

Invited Talks

Johns Hopkins University Applied Physics Laboratory
Biomechanics and Injury Mitigation Systems Division
Laurel, Maryland, November 2017